FLOW CONTROL TECHNIQUES IN A SERPENTINE INLET: AN ENABLING TECHNOLOGY TO INCREASE THE MILITARY VIABILITY OF UNMANNED AIR VEHICLES

by

Andrew Scott Luers

B.S. Physics and Economics
Texas Christian University, 2001

Submitted to the Department of Aeronautics and Astronautics
and to the Engineering Systems Division
in partial fulfillment of the requirements for the degrees of

Master of Science in Aeronautics and Astronautics

and

Master of Science in Technology and Policy

at the
Massachusetts Institute of Technology
June 2003

Author: _____
Andrew Scott Luers
Department of Aeronautics and Astronautics
Technology and Policy Program
May 15, 2003

Certified by: _____
James D. Paduano
Principal Research Engineer
Thesis Supervisor

Certified by: _____
David A. Mindell
Associate Professor of the History of Engineering and Manufacturing
Policy Reader

Accepted by: _____
Daniel E. Hastings
Professor of Aeronautics and Astronautics and Engineering Systems
Director, Technology and Policy Program
Chairman, Committee for Graduate Studies

Accepted by: _____
Edward M. Greitzer
Professor of Aeronautics and Astronautics
Chairman, Departmental Graduate Committee

FLOW CONTROL TECHNIQUES IN A SERPENTINE INLET: AN ENABLING TECHNOLOGY TO INCREASE THE MILITARY VIABILITY OF UNMANNED AIR VEHICLES

By
Andrew Scott Luers

Submitted to the Department of Aeronautics and Astronautics and the Engineering Systems Division on May 15, 2003 in partial fulfillment of the requirements for the Degrees of Master of Science in Aeronautics and Astronautics and Master of Science in Technology and Policy

ABSTRACT

By removing the pilot from the aircraft, unmanned air vehicles allow developers to trade off vehicle survivability with cost and capability in the equation to find the right vehicle for a particular need. Recent UAV programs have shown that understanding this new equation is essential for program success and have indicated that increased survivability is only desirable to the extent that it does not significantly drive up costs or limit capabilities. In current UCAV programs 'mission creep' is pressuring developers to make larger more capable and highly survivable vehicles that will carry high price tags. This will likely result in delaying the introduction of the UCAV into the force mix and presents an opportunity for a competing development program to produce a cheaper more attritable vehicle that will ultimately be more attractive to military planners.

Active Flow Control can help the UCAV to achieve its survivability goals while reducing costs and improving performance. High subsonic flow experiments (Mach number 0.65) were conducted in a $1/6^{th}$ scale model UCAV inlet as part of an integrated inlet-compression system Active Flow Control study. Hot-film sensors were placed in the separated region of the inlet in attempt to capture the unsteadiness in the flow for use in feed-forward control schemes that use compressor face actuation. An FIR Wiener filter was constructed and used to filter the hot-film data. After filtering, this data was found to be highly correlated to data measured at the AIP and thus potentially useful for feed-forward control of compressor face actuators. In addition, periodic injection was introduced near the separation point in attempt to improve pressure recovery and mitigate distortion at the Aerodynamic Interface Plane (AIP). Data was collected by way of 80 equal-area total pressure measurements covering the AIP as well as by static pressure taps placed at various locations around the diffuser. Results include total pressure maps, upper-quadrant pressure recovery, and distortion as functions of the governing parameters. For an injection mass flow of 2% of the inlet mass flow, the best injection configuration to date increases total pressure recovery in the upper quadrant (where separation effects are severe) from 93% to 97% (a 60% reduction in the losses) and significantly reduces distortion. Various parameters governing injector geometry and actuation behavior were examined and optimized

Thesis Supervisor: James D. Paduano
Title: Principal Research Engineer

Policy Reader: David A. Mindell
Title: Associate Professor of the History of Engineering and Manufacturing

Acknowledgements

I would first like to give my sincere thanks to my research advisor Dr. James Paduano for inviting me to be a part of the Micro-Adaptive Flow Control Project and for his constant guidance throughout my time at MIT. I would also like to thank Dr. Gerald Guenette for his willingness to answer my many questions. Both were extremely generous with their time and patient in helping me to work through the problems of this research.

In addition, I would like to thank Professor David Mindell for agreeing to serve as my Policy Reader and Sydney Miller for the many hours she spent helping me to coordinate the TPP and Aero-Astro curricula.

I would also like to thank the staff of the Gas Turbine Laboratory with whom, thanks to the highly experimental nature of my research, I was fortunate to spend much time. Their help in the design, fabrication and operation of the experiments was invaluable as were their considerable political and philosophical insights.

Thanks are also deserved by many of the other students of the GTL who often lent me their time and talents and who helped to make my days here so enjoyable. Specifically I'd like to thank Steve Braddom and Brian McElwain for showing me the ropes on this project, Jameel Janjua for constantly distracting me from the project, Neil Murray for helping me understand the virtues of Murphy's, Chris Protz for introducing me to midnight scuba diving in New England, Dan Kirk for the unique ability to make summer softball an intense experience, and Jean Collin for helping me to develop a coffee addiction.

Lastly I'd like to thank my family for their constant love and encouragement and for frequently coming to visit when the demands of MIT didn't allow much time for me to make it home.

This work was supported by AFSOR contract #F49620-00-C-0035, as part of the DARPA Micro-Adaptive Flow Control Program, Dr. Thomas J. Beutner, contract monitor.

Table of Contents

List of Figures

List of Tables

Nomenclature

Acronyms

ACTD	Advanced Concept Technology Demonstration
AFB	Air Force Base
AFC	Active Flow Control
AIP	Aerodynamic Interface Plane
CFD	Computational Fluid Dynamics
CTA	Constant Temperature Anamometry
DARPA	Defense Advanced Research Projects Agency
DoD	Department of Defense
EO/IR	Electrical-Optical/Infrared
EMD	Engineering Manufacturing and Development
FIR	Finite Impulse Response
GTL	Gas Turbine Laboratory
HAE	High Altitude Endurance
ISR	Intelligence Surveillance and Reconnaissance
JSF	Joint Strike Fighter
J-UCAV	Joint Unmanned Combat Air Vehicle
MAE	Medium Altitude Endurance
MISO	Multiple-Input Single-Output
MIT	Massachusetts Institute of Technology
PAV	Average Total Pressure
PAVLOW	Average Total Pressure of Low Pressure Region
PPSL	Predator Primary Satellite Link
SAM	Surface-to-Air Missile
SAR	Synthetic Aperture Radar
SDIU	Scan-valve Digital Interface Unit
SEAD	Suppression of Enemy Air Defenses
SISO	Single-Input Single-Output
UAV	Unmanned Aerial Vehicle

UCAV	Unmanned Combat Air Vehicle
UFP	Unit Flyaway Price
VG	Vortex Generator
VI	Virtual Instrument

Symbols

A_{inj}	Area of Injection Slot
A_s	Area of Separated Region
c	Characteristic Length (i.e. chord)
c_x	Axial Velocity
C_μ	Momentum Coefficient
$C_{\mu steady}$	Steady Momentum Coefficient
$<C_\mu>$	Unsteady Momentum Coefficient
δ	Boundary Layer Thickness
DC(60)	Distortion
DPCP	Distortion Intensity
$f_{excitation}$	Excitation Frequency
F+	Nondimensional Frequency
γ	Ratio of Specific Heats
h	Slot Width, Enthalpy
l	Length of Injection Slot
L	Characteristic Length
M	Mach Number
$\dot{m}$	Mass Flow
P_{atm}	Atmospheric Pressure
P_{ref}	Reference Total Pressure
P_T	Total Pressure
$\overline{P_t}\big\|_{360}$	Average Total Pressure at AIP
$\overline{P_t}\big\|_{60}$	Average Total Pressure over the 60° with the Greatest Distortion
R	Gas Constant

Re	Reynolds Number
ρ_{inj}	Density of Injected Flow
ρ_∞	Density of Inlet Flow
T_T	Total Temperature
T_{ref}	Reference Total Temperature
T_{atm}	Atmospheric Temperature
U_{inj}	Mean Velocity of Injected Flow
u_{inj}	Amplitude of Oscillatory Component of Injected Velocity
U_∞	Velocity of Inlet Flow
V	Volts

1 INTRODUCTION

1.1 Motivation

1.1.1 The UCAV

The Unmanned Combat Air Vehicle (UCAV) is an emerging weapon system with revolutionary potential. With the emergence of unmanned vehicles comes a host of new opportunities. One of these opportunities is a new way for the aerospace industry and the military to treat the issue of aircraft survivability. For a given mission requirement, aircraft survivability can now enter the calculation as a variable that can be traded with cost and capability. It will be essential that those involved with UCAV development programs recognize this opportunity. If an industry contractor fails to recognize and exploit this new equation it will likely mean that they will lose out to a competitor who does. If the military fails to recognize and exploit this new equation the development of the UCAV will likely be delayed as alternative assets out compete it for military dollars and mission use. Active Flow Control has the potential to significantly contribute to this new calculation by allowing UCAVs to be designed for high survivability while reducing cost and maintaining or improving performance.

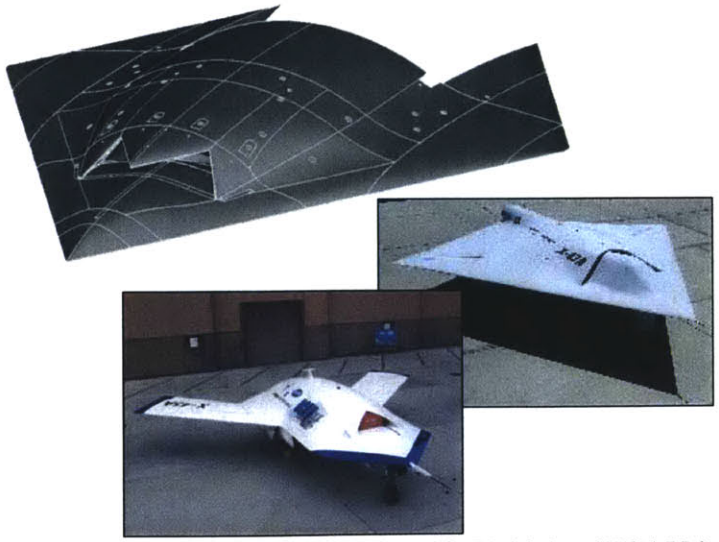

Figure 1-1: Unmanned Combat Air Vehicles (UCAVs)

For manned aircraft, aircraft survivability equates to crew survivability and thus it is treated with special deference. The aircraft itself, though expensive, is of secondary importance to the crew. According to military doctrine, missions involving manned aircraft are planned to have "100% in and 100% out." The uncompromising concern for the crew is further emphasized by a public that has become averse to casualties of war and has come to expect an extremely low number of combat fatalities. These priorities place limitations upon which missions can be conducted. If a military planner feels that it is unlikely that they can achieve 100% in 100% out, the mission will not be undertaken and an alternative strategy must be devised. "I don't want to be the one to tell any mother that in my plan I came up with an idea that your son was attritable." Said one military planner [25].

New technologies can sometimes expand the mission possibilities while allowing military planners to stick to this doctrine by creating an aircraft with capabilities that reduce the risk of them being intercepted by defensive weapons. Such technologies include making the aircraft faster and more maneuverable, developing countermeasures and making the aircraft less visible to enemy radar. All of these things are included in the category of aircraft survivability. But technological advantages in the area of survivability become eroded with advances in defensive technologies and thus this becomes a game of one-up-man-ship that relies on ever-improving technologies.

In this game, crew survivability is of primary importance and cost and capability are traded off. The military, in an attempt to create an aircraft that is capable of successfully and safely completing a certain mission, can fix cost and thus will sacrifice certain other capabilities (i.e. payload, endurance, etc.), or they can fix the capability requirements and will thus end up with a more expensive vehicle. The equation can be illustrated as,

$$\frac{\text{Survivability}}{\text{Cost} \Leftrightarrow \text{Capability}}$$

where survivability is fixed and cost and capability are traded.

Never-the-less, it is unlikely that advantages achieved through improvements in aircraft survivability will ever be so great that manned aircraft will be able to fulfill every mission that military planners would like to specify all the time.

With unmanned aircraft, the equation changes. Without a crew to worry about, losing an aircraft now just means losing expensive equipment. In the words of one Air Force colonel, "If I plan a mission and we lose a UCAV the controller's mom and dad back in Des Moines Iowa are not upset with me" [25]. Thus, now the equation becomes,

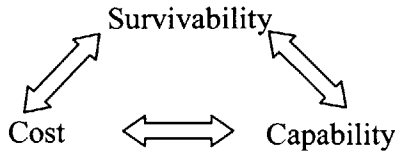

It is hard to overstate the implications of this change both for military planners and for industry designers and developers. How the issue of survivability is treated will likely be a major factor in determining when the UCAV will ultimately be introduced into the force mix and how and to what extent it will be used.

1.1.2 Flow Control

At the same time the UCAV is emerging as a potentially revolutionary weapon system for the military, a field of study called Active flow control (AFC) is quickly growing and has equal revolutionary potential for the aerospace industry. In a broad sense AFC consists of using actuators, sensors and controllers to influence the flow of air over, within, or around an aircraft. Studies are being conducted that use AFC on wings, in inlets, engines and nozzles, on tails, on weapons bays and for just about every other conceivable application. In the words of one engineer working for a large aerospace company,

> "We see active flow control as a potential revolutionary technology for the next generation of air vehicles. ACF will allow designers to shape the aircraft the way they want to, make them smaller, and meet all of the performance requirements, but at a much lower cost. The limiting factor in all of these things has been

traditional aerodynamic design laws but AFC will allow designers to push beyond the traditional limits or bounds of the design space" [26].

Active flow control goes right to the heart of the equation mentioned above because it is a technology that could allow UCAV designers to reduce costs while at the same time improving capability and survivability.

All UCAV designs which have currently been made available to the public feature a top-mounted serpentine inlet. This design is purely for survivability purposes as it is helpful in making the aircraft less visible to radar by providing line-of-sight blockage of the engine face. However, these designs are typically in conflict with engine performance. If the inlet diffuses the flow too aggressively or the ductwork turns too sharply, flow separation will occur and result in pressure loss, distortion and unsteadiness at the compressor face. This in turn will result in decreased efficiency, reduced compressor stability, and reduced stall and surge margins.

Many UCAV designs are limited in length by the propulsion system; if weapons bay length is not a driving factor, it is the longest feature of the aircraft and sets the minimum size of the airframe. The propulsion system consists of the inlet through which the flow is initially passed and conditioned, the engine in which it is compressed and in which combustion takes place, and the nozzle through which it is ejected. Because the propulsion system currently sets the minimum airframe size, there is a strong incentive to reduce aircraft length, and thus cost, by making shorter more aggressive inlets, while at the same time maintaining system performance

Flow control is an enabling technology that can facilitate the design of more aggressive inlet designs while improving the performance and robustness of the propulsion system.

By allowing designers to make short serpentine inlets while maintaining performance requirements, flow control allows designers to design for survivability while reducing costs by making the aircraft shorter. It is estimated that designers can save about $1000

for every pound of gross take off weight that is reduced, or $1 million per inlet diameter reduced [26]. Figure 1-2 shows an example of a serpentine inlet and illustrates the desired change. The improvements in performance relate to improvements in propulsive efficiency, and compressor stability and stall and surge margins. These improvements can translate into increases in payload or flight duration of the aircraft, as well as increases in the flight maneuverability envelope and decreases in fuel consumption.

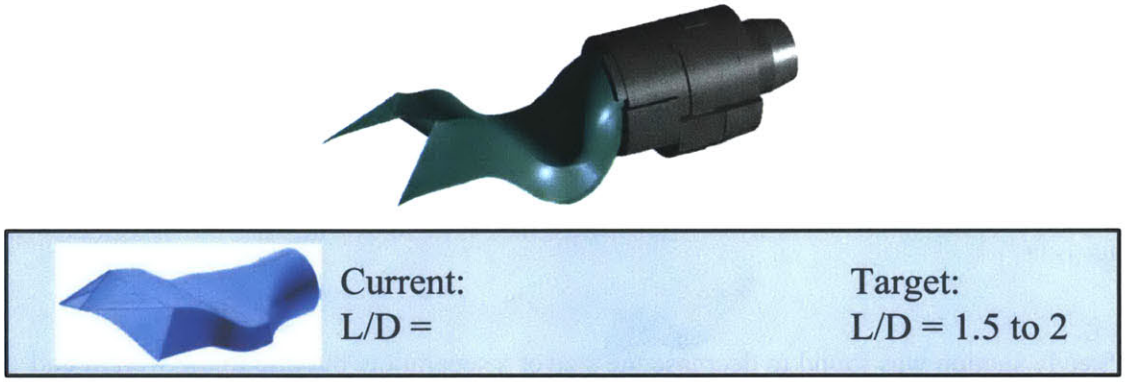

Figure 1-2: Inlet Ducts

1.2 Previous Work

Most flow control studies conducted on internal flows have consisted of simplified geometries and low Mach number flows. The primary means for control has been through the injection or removal of mass flow in order to prevent flow separation or reattach the flow. Other studies have demonstrated the ability of compressor face actuation to mitigate the effects of unsteadiness on the compressor. And still other studies have shown the potential for wall-based sensors in a turbulent flow to capture the unsteady properties.

1.2.1 Literature Review

1.2.1.1 Upstream Boundary Layer Actuation

Many active flow control techniques involve attempts at preventing separation or reattaching the boundary layer. Historically the primary methods to do this have been

steady state methods – steady blowing and suction in the boundary layer. More recently, however, many studies have used periodic excitation methods, such as the periodic injection of mass flow, acoustic pulses, and synthetic jets.

In a review of studies performed at low Mach numbers on external flows, Grenblatt and Wygnanski concluded that periodic excitation, which exploits instabilities in the flow, performed better than steady blowing, allowing control with much lower input energy. They explained the reason for this being that large coherent structures in the flow are primarily responsible for the transport of momentum across the flow domain and the introduction of periodic excitation "accelerates and regulates the generation of large coherent structures, thereby transferring high momentum fluid across the mixing layer."[1]

Steady suction was found to decrease the size of a separation, but due to the weight and complexity of the associated system, suction was not deemed a feasible solution for use on an aircraft [1].

The two parameters used by Grenblatt, Wygnanski and others to quantify excitation are the momentum coefficient, C_{μ}, and a non-dimensionalised frequency, F+. C_{μ} is the ratio of the momentum added to the system to that in the free stream, and it can be broken down into steady and unsteady components. $C_{\mu steady}$ is the ratio of the mean added momentum to the free stream momentum; $\langle C_{\mu} \rangle$ is the ratio of the oscillatory component of the added momentum to the free stream momentum.

$$C_{\mu steady} = \frac{\rho_{inj} U_{inj}^2 h}{\rho_{\infty} U_{\infty}^2 c} \tag{1-1}$$

$$\langle C_{\mu} \rangle = \frac{\rho_{inj} u_{inj}^2 h}{\rho_{\infty} U_{\infty}^2 c} \tag{1-2}$$

ρ_{inj}, and U_{inj} are the density and mean velocity of the injected flow, h is a reference length for the added momentum, such as an ejection slot width, u_{inj} is the amplitude of the oscillatory component of the injected velocity, ρ_{∞} and U_{∞} are the density and velocity of the free stream flow, and c is a reference length for the free stream momentum. In their

review, Grenblatt and Wygnanski found a value of $C_{\mu steady}$ below about 2% to be detrimental and found values of $<C_{\mu}>$ of about 0.02% to have a large impact on the separation [1].

F+ is the actuation frequency multiplied by a reference length and divided by the free stream velocity.

$$F+ = \frac{f_{excitation} L}{U_{\infty}} \tag{1-3}$$

An F+≈1 was found to be an optimal value for controlling turbulent separated flow, and this value was found to be independent of Reynolds number [1].

In low subsonic flows, the synthetic jet, a method of periodic excitation, has shown particular success [2],[3]. These devices alternate between a blowing and suction cycle in which they energizing the boundary layer by blowing high momentum air into it, and remove the low momentum flow from the boundary layer through suction with zero net mass flux. In a 2D divergent duct with a free stream flow of M=0.05, McCormick used directed synthetic jets to improve pressure recovery. He found that pressure recovery did improve with increased $C_{\mu steady}$ up to a value of 0.6%, which he called the saturation level. The optimal forcing frequency in this study was also found to be F+=1. Amitay et al conducted a similar study in a 2D serpentine duct with constant area (i.e. no diffusion) in which the boundary layer was tripped to artificially cause a separation. Synthetic jets were then used to reduce the separation and improve pressure recovery. They tested up to M=0.3 and found that they were able to reattach the flow and, with increased levels of actuation, decrease the total pressure loss in the duct. Their results led them to suggest that periodic excitation can improve the separation behavior of serpentine inlets at high subsonic conditions as well [2].

While synthetic jets have been shown to be a successful method of periodic excitation in low speed flows, there are few studies that indicate whether they can provide the necessary control authority for high subsonic flows. An outstanding issue is the fact that, for such injectors operating in high-speed flows, the injected momentum is lower than the

free stream momentum during most of the duty cycle. Periodic excitation about a non-zero mean injection level, on the other hand, has an additional degree of freedom that allows mean momentum to be relatively high compared to the base flow.

Seifert and Pack showed that with periodic blowing they were able to shrink the separation region in a high subsonic flow (M=0.65) on a 2D wing section [4].

An exception to the use of periodic excitation has been a recent use of vane and air-jet vortex generators (VGs). Vane and air-jet VGs have been used to generate vortices opposite to, and thus nullifying of, the secondary flows [5], [6]. These methods concentrate on improving the flow quality in serpentine diffusers by preventing 'lift-off' of longitudinal vortices. Such approaches address inlets that are dominated by secondary flow vortex lift-off, rather than inlets with separation events induced by strong adverse pressure gradients [7].

1.2.1.2 Sensing Unsteadiness

The above studies address the steady effects of the separation, however it has also been found that many unsteady effects exist which can be equally detrimental to system performance. Controlling the steady effects of the separation will likely do little to improve the unsteady effects and may actually exacerbate the problem [8]. Prior research at MIT has demonstrated the ability to mitigate unsteady effects at the compressor face through compressor face actuation [9], [10], [11]. In order to use compressor face actuation to control unsteadiness, sensors must be used to capture the unsteadiness.

In a real application it is not practical to place sensors in front of the compressor face and so the unsteadiness must be captured in another way. One possibility is through the use of upstream wall-based sensors. If the separation and flow instabilities (structures in the flow) can be identified and correlated to the control points, it may be possible to place sensors in the flow to provide real-time data that can be used in a closed loop control scheme to achieve a desired outcome. Using upstream sensors could provide an

additional advantage by allowing the possibility of implementing feed-forward control because they could capture the unsteadiness before it reaches the compressor face.

In order to provide this real-time data, it must be possible to characterize the turbulent boundary layer with the use of sensors. It is assumed that the behavior of the coherent structures in the flow are the primary contributors to the nature of the flow and thus identification techniques are geared toward the identification of these structures [8]. Various sensing techniques have been used to do this, which measure the wall shear stress, stream-wise velocity fluctuations and wall pressure fluctuations.

Recently, Ng and Burdisso studied the ability of a microphone in a separating 2D serpentine inlet to be used as a feedback sensor and concluded that as actuation was applied to the separated flow, the microphone data correlated well with improvements in the boundary layer and thus showed promise for such a use [12]. Rabe et al in a similar study of a 3D serpentine inlet concluded that large amplitude wall static pressure fluctuations measured by surface-microphones can be used to indicate the levels and locations of distorted flows [6].

Previous research and experience have shown the usefulness of hot film sensor for determining the characteristics of a flow and for use in active control systems to improve aircraft and engine performance [13], [14]. Hot film sensors measure the time varying shear stress levels on the surface to which they are adhered and thus can provide information about the size and stability of a separated region.

Many different controls schemes for AFC have been suggested. Israel and Fasse discuss several different aspects of closed loop control and consider non-linear and linear control laws. They decide in favor of a linear approach for the following reasons: (1) there are many powerful linear design tools, (2) linear methods are used successfully in practical flight controls systems, (3) linear methods have been applied successfully in research to certain flow control problems, and (4) any developed linear controller can be used as a baseline for comparison with more sophisticated nonlinear controllers [13]. Isreal and

Fasse consider a single-input, single-output (SISO) system where the input is an upstream sensor and the output is a sensor at a selected downstream control point (the place to be optimized by the control)

Rathnasingham and Breuer have also demonstrated effective closed-loop control in a low Reynolds number fully turbulent flow. They made the assumptions that large scale "coherent structures" in the near-wall region are responsible for the majority of the turbulence production and that these coherent structures may be modeled for short times as linear with respect to the mean flow [14], [15], [16], [17]. These assumptions allowed them to use a Wiener filter, which can be easily computed and updated, and which facilitates a multiple-input, single-output (MISO) system. Using multiple inputs provides the advantage of giving a more accurate picture of the flow and provides greater flexibility for sensor placement.

1.2.2 Previous Work Done at MIT

As part of an ongoing project at MIT an integrated approach to flow control of the inlet-compressor combination was undertaken. High subsonic Experiments were performed on a $1/6^{th}$ scale model of a Northrop-Grumman prototype UCAV inlet, with 3D geometry. At cruise operating conditions, this inlet exhibits a strong separation from the top surface and a smaller separation from the bottom surface as well. Measurements taken at the Aerodynamic Interface Plane (AIP), the plane between the inlet and compressor, show unsteadiness, a loss of pressure recovery and two distorted regions, a larger one at the top of the AIP and a smaller one at the bottom. The present study attempts to eliminate the source of the separation by way of periodic separation point injection; it attempts to improve the robustness of the compressor by way of compressor face actuation; and it attempts to provide real-time data for use in controlling the actuators by way of wall-based sensors placed in the separation zone.

Warfield and Brear characterized the inlet flow, which will be discussed in more detail in chapter 5 [18], [19]. They found that two large counter-rotating vortices form in the separated region and they hypothesize that these vortices periodically shed and convect

downstream, resulting in the large total pressure loss regions that are observed at the AIP. It was found that the unsteadiness does have an effect on the compressor stall point and that, in some cases, unsteadiness has a larger impact than steady state distortion [7]. Warfield placed actuators downstream of the AIP in order to simulate compressor face actuation. Using an unsteady pressure probe placed at the AIP and the actuators, Warfield was able to reduce the local unsteadiness at the AIP through the use of feedback control [18].

Several hot film sensors were then placed in the separation region to determine if they could capture the same information as did the total pressure probe at the AIP and thus be used in its stead. Data from the hot film sensors were correlated to data taken at the AIP from the unsteady probe and the coherence and correlation between a hot film sensor and the unsteady probe was calculated. Figure 1-3 shows a coherence of greater than 0.5 at frequencies of 500-600 Hz. Warfield concluded that this frequency corresponds to the characteristic vortex shedding frequency of the flow separation.

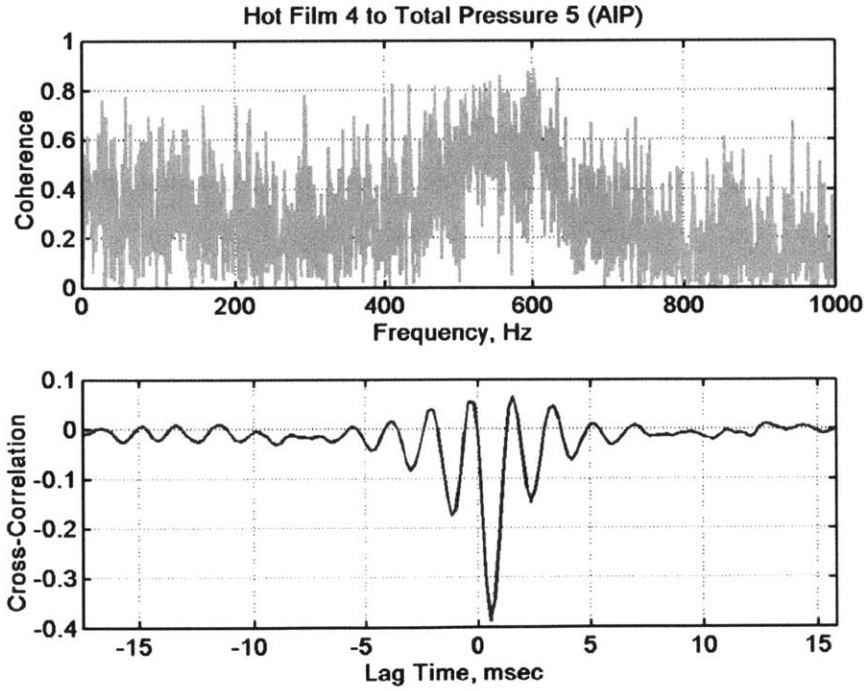

Figure 1-3: Coherence and Correlation Between a Hot-Film Sensor in the Separated Region and an Unsteady Total Pressure Probe at the AIP

The time delay is consistent with the flow convection time, further indicating that the distortion seen at the AIP results from a periodic convective disturbance, such as a vortex shedding, which travels from the separated region to the AIP. Warfield concluded that the coherence was sufficiently high to generate a transfer function between the hot film and unsteady total pressure probe

Braddom further demonstrated the ability of hot film sensors to provide valuable information about the separated region [20]. He inserted a 30-sensor hot film array covering the entire region, which provided valuable information about which regions of the separation were most highly correlated to the AIP and he showed that many of the sensors were highly correlated within a characteristic frequency band.

Braddom demonstrated that hot film sensors in the separated flow region can predict unsteady flow conditions at the AIP and that hot film sensors can determine the steady intensity of the separation and thus provide information on the inlet pressure recovery. In addition, Braddom developed robust hot film sensors that could be used in realistic environments over prolonged periods of time in adverse conditions.

In a third study, McElwain explored the use of periodic separation point injection in order to energize the boundary layer of the flow to prevent separation or to reattach the flow [21]. The injected flow was introduced into the diffuser by way of a Coanda-type injector, which takes advantage of the Coanda Effect to keep the injected flow attached to the inner wall of the inlet.

Most studies were conducted in a 2D diffuser that matched the geometry of the 3D inlet. This was done in order to better understand the underlying effects as well as to experimentally verify CFD predictions [21], [22]. In the 2D case McElwain showed that periodic excitation via pulsed injection into the boundary layer near the flow separation point (with relatively high mean momentum) can reattach the flow and improve downstream pressure recovery for a high subsonic flow in a 2-D diffuser [21].

McElwain showed that increased actuation frequency allowed for a greater improvement with less injection mass flow; 2 kHz, the highest frequency tested, yielding the best result. The steady component of injection, however, was found to primarily account for enhanced control of separation; this result is contrary to previous findings at low Mach numbers, where steady injection was found to be detrimental to separation [21].

McElwain then modified the 3D inlet for separation point injection and did a preliminary proof of concept test. He found that periodic separation point injection can improve pressure recovery at the aerodynamic interface plane, but did not perform as well as in the 2D case. He hypothesized that a good value for the ratio between the mean injection velocity and the free stream velocity is one, which would result in a minimum C_μ requirement. Thus injection slot size should be optimized to provide a mean velocity ratio of one at the desired injection mass flow.

All of the above studies indicate that the steady effects of separation in a 3D serpentine diffuser can be controlled by periodic excitation. The important parameters for controlling separation are the ratio of the added mean, and oscillatory momentum to the free stream momentum, and the frequency of actuation. In addition, they indicate that shear stress from large coherent structures in the flow could be used in a control loop to control actuators at the compressor face to mitigate unsteady effects.

1.3 Objectives

The objectives of this thesis are to first examine the question of how survivability should be treated for unmanned air vehicles, and to see if current UCAV programs are treating it appropriately, and second to advance the understanding of flow control technology, as it directly relates to aircraft survivability, as a potential enabler for increasing aircraft survivability while decreasing costs.

In order to advance flow control technology, this thesis will attempt to provide answers to the following questions:

1) Can we use the Rathnasingham and Breuer method with multiple hot film sensors in a 3D inlet at high subsonic conditions to adequately capture the unsteadiness experienced at the AIP?
2) Can the ability of separation point injection to reduce the steady effects of flow separation be improved upon by adjusting several parameters, and if so, by how much?

Specifically, this thesis attempts to further work done by Warfield and Braddom by identifying the optimal locations of sensor placement within the inlet to best characterize the flow and predict downstream conditions, then to use the control method of Rathnasingham and Breuer, briefly described above, to create a MISO filter which will provide a sufficiently high correlation of input to output that could be used for the purposes of feed-forward control, and finally to determine the optimal number of sensors to be used in the inlet and test the robustness of the filter over varying conditions.

In addition, the work of McElwain is furthered by performing a parametric study of the effects of C_μ, injection position, injection angle and forcing frequency. The ultimate goal is to find the optimal value of these parameters within this inlet, where the metrics for improvement are Pressure Recovery and distortion at the AIP.

1.4 Approach

In order to examine the question of how survivability should be handled by UCAV developers, a study of two UAV programs will be presented which illustrate many of the relevant issues and can thus provide lessons for the UCAV. In addition, interviews with people in Academia, Industry, and the Military were conducted in order to assess the UAV programs, current UCAV programs and the military environment and needs.

In order to contribute to the advancement of flow control technology for the potential use in helping to overcome some of the survivability challenges facing UCAVs, several experiments were conducted at the Gas Turbine Lab (GTL) at MIT using the $1/6^{th}$ scale UCAV model and a De Laval air compressor to produce high subsonic flows.

1.5 Thesis Overview

The remainder of this thesis focuses on three topics. Section one is a look at the UCAV issues, in which chapter two is a case study involving Predator and Global Hawk, chapter three is a look to the military, chapter four, a look to industry and current UCAV programs, and finally, chapter five ties this to flow control and work done in a specific UCAV inlet.

Section two is a description of a study to advance toward active control in a realistic inlet geometry at realistic Mach numbers using separation zone wall-based sensors, where chapter six describes the theoretical underpinnings and the experimental setup and chapter seven describes the results.

Section three describes a study of boundary layer actuation in search of optimizing separation control in this inlet while exploring many of the important physical properties involved with the general problem, where chapter eight describes the experimental setup, chapter nine describes the results and chapter ten describes the development and use of a new actuator that was also tested for use in periodic separation-point injection. Finally, section four includes a discussion of the results and their implications followed by recommendations for future work.

SECTION 1 – THE NEW EQUATION

2 UAVs AS AN ILLUSTRATION OF THE ISSUES

2.1 Introduction

As stated in chapter one, because unmanned air vehicles (UAVs) remove the person from the aircraft cockpit, the military can now trade off survivability, along with cost and capability, as they try to develop the right vehicle for a given need. This is because where as the military thankfully never considered a person to be attritable they can consider a UAV to be attritable.

Survivability is defined by the Department of Defense (DoD) to be a "Concept which includes all aspects of protecting personnel, weapons, and supplies while simultaneously deceiving the enemy. Survivability tactics include building a good defense; employing frequent movement; using concealment, deception, and camouflage; and constructing fighting and protective positions for both individuals and equipment." An attritable item is one that, though not intended to be lost or destroyed, is used in such a way that the probability of loss may be high; the 100%-in 100%-out doctrine is loosened. This is in contrast to expendable, which, according to the DoD means, "Property that may be consumed in use or loses its identity in use and may be dropped from stock record accounts when it is issued or used." An attritable item is not intended to be lost when used, but instead a high probability of being lost or destroyed is allowed [24].

Current UAV programs have already begun to deal with the question of how survivability should be treated by industry developers and military planners and can thus be instructive for current UCAV programs. The two UAV programs that will be examined here are the Predator and Global Hawk UAVs, where the Global Hawk will be contrasted with its primary competitor, the DarkStar.

2.2 Predator

Today there are over 150 UAV designs being developed and of those 115 have flown either in use or as a prototype. The government spent $3 billion on the development of UAVs from 1991-1999 and is projected to spend $10 billion over the next 7 years [27].

In the midst of all of this activity, the Predator has become the most famous if not most successful UAV program to date (see Figure 2-1). The predator has been in the news countless times as an illustration of the future of the military, the first step in the transition to wide use of unmanned aircraft for military missions. For its mission requirements, the Predator seems to have gotten the equation right, it has the right combination of capability, survivability and cost for the mission need, and thus it warrants examination.

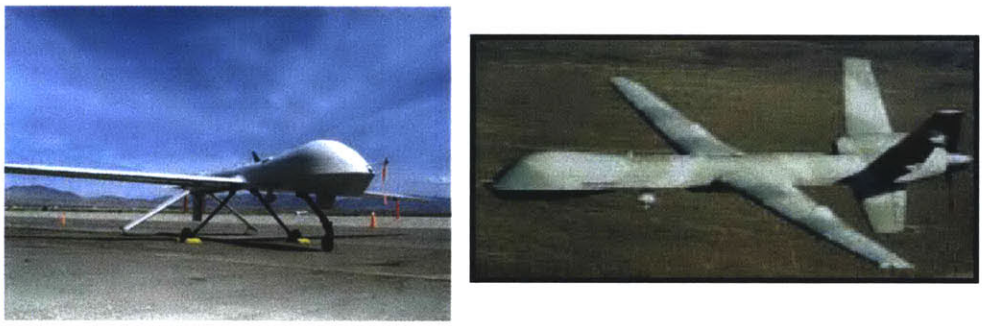

Figure 2-1: Predator [27], [28]

The RQ-1 Predators, built by General Atomics, was designed primarily for Intelligence, Surveillance and Reconnaissance (ISR) missions. The name RQ-1 indicates that it is a reconnaissance vehicle (R), that it is unmanned (Q) and that it is the first version of the vehicle (1). It has many on board sensors, including electrical-optical and infrared (EO/IR) sensors and synthetic aperture radar (SAR) and transmits streaming video by way of a data link, either through a line-of-site C-band data link or through a K_u-band satellite link.

The Predator is actually a system consisting of a ground station, 4 vehicles and a Predator Primary Satellite Link (PPSL). The Predator is considered a Medium Altitude Endurance (MAE) UAV. Its flight ceiling is 25,000 feet. It has a 100-horsepower turbo cooled engine (four cylinder Rotax engine) that gives it a cruise speed of 84 mph and a maximum speed of 135 mph. It has a maximum takeoff weight of 2,250 pounds and is capable of carrying a payload of up to 450 pounds. It has a range of 400 nautical miles and can stay aloft for over 24 hours [28]. An operator controls the predator continuously with a joystick on the ground, unlike semiautonomous or autonomous vehicles in which some, or all, of the mission is preprogrammed in an onboard computer.

Predator was developed quickly. Its development began in 1995 as a Defense Advanced Research Projects Agency (DARPA) Advanced Concept Technology Demonstration (ACTD) in 1993. This was a 30-month program consisting of 3 ground stations and 10 vehicles. Within six months of the initiation of the program the first flight test took place. Because of its relatively simple design and operation, it had very few glitches and it emerged quickly from its ACTD as a useful vehicle and was pulled into service before even finishing the program.

The Predator was first used in Bosnia in August of 1995, during which time it flew 130 missions, and had 850 flight hours. It quickly proved its military utility.
In 1996 it was given an upgraded airframe and the ACTD was considered complete. It entered production phase in August 1997 [29].

In 2001, the Air Force equipped Predator with the Hellfire air-to-surface missile, expanding its mission from reconnaissance to a strike weapon, and changed its designation from RQ-1 to MQ-1, where the M represents its new multi-role function.

Currently the Predator B is being developed, designated MQ-9 Predator (hunter-killer). The MQ-9 is larger than the MQ-1 (10,000lbs v. 2250 lbs), carries a much larger payload (3750 lbs v. 450 lbs) making it capable of carrying up to 10 hellfire missiles [30].

The Predator B had its first flight in February of 2001. Two vehicles were used in the development program and both were acquired by the DoD in October of 2001 [29]. There is current funding for the development of 9 more Predator B vehicles and Congress has expressed interest in increasing this.

In all, the Air Force had 60 Predators in 2002 divided into 3 or more squadrons. The price for each vehicle is in the range of ~$2.5-$4.5 million. The Air Force plans to spend $158 million to buy 22 more vehicles and associated systems over the course of 2003 [31]. The CIA also has an undisclosed number of Predators.

As of March 2, 2003, 80 known Predator vehicles had been deployed and of those, 28 have crashed. Since then, several more have crashed in the war in Iraq. Of these crashes only a few have been from enemy fire, the rest have come from manufacturing defects, weather related problems, and human error [32].

The Predator is not cutting edge technology, nor was it when it was developed. It was developed cheaply and quickly. Col. Edward Boyle, first commander of an armed Predator squadron, said, "Predator was built because it could be built. If you look at the technology it's a big model plane being flown by kids with a big model joystick. The technology that allowed it is C-band line-of-sight and K_u-band satellite technology" [25]

Due to its simplicity Predator is relatively cheap and reliable. Though many of them have been lost, because of their low price and utility they continue to be used extensively. The military considers them to be attritable and the demand for them by the armed forces is increasing. The predator fills a mission requirement more effectively and cost efficiently than anything else could. "In Iraq Predators are just sitting with those tank columns giving a visual picture of what's over the next mountain. That's why these things are so valuable especially with streaming video," said Col. Boyle [25].

The main takeaway from the Predator is that it effectively performs an important mission, but does so in a fairly simple and cheap manner. The Predator takes advantage of the fact that it is an attritable asset.

2.3 Global Hawk

The most sophisticated UAV to enter the military force mix to date is the RQ-4A Global Hawk (see Figure 2-2), developed by Northrop-Grumman. It was developed concurrently with another and even more sophisticated UAV called the RQ-3A DarkStar (see Figure 2-3), developed by Boeing and Lockheed-Martin.

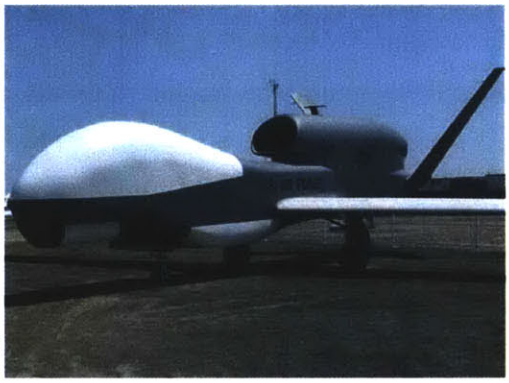

Figure 2-2: Global Hawk [33]

Figure 2-3: DarkStar [34]

It was not originally clear if these vehicles were being developed as compliments for the same mission or if they were in direct competition. However, in the end, Global Hawk was introduced into the force mix, and DarkStar was cancelled. The most fundamental difference between Global Hawk and DarkStar was the way in which each program handled the issue of survivability.

The mission they were designed for was that of a high altitude long-duration spy plane, meaning that it could loiter around at an altitude that gives it a broad perspective of the ground, more likely out of harms way, and could remain there for a long time. This capability is different from the Predator that is much lower and takes a much smaller snap shot of the area, and unlike a satellite it can cover areas for a long time and is not subject to the laws of orbital mechanics, which limit the amount of time a satellite can hover over an area.

The only existing capability that is similar to the role the Global Hawk or DarkStar were designed to fill is the aging U-2 spy plane. Currently it is said that there are only 50 pilots capable of flying the U-2. The missions are long and boring and uncomfortable because pilots are required to wear big heavy suits for 8+ hours at a time and the aircraft is difficult to handle. Thus these UAVs were expected by many to eventually take over some, if not all, of the role of the U-2.

The Global Hawk and DarkStar were developed under the auspices of a Defense Advanced Research Projects Agency (DARPA) ACTD program called the High-Altitude Endurance Unmanned Aerial Vehicle (HAE UAV) program. This program, which began in 1995, was an innovative new program initiated largely in response to the historical trend in UAV programs to significantly overrun their cost estimates [35]. The most significant attribute of this program was that it had a single requirement that industry competitors were required to meet: the unit flyaway price (UFP). This metric included the direct and indirect manufacturing costs and associated overhead. The UFP was set to $10million in FY1994 dollars. All other goals were flexible and left largely to the

discretion of the contractors [36]. Thus for the Global Hawk and DarkStar, because cost was fixed, only survivability and capability were traded.

The Global Hawk emerged capable of flying a mission 1200 nautical miles away, loitering there for 24 hours and then returning home. It is much larger than Predator, weighing 25,600 pounds, with a length of 44 feet and wingspan of 116 feet. It is capable of flying 400 mph at 65,000 feet with a payload of 1950 pounds [37].

In 2001 the Global Hawk entered the Engineering Manufacturing and Development (EMD) phase of defense acquisition. The Air Force acquired all seven of the full-scale vehicles used in the development program. Northrop Grumman delivered the last ACTD vehicle to the Air Force on February 14, 2003, and has since awarded Northrop Grumman $303 Million to deliver 6 more vehicles (4 to the Air Force and 2 to the Navy) and associated equipment (sensor packages, control equipment, etc.) [38].

The Global Hawk, though designed to have some stealthy attributes, generally has very poor low observable attributes. The DarkStar on the other hand was fitted with all of the most advanced stealth technologies.

The DarkStar emerged much smaller than the Global Hawk, weighing in at 8,600 pounds. During a mission it would be capable of flying 500 nautical miles and remaining aloft for 9 hours. The DarkStar was designed to fly at up to 350 mph at 45,000 feet, with a payload of 1,000 pounds [39].

DarkStar's first test flight took place on March 29, 1996 at Edwards Air Force Base (AFB). On its second test flight one month later, it crashed. It was subsequently modified to increase stability and flew again June 1998, but in 1999 the program was canceled [27].

The developers of Global Hawk and DarkStar took two drastically different approaches in attempt to balance survivability, cost and capability to develop the right vehicle for

current needs. Developers of DarkStar believed that in an environment where radar-guided surface-to-air missiles are increasing in abundance, high survivability should be a high priority. This belief was encouraged by many in the Air Force and DoD who were saying the same thing. The Global Hawk, on the other hand sacrificed survivability for increases in payload and endurance.

Why did Global Hawk win? The simple answer is because when it came to the military ranking their priorities with their money they chose capability over survivability. In the discussion of design goals at the beginning of the HAE UAV program the military had indicated that they wanted a stealthy reconnaissance vehicle in addition to other capability goals and the UFP cost requirement; however, when it came to priorities, survivability was not on top, payload and range were. Global Hawk had three times the capability of the DarkStar for the same cost. The payload of DarkStar was considered to be too small and its range too short. Undoubtedly there were other issues involved that led to Global Hawk's success and DarkStar's failure, but this was the primary reason. The Defense department recently validated this in the UAV Roadmap, in which it was said, "[DarkStar] was canceled for reasons that included its performance shortfall outweighing the perceived value of it enhanced survivability" [27].

Global Hawk ended up coming in at a UFP of $15 million. Though higher than the original UFP, this cost is still lower than the expected $20 million for a new production of the U-2 and the maintenance costs of the Global Hawk are expected to be much less than what they are for the U-2 [40]. Of the eight Global Hawks that had been built as of the beginning of 2003, 3 have been lost and none of these to enemy fire. However, demand still exists and production is proceeding. The Global Hawk has found a niche in the force mix by being a cheaper and more desirable alternative to an existing technology.

The Global Hawk, like the Predator, is considered to be an attritable asset, however, due to its greater expense, it is considered less attritable than Predator. Its crashes caused ripples in the development program and questions about its future arose [41]. In the end,

and with its recent successes in Afghanistan and Iraq and the aging U-2 fleet, however, it appears that the Global Hawk has also managed to get the cost-capability-survivability equations right.

Like Predator, Global Hawk is, for the most part, not cutting edge technology. Cutting edge technology quickly drives up the price, and had Global Hawk been more expensive, the three crashes may have been fatal to the program.

The Primary takeaway from Global Hawk and DarkStar is that survivability is only desirable in unmanned air vehicles so far as it does not significantly drive up costs or limit other capabilities.

2.4 lessons of UAVs

In both cases, Survivability was not the highest priority – capability and cost were. The most valuable attribute of Predator and Global Hawk is that they are attritable, and both took advantage of this fact. As both programs have evolved and more vehicles have been put in service, both have incurred high rates of attrition. However, because in their development programs attrition was properly accounted for, they have been able to sustain these losses and demand for them has continued to grow.

3 THE UCAV AND THE MILITARY

3.1 Introduction

The experiences of recent UAV programs can be instructive as decision makers involved with UCAV development programs try to decide how best to balance the cost-capability-survivability equation to meet the needs of the military. The Predator and Global Hawk found their niche in the force mix; developers exploited the fact that they are attritable and made a vehicle that could cost effectively complete a valuable mission. Though the mission requirements for the UCAV will be different from those of the UAV, the UCAV also has a niche in the force mix and it will be important that this niche be exploited. To understand the role of the UCAV in the force mix, it is necessary to look at the mission requirements placed on the UCAV, its proposed capabilities, the existence of alternative assets that can also fulfill the same mission, and the current threat environment.

3.2 Proposed Capabilities and Mission Requirements

The proposed UCAV mission capabilities have varied greatly over the last several years and they continue to change rapidly (as will be discussed further in the next chapter). Nevertheless, certain expected attributes of the UCAV have pervaded most proposals. At a minimum, the UCAV is to be autonomous, capable of carrying munitions, capable of extended duration missions or a long combat radius, highly maneuverable and inherently stealthy.

The UCAV is to take off, perform a mission or multiple missions, and land all on its own by way of a pre-programmed onboard computer. An operator is to monitor the UCAV mission from a control station but will only be concentrating on aspects of the mission such as mission changes and weapons delivery. The UCAV must be capable of carrying a payload sufficiently large to handle an array of existing munitions; particularly it should be able to carry one or more of the 1,000 lb – 2,000 lb Joint Direct Attack Munitions (JDAMs). The UCAV is to be a high endurance vehicle, capable of sustaining missions of great distances and long durations. Just how far and how long has varied, but in

general it has been proposed that these numbers should be multiple times greater than the current endurance and combat radius of the average piloted fighter aircraft. UCAVs have the potential to be much more maneuverable than piloted aircraft. They would be capable of performing violent maneuvers necessary to avoid enemy fire, maneuvers that could potentially kill a pilot [42]. Finally, the UCAV will be inherently stealthy. With no pilot, canopy, and all of the support systems that accompany a pilot, UCAVs can be much smaller than their manned counterparts, and can be designed with fewer angles toward vertical; both advantageous characteristics for avoiding radar [43], [44].

The mission capabilities of a UCAV have been described as dull, dirty, and dangerous; dull because they are to be capable of operating for very long periods of time, covering great distances at high altitudes; dirty because they are to be capable of going into situations in which biological, chemical, or nuclear weapons have been used, places manned aircraft would not be able to fly without jeopardizing the health and safety of the pilot; dangerous, because they could be used for high risk missions. The most dangerous missions that manned pilots currently fly are Suppression of Enemy Air Defenses (SEAD) missions. These are missions that usually take place during the first days of combat and target enemy surface-to-air missile (SAM) systems, and these are the missions for which the military is hoping to first use the UCAV.

SEAD missions are becoming even more dangerous in the minds of military personnel as new and more sophisticated defensive threats are beginning to emerge. These threats provide further motivation for using an unmanned aircraft. As stated by Col. Boyle, "You start to get to the point in time where everyone is leaping each other on the threat. Why did we come up with stealth? Because people came up with SA-10s. Why are we going to the next generation? Because people came up with SA-12s. Why are we doing this? Everyone started talking about UAV and UCAV when they started talking about the fourth and fifth generation threat of ground-to-air. This problem makes it become so extremely costly to counteract. When you can no longer, with the systems that you have, guarantee that you're going to get 100% out, you start thinking to yourself, is there a better way to do this?" [25]

As a result of the proposed capability of the UCAV, the emerging defensive threat, and most importantly, the fact that the UCAV removes the pilot from harm's way, the UCAV has gained much support from the military and DoD. A prevalent attitude of the military is the following, "If I can use a UCAV for the same mission I would use a strike eagle or a hornet for, if I lose a UCAV I ask myself did I do a good job planning the mission or did I screw up, instead of having to call some parents up and tell them I got their kids killed. When you start talking about the UCAV, what a lot of people have talked about in the military is the fact that the threat has become so high that before you want to risk putting a person into it you'll use something that allows you to say, 'I lost one, but the other three got it.' And you don't care. Writing letters is not a good thing" [25].

Thus, the potential value of the UCAV will come primarily from its ability to effectively fulfill a vital mission while keeping military personnel out of harm's way.

3.3 Competing Assets

The UCAV's greatest attribute then is that it is attritable. For this reason, it will always be of great value. However, its ultimate value will also depend upon the existence of alternative assets in the military force mix that can complete the same mission and will depend on the general nature of the threat for which it would be used.

3.3.1 Competing Capabilities

For SEAD missions, the primary competition to the UCAV for procurement dollars will come from cruise missiles and piloted fighter-bomber aircraft, the two assets currently used for SEAD missions.

The cruise missile is considered by many to be the first unmanned vehicle, albeit a single-use UAV. Because it is a single-use weapon, it is considered expendable and so appropriate for very high-risk situations. As was seen in the recent war in Iraq, in which hundreds of cruise missiles were used, this is a valued attribute. What the cruise missile

lacks is versatility. The UCAV's strength lies in the fact that it could be used in dangerous missions and would be more capable than the cruise missile. The UCAV could adjust in flight to moving targets, hover over an area till the target is located and move in quickly, provide damage assessment, etc.

Lockheed-Martin is currently developing a new, versatile and relatively cheap manned fighter-bomber called the Joint Strike Fighter (JSF). The JSF is a highly versatile aircraft which comes in three variants: an Air Force version, Navy version and Marine version, in order to account for each services' unique needs. It is thought that the JSF could eventually replace the F-16, A-10, F-18, and the Harrier. Because the JSF and UCAV are emerging for use at roughly the same time (the JSF is expected to be ready for EMD a couple years before the UCAV), they will likely be in direct competition with each other for procurement and use [51]. The JSF, because it is piloted, will obviously be much more capable and versatile than the UCAV, better able to react to changing conditions, mission adjustments, etc. The UCAVs advantage described above is simply that it won't put a pilot at risk in dangerous missions.

With the current force mix, i.e. without the UCAV, the cruise missile is used for very high-risk missions and manned assets are used for lower risk missions that require greater capabilities than a cruise missile can provide. The UCAV would be more flexible and capable than a cruise missile and more readily attritable than a piloted aircraft.

3.3.2 Competing Costs

Because there will be overlap in ability of the UCAV, cruise missile and JSF (or other manned assets), the price with which they can complete a mission compared to the perceived value added by their capabilities will impact which asset is selected.

The UCAV was originally envisioned to cost about 1/3 as much as the JSF, or about $10 million. In addition, the operation costs for UCAVs are expected to be about 75% less than they are for manned aircraft. This is largely because the UCAV would not require constant pilot training; simulators would be identical to the controls actually used to

operate the aircraft and thus will virtually eliminate fuel and maintenance costs associated with training. Currently the Air Force spends about $1 billion annually training F-16 pilots alone [45]. Cruise missiles, such as the Tomahawk, each cost about $1 million. The UCAV could deliver bombs that cost about $2,000 each and would be equally or more effective.

The cost estimates of the UCAV are beginning to rise, however, and some have now estimated that a UCAV like the ones currently being developed could cost as much as $30-40 million. As the costs of the UCAV increase, its value as an alternative to using piloted aircraft or cruise missiles may be less clear. In the words of an engineer with Lockheed Martin, "If they could actually fulfill a combat role in the force mix for $10 million, that could be a threat to JSF, there's no doubt. But with fly away costs of $30-40 million, it's not a threat, because a manned asset is going to be able to outperform and have more capability than an unmanned asset in the near term" [25].

Additionally, as the expected cost of the UCAV cost rises, it would take a greater number of missions before the UCAV becomes a cheaper alternative to the cruise missile. And if the attrition rate of the UCAV is as high as that of current UAV programs, it is not obvious that the UCAV would be a cost saving alternative to the cruise missile.

By making a very expensive aircraft the UCAV loses some of it niche value. In very high-risk missions, the cruise missile will be the alternative because it's cheaper and less is risked by using it than by using a UCAV. In low risk missions, a piloted asset will be used because it is more capable and not much is saved in the way of cost by using a UCAV instead.

3.4 The Current Threat Environment

An expensive UCAV loses its value and is only more valuable than its alternatives when the risk is very high, and a greater capability than that provided by a cruise missile is needed to assure success. In such a case, cost would be less of a factor and capability and

saving human life would be given a much higher priority. This would be the case if the adversary were a wealthy and technologically advanced group.

With the end of the cold war and the emergence of new and very different security threats, coupled with rapid advances in technology, the Department of Defense and the various military branches have rightly proposed a major shift in the way the military thinks about and conducts defense planning. Where there was once a clearly defined enemy, the Soviet Union, and where there was once a clear defense objective, military strength to deter Russia, there is now uncertainty regarding where threats will come from, and what form these threats will take. The National Security Strategy of the United States of America and the 2001 Quadrennial Defense Review Report both emphasize the need to develop new military systems that take the risk and uncertainty of asymmetric threats into account [46], [47], [48]. Where asymmetric threats means threats posed by terrorists groups and 'rogue' nations.

With asymmetric threats that have fewer and less technologically advanced defensive capabilities, it is possible for the military to plan around dangerous missions and still be successful. This was witnessed recently in the war in Iraq where the U.S. simply by-passed certain areas in order to avoid the threat. In other instances, cruise missiles can be used instead of manned aircraft, etc. With this flexibility, the military is able to more narrowly define what is attritable, and though the pilot will always be the primary determinant, cost or the desire to save an asset for another purpose can enter in to the planning.

Though a well prepared military will prepare for all scenarios, recent experience suggests that the military is right to plan heavily for asymmetric threats. An expensive UCAV may not be as valued in this type of environment as it would be if the perceived threat were more similar to that of the cold war or from a technologically advanced nation.

3.5 Conclusion

As shown above, a niche does exist for the UCAV within the force mix. However, the degree to which the UCAV takes advantage of that niche will depend upon the ability of developers to optimally balance cost, capability and survivability. The speed with which the UCAV will be introduced into the force mix and in what quantity and capacity it will be used will depend upon how well developers exploit the UCAV's niche. The strongest attributes of the UCAV are that it is more capable than a cruise missile and more attritable than a piloted vehicle. The UCAV can best take advantage of these attributes by focusing little on survivability and much on keeping costs low. The cruise missile and JSF should serve as rough guides as developers try to find the correct balance to the cost-capability-survivability equation.

4 UCAV DEVELOPMENT PROGRAMS

4.1 Technology Demonstrators

Currently, several UCAV prototypes are being developed. The Air Force and Department of Defense have been the primary supporters of these programs but the Navy continues to become more involved in UCAV programs as well. The primary contractors in developing these vehicles have been Boeing and Northrop-Grumman.

The UCAV was originally being developed as an Air Force vehicle only. The Navy was in the process of developing a UCAV-N for its purposes, but fewer resources were being devoted to this program and it was behind the Air Force program in terms of when an operational vehicle was expected. This was in large part due to the additional requirement the Navy has which is that the vehicle be able to safely and reliable land on an Aircraft Carrier.

In March of 1999, DARPA and the Air Force awarded Boeing a $116 million contract to develop a prototype UCAV called the X-45A, see Figure 4-1. The first test flight of this aircraft took place on May 22, 2002 [49]. The X-45A has a wingspan of 34 feet; it is 27 feet long; and it stands 7 feet tall. It weights 12,000 lbs and is capable of carrying 1,500 pounds. This UCAV is designed to fly mach 0.8, or about 500 miles per hour at 40,000 feet. It has an endurance of about 1.5 hours. Of the UCAV prototypes currently in existence the X-45A is the most advanced in terms of its development. The X-45A was designed to show that a UCAV could "effectively and affordably prosecute SEAD in a 2010+ threat environment" [50]. It was originally estimated to have a fly-away price of about 1/3 that of the JSF or about $10 million [42].

Figure 4-1: The X-45A

Both Boeing and Northrop-Grumman have developed technology demonstrators for the UCAV-N program, doing so largely with their own funding. Boeing has the X-46, and Northrop the X-47A Pegasus, both to demonstrate the technological feasibility of developing a vehicle with the requirements needed by the Navy. The X-47 had its first flight on February 23, 2003.

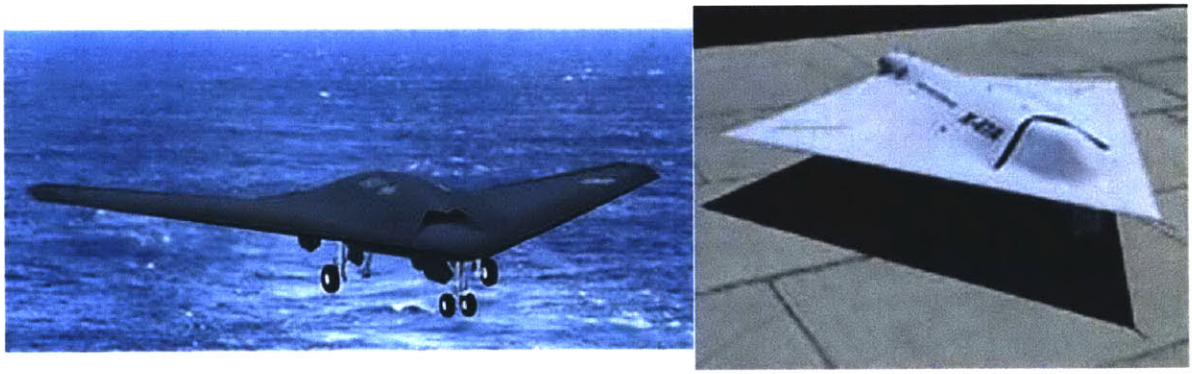

a) b)

Figure 4-2: a) X-46 and b) X-47A

The UCAV-N was expected to be much larger than the X-45A, and to have greater capabilities. It was estimated to be 34 feet long with a wingspan of 54 feet, to have a gross-takeoff-weight of 29,000 pounds, and to capable of carrying a payload of 5,500 pounds. In addition, It was to have a flight ceiling of 40,000 feet and a radius of 1,500 nautical miles and an endurance of 12 hours. The first test flight of the X-47A took place on Feb 23, 2003. The cost of the UCAV-N was expected to be about ½ that of the JSF [27].

All of these programs are rapidly evolving and new announcements are coming almost daily. In March of 2003 the Defense Department issued a UAV Roadmap in which it announced the creation of a new joint UCAV office, in which the DoD, Air Force, and Navy will work together on UCAV development [27]. This office is to become operational in October of 2003. Also in the Roadmap, it was announced that the X-46 and X-47A would be a part of a competition to meet both Air Force and Navy requirements.

In late April, DARPA announced that instead of the X-46 and X-47A, it has asked Northrop-Grumman to move forward with a new design called the X-47B and asked Boeing to move forward with the X-45C in order to compete for a UCAV capable of filling both services' requirements. This new program is being called the Joint UCAV (J-UCAV) [52].

Though in its initial stages, the program appears to be shaping up in much the same manner as the JSF competition between Boeing and Lockheed Martin in which both companies where asked to make a vehicle which would have a high degree of commonality but which could be modified to meet the specific requirements of the Air Force, Navy (carrier landings), and Marines (vertical takeoff).

The common objectives for the J-UCAV are a combat radius of 1300 nautical miles, a payload of 4,500 pounds, the ability to loiter for two hours over a target up to 1000

nautical miles away. The vehicle is to be developed with an autonomous control system [53].

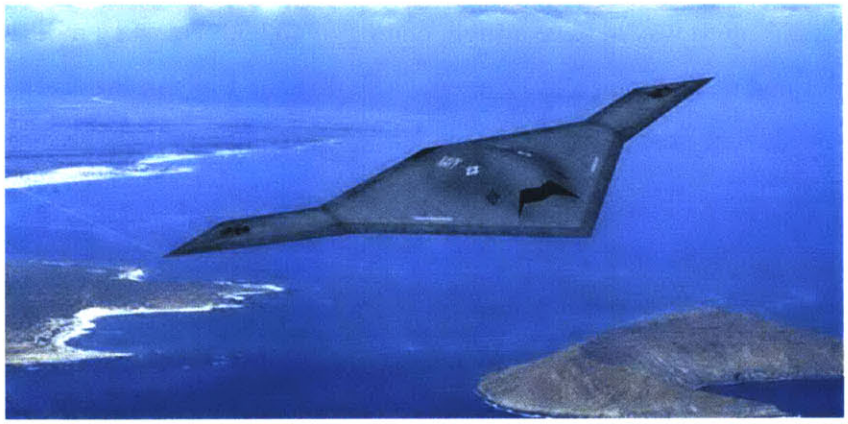

Figure 4-3: X-47B

DARPA will provide Boeing with funding of up to $140 million to proceed with the development of three X-45C vehicles, and will fund Northrop Grumman up to $160 million to proceed with the development of two X-47B vehicles.

The X-45C is the third Boeing vehicle in a progression of larger more capable and stealthier vehicles. The X-45B has an area two-thirds greater than the X-45A and a one-third greater weight, making it about the same size as an F-16. It was also designed to be stealthier than the X-45A. The X-45C then builds upon the X-45B. According to a press release from Boeing on April 29, 2003, "the X-45C Air Force design will be based on the subsystems and center body of X-45B design, but with a revised planform that carries more fuel and provides better aerodynamic performance. With its increased fuel volume, the X-45C will have a combat radius of more than three times the X-45B carrying the same payload…The X-45C will also have a larger payload capability, including the ability to carry two 2,000-pound Joint Direct Attack Munitions (JDAMs)…The X-45C design for the Navy will be based on the Air Force X-45C air vehicle, but will include changes required to assess potential carrier suitability and other Navy-unique needs. These changes relate to structure, landing gear, tail hook mechanism and advanced avionics required to demonstrate precision approach and landing" [54].

The X-45C will weigh 35,000 pounds with a payload capacity of 4,500 pounds. It is expected to be able to fly 1,000 nautical miles and loiter there for up to two hours. It will have a flight ceiling of 40,000 feet and fly Mach 0.85. Its first flight is expected to take place in late 2005. According to the DoD, the X-45C will add more stealth characteristics [54].

Few details have been released detailing the new X-47B design, however it is also designed to be highly stealthy and meet the commonality requirements. Its first flight is scheduled for early 2006.

4.2 Conclusion

The X-45A is moderately stealthy but, more like Global Hawk, the original focus of the program was to provide a cheap vehicle that could meet a mission need. No official cost estimates of the new X-45C or X-47B vehicles have yet been released. However, It is estimated by some in the aerospace industry that the X-45C may cost as much as $40 million a copy and it can be assumed that the X-47B would be similar.

In going to a more expensive and more highly survivable vehicle, these UCAV programs risk making the same error as DarkStar. 'Mission creep' continues to drive the cost of the vehicle higher and higher. By making a more expensive and highly survivable vehicle, these programs may begin to erode the UCAV's advantage of being a cost effective alternative to the cruise missile or JSF.

The UCAV's niche is in the fact that it is attritable. As they become more highly survivable due to mission creep they run into conflict with other weapon systems, thus moving out of their niche. If all developers go this route, development of the UCAV will ultimately be slowed because when these UCAVs mature and get to the point where the military has to decide whether to buy a squadron of expensive UCAVs or a squadron of JSFs, or more cruise missiles, they are likely to choose away from the expensive UCAV.

Like the Global Hawk, a program that makes a cheaper UCAV, that focuses less on survivability and takes advantage of the new equation, could likely out compete a very expensive, highly survivable UCAV for military procurement dollars when the military once again ranks it priorities with its money.

There is little doubt that the UCAV will eventually become a large part of the force mix, stimulating many revolutionary changes as it comes, however, how soon the UCAV becomes a significant part of the force mix, and what its ultimate role will be when it does so, will depend on how well the development programs handle the cost-capability-survivability equation. By neglecting to take full advantage of the survivability part of this equation, current development programs are moving away from optimum. This will likely slow the UCAVs ultimate emergence and perhaps open the door to a competitor who better handles the equation.

5 FLOW CONTROL: AN ENABLING TECHNOLOGY

5.1 Introduction

Active Flow Control is a technology that can help the UCAV to achieve its survivability goals while reducing cost and increasing capabilities. It can do this by allowing designers to make more aggressive serpentine inlets, which will allow the UCAV airframe size to be reduced and system performance to be maintained or improved. As was mentioned in chapter one, if the curvature of the inlet is too severe, or the diffusion too aggressive, flow separation can occur which results in unsteadiness, distortion, and a loss of pressure recovery at the AIP. The remainder of this thesis focuses on using flow control techniques in a $1/6^{th}$ scale Northrop-Grumman UCAV to mitigate such a separation and its effects, both steady and unsteady.

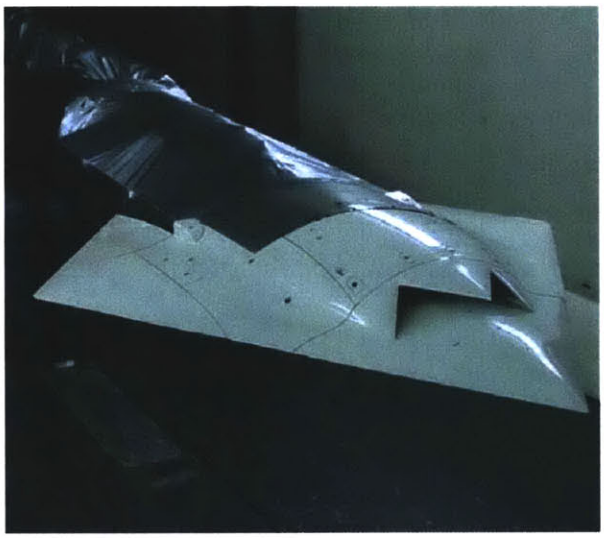

Figure 5-1: $1/6^{th}$ Scale UCAV

5.2 Description and Physics of UCAV Inlet

The UCAV model used in these studies features a top-mounted, serpentine inlet with varying cross-sectional geometry. Because of the severity of the internal curvature, at moderate mass flows adverse pressure gradients cause the flow to separate from the

surface of the diffuser. In previous studies the details of the structure of this separation were examined and are documented by Brear [19].

Brear *et. al* clearly show how the CFD predictions shown in Figure 5-2, together with oil-flow visualization results in the experimental apparatus, shown in Figure 5-3, elucidate the physical mechanism of the separation. Two large counter-rotating vortices form at the top of inlet in the reverse-flow region downstream of the separation line. The 3D morphology of the separated region (in contrast to typical 'separation bubbles' one sees in 2D diffusers) generates a longitudinal vortex pair that extends downstream, and is subsequently observed in the upper quadrant of the AIP [7]. Brear *et. al* conclude that the separation results from a strong adverse pressure gradient, appears to be strongly unsteady, and may respond to freestream disturbances. He argues that the longitudinal vortices result from flow separation, and demonstrates that they are largely responsible for the poor pressure recovery and increased distortion and unsteadiness measured at the AIP. These vortices periodically form, shed, and convect downstream to the AIP. The characteristic frequency of this shedding has been studied in greater detail by Braddom who has shown the shedding frequency to range from 650Hz to 900Hz for mass flows of 2.9-3.3 lb/s (these are the cruise mass flow conditions for the 1/6th scale inlet) [20].

Although the Mach numbers in our experiments were similar to flight conditions in this study, Reynolds numbers were not. However, Brear *et al.* argue that the effects seen in this inlet are not likely to be strongly dependent on Reynolds number. For instance, as mass flow through the inlet is increased, the pressure recovery at the AIP is found to decrease. If Reynolds number effects dominated, we would expect the opposite trend: Reynolds number increases with increased mass flow, which typically results in reduced boundary layer thickness. This in turn would result in an increase, not a decrease, in pressure recovery. Thus we expect the trends and effects measured in the inlet to be consistent with the full-scale system.

a)

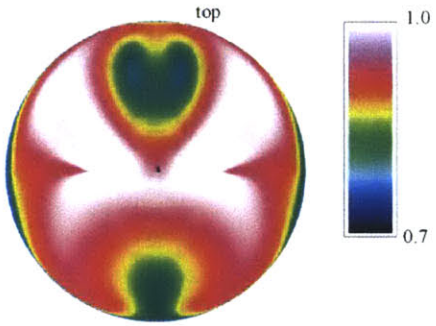

b)

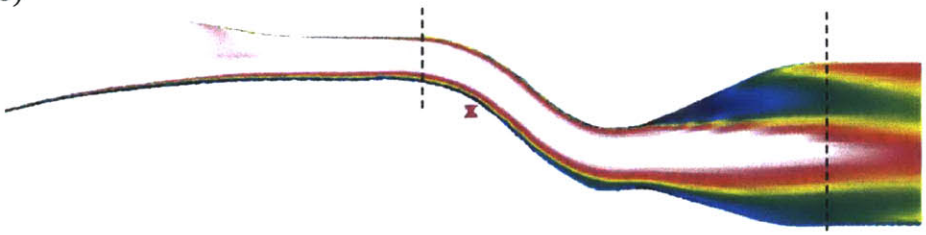

Figure 5-2: a) Predicted Contour of Total Pressure Recovery at the AIP and b) Along the Center-Plane of the Inlet

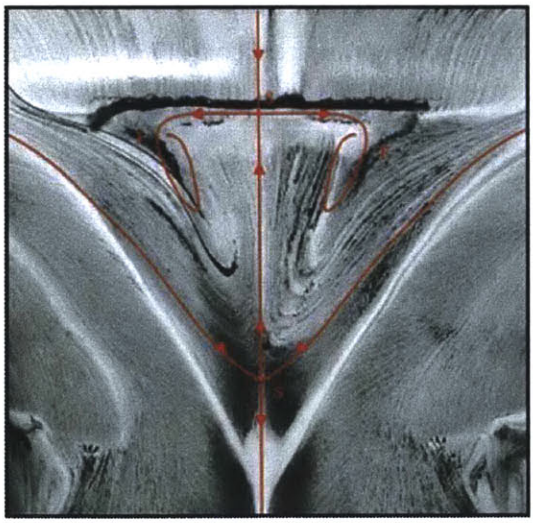

Figure 5-3: Flow Visualization of Separation

Figure 5-4 shows the total pressure profile at the AIP for an inlet mass flow of 3.1 lb/s (corresponding to cruise conditions) without actuation of any kind. As can be seen from

the figure, there is a large distorted region in the top quadrant and a smaller distortion at the bottom. The area averaged total pressure recovery is 95.6%, where average pressure recovery is the measured total pressure at each probe location divided by the upstream total pressure averaged across all 80 probes.

$$\text{Pressure Recovery} = \frac{1}{n}\sum\frac{P_t}{P_\infty} \tag{5-1}$$

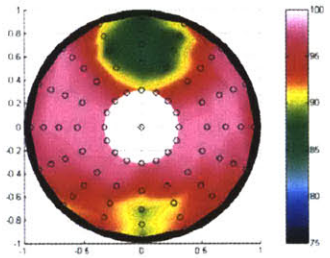

Figure 5-4: Contour of Pressure Recovery at the AIP for an Inlet Mass Flow of 3.1 lb/s

The area averaged total pressure recovery in the top quadrant, which contains the large distorted region, is 93.25%. Because flow control in the bottom of the inlet was not considered in the present studies, the pressure recoveries in this thesis will be reported for the upper quadrant.

For a more detailed account of the inlet flow physics see references [19], [22] and [23].

5.3 Overview of Experiments

The remaining chapters, chapters 6-10, discuss work done as an extension of the comprehensive study mentioned in chapter 1. Experiments to capture the unsteadiness in the inlet through the use of upstream wall-based sensors, for use in a feed-forward control scheme with compressor face actuation, are discussed in section 2. Section three is a discussion of experiments performed in order to suppress the separation, or reattach the flow, in the inlet in attempt to improve the steady effects of the separation, loss of pressure recovery and distortion.

SECTION 2 – WALL SENSORS FOR USE IN CONTROL SCHEMES

6 FIR WIENER FILTER

6.1 Overview

In this chapter an experiment is described in which data is collected from sensors in the separated region of the flow and at the AIP of the $1/6^{th}$ scale UCAV prototype. The optimum transfer function between the inputs and output is computed and a filter is constructed in the manner of Rathnasingham and Breuer [17].

As mentioned in chapter one, reducing the unsteadiness at the AIP was a major thrust of the comprehensive study performed at MIT. Warfield showed that reduction of unsteadiness is possible if information from the AIP is available. Warfield placed actuators downstream of the AIP in order to simulate compressor face actuation. Using an unsteady total pressure probe placed at the AIP and the actuators, Warfield was able to reduce the local unsteadiness at the AIP through the use of feedback control [18]. However, in a real application it is not possible to place a probe at the compressor face and thus information about the unsteadiness must be obtained in another way. The present study attempts to use hot-film sensors placed in the separated region, which measure the shear stress of the flow, to obtain such information. Because these sensors are upstream of the compressor face, they could be used in a feed-forward control scheme with compressor face actuation to control the unsteadiness in the system.

The objectives of this chapter are:

- To develop a linear predictive filter that can be used in a control loop to predict the propagation of large-scale coherent structures, formed in the separated region, to the AIP (i.e. to test the Rathnasingham/Breuer concept in this 3D inlet with high Reynolds numbers and realistic Mach numbers), for use in a feed-forward control scheme with compressor face unsteadiness rejection control.
- To use Wiener filtering techniques to improve the correlation between sensors in the upstream separated region and at the AIP, and thus the ability of upstream sensors to predict compressor face conditions in order to optimize the system and better understand the limitations and issues.

- To determine the optimum number and placement of hot-film sensors to use in order to make the system more realistic.
- To demonstrate the robustness of the filter to predict flow conditions at the AIP over varying inlet mass flows and atmospheric conditions, again in order to understand the limitations and issues of this approach.

The test setup (see figures 6-3 and 6-4) consisted of the $1/6^{th}$ scale UCAV model with an attached bellmouth to condition the flow to simulate cruise conditions. Airflow was pulled through the bellmouth and UCAV inlet with a De Laval air compressor and mass flow was regulated with a calibrated variable mass flow plug. A sensor array, consisting of 30 hot-film sensors, was mounted flush with the top of the inlet in the separated flow region, and several unsteady total pressure probes were placed at the AIP [20].

A finite impulse response (FIR) filter was constructed using multiple hot-film sensors as inputs and a single total pressure probe as the output. The filter was then applied to various combinations of hot-film sensors (both varying number and location) and tested over varying inlet mass flows and atmospheric conditions.

6.2 Filter Construction Theory

The filter that is used here is essentially an FIR Wiener filter with the only difference being that in this case the spectral characteristics of the signal and the noise are not separately known as they are in a traditional Wiener filter.

For an input signal that is an additive combination of the signal and noise, a Wiener filter performs a linear operation to separate the signal from the noise. The Wiener filter is an optimizing least squares filter that minimizes the mean-square error between the predicted and the actual signal and produces an output signal that, in the case of a predictor, approximates the input signal at some later time without the noise [62].

The performance of the filter depends on the correlation between the input and the output signals. If the input and output are independent, the filter will be ineffective; if the input

and output are perfectly linearly dependant, the filter will give an exact prediction of the output signal.

In practice, for data sampled in discrete increments, the Wiener filter operates on the data with a set of pre-computed 'weighting values' to produce an approximation of the output signal. These weighting values constitute the filter.

Additionally, an FIR filter inherently provides a linear phase response. This is desirable for the present situation because it means that the delay through the filter will be the same at all frequencies, thus the filter does not introduce unwanted delays or distortions in the phase.

The system can be represented by the block diagram of Figure 6-1, where s is the signal at the separated region, P_t is the signal at the AIP, B is the FIR filter, $\hat{P}_{t_c}$ is the predicted signal at the AIP, t_{FIR} is the response time of the filter and τ_c is the convection time from the input sensors to the AIP. Note that the signal at the AIP is actually corrupted by noise, instrumentation error, etc. This corruption is represented here by n_p and was not accounted for in these studies. Also note that in order for this system to serve as a predictor, t_{FIR} must be less than τ_c.

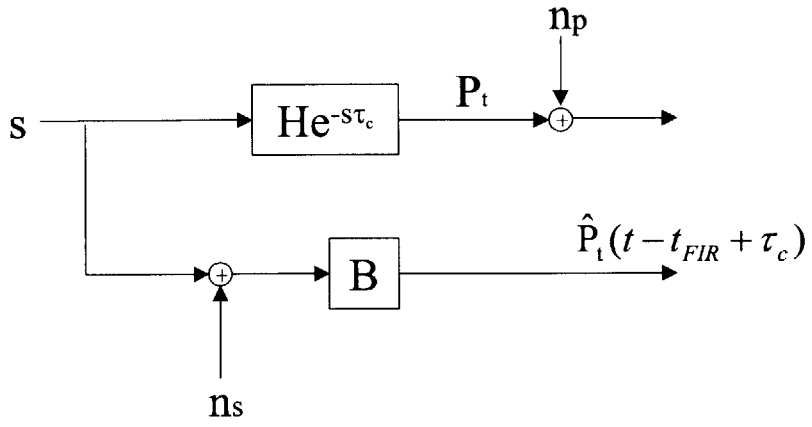

Figure 6-1: Block Diagram of the System

6.2.1 Assumptions

Our approach is based on the assumption that the primary source of distortion at the AIP is due to large-scale 'coherent structures' that form in the separated region, detach, and convect downstream. It is also based on the further assumption that the behavior of these coherent structures is statistically stationary and may be modeled as linear with respect to the mean flow. The findings described in chapter 5 make it clear that, for the case studied in this research, the assumption of large-scale coherent structures is justifiable. The stationary assumption is necessary so that the correlations used to make the filter will be constants in time. The linearity assumption, which need only apply for the time period it takes for the flow to convect from the hot film sensors to the AIP (for this inlet at flight cruise conditions this is about 1ms), is supported by several studies cited by Rathnasingham and Breuer [17]. In any case, the ultimate performance of the filter will give an indication of the validity of the assumptions.

6.2.2 Filter Construction

The input to the filter is a signal and noise combination that is discretely sampled over time. For the case presented in this research, the inputs are the discrete measurements from hot-film sensors in the separated region of the flow.

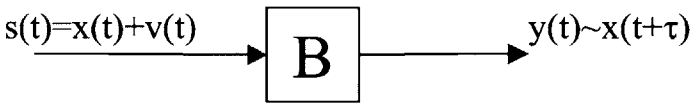

Figure 6-2: Wiener Filter

The filter output at time, t_n, can be written as a linear combination of the past measurements multiplied by yet-to-be-determined weighting constants, b_1, b_2, ..., b_n.

$$y_n = b_1 s_1 + b_2 s_2 + ... + b_n s_n \tag{6-1}$$

where s_1, s_2,...,s_3 represent past values of s at discrete intervals T.

For this research, the filter output is a prediction of the downstream signal (signal at the AIP) at time t_n. The following describes how the values of these weighting constants, b_1, b_2, ..., b_n, are found.

First, the filter error can be written as,

$$e_n = x_n - y_n = x_n - (b_1 s_1 + b_2 s_2 + ... + b_n s_n). \tag{6-2}$$

The mean square prediction error is,

$$\begin{aligned} E(e_n^2) &= E[x_n - (b_1 s_1 + b_2 s_2 + ... + b_n s_n)]^2 \\ &= E(x_n^2) + [b_1^2 E(s_1^2) + b_2^2 E(s_2^2) + ... + b_n^2 E(s_n^2) + 2b_1 b_2 E(s_1 s_2) + 2b_1 b_3 E(s_1 s_3) + ...] \\ &\quad - [2b_1 E(s_1 x_n) + 2b_2 E(s_2 x_n) + ... + 2bE(s_n x_n)]. \end{aligned} \tag{6-3}$$

To find the optimum values of b_1, b_2, ..., b_n that minimize the mean square error the derivative of both sides is taken and the left-hand-side set to zero. Ultimately the following set of linear equations is obtained.

$$\begin{bmatrix} E(s_1^2) & E(s_1 s_2) & \cdots & E(s_1 s_n) \\ E(s_2 s_1) & \ddots & & \\ & & \ddots & \\ E(s_n s_1) & & & E(s_n^2) \end{bmatrix} \begin{bmatrix} b_1 \\ b_2 \\ \vdots \\ b_n \end{bmatrix} = \begin{bmatrix} E(s_1 x_n) \\ E(s_2 x_n) \\ \vdots \\ E(s_n x_n) \end{bmatrix} \tag{6-4}$$

The left-hand-side contains autocorrelations for different values of delay; for example, $E(s_i s_j) = E\{s(t)s(t-T(j-i))\} = R(t-(j-i)T)$, where we have made the ergodic assumption [62]. The right-hand-side of equation 6-4 contains the cross-correlations between the input signals and the output signal value, for various values of delay (also called "correlation lag").

Thus equation 6-4 can be rewritten as,

$$\begin{bmatrix} R_{ss}(0) & R_{ss}(1) & \cdots & R_{ss}(n-1) \\ R_{ss}(1) & \ddots & & \\ & & \ddots & \\ R_{ss}(n-1) & & & R_{ss}(0) \end{bmatrix} \begin{bmatrix} b_1 \\ b_2 \\ \vdots \\ b_n \end{bmatrix} = \begin{bmatrix} R_{sx}(0) \\ R_{sx}(1) \\ \vdots \\ R_{sx}(n-1) \end{bmatrix} \tag{6-5}$$

This set of linear equations is known as the Wiener-Hopf equations.

These correlations can be obtained from data sampled at the separated region and at the AIP and thus the weighting constants, b_1, b_2, ..., b_n, can be solved for by inverting the left-hand-side matrix of equation 6-5. These weighting constants can then be used to filter subsequent hot-film data, and a feedback or feed-forward controller can be developed.

This same method can be easily extended to a multiple-input single-output (MISO) system. An example is given here for a three-input, single-output system.

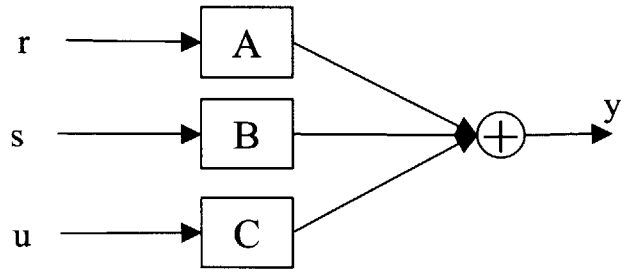

Figure 6-3: multiple-Input Wiener Filter

First the filter output at time t_n can be written as a linear combination of the past measurements from each input sensor multiplied by the yet-to-be determined weighting constants, A, B, and C.

$$y_n = \sum_{k=1}^{n} a_k r_k + \sum_{k=1}^{n} b_k s_k + \sum_{k=1}^{n} c_k u_k + \ldots \tag{6-6}$$

The filter error can again be written as,

$$e_n = x_n - y_n \tag{6-7}$$

and the mean square prediction error as,

$$E(e_n^2) = E\left[x_n - \left(\sum a_k r_k + \sum b_k s_k + \sum c_k u_k\right)\right]^2 \tag{6-8}$$

now expanding for terms containing b_l, recognizing that when the derivative is later taken with respect to b_l all terms not containing b_l will drop out,

$$E(e_n^2)\Big|_{b_l} = E\left[x_n^2\right] + 2\left[b_l \sum a_k E(r_k s_l) + b_l \sum b_k E(s_k s_l) + b_l \sum c_k E(u_k s_l)\right] - 2b_l E(x_n s_l) \tag{6-9}$$

The derivative of the mean squared error is then taken with respect to b_l,

$$\frac{\partial E(e_n^2)}{\partial b_l} = 2\left[\sum a_k E(r_k s_l) + \sum b_k E(s_k s_l) + \sum c_k E(u_k s_l)\right] - 2E(x_n s_l) \tag{6-10}$$

Setting the left-hand side to zero yields,

$$\sum a_k E(r_k s_l) + \sum b_k E(s_k s_l) + \sum c_k E(u_k s_l) = E(x_n s_l) \tag{6-11}$$

Performing this derivation for every a_k, b_k, and c_k yields the following set of linear equations,

$$\begin{bmatrix} E(\underline{r}\underline{r}^T) & E(\underline{r}\underline{s}^T) & E(\underline{r}\underline{u}^T) \\ E(\underline{s}\underline{r}^T) & E(\underline{s}\underline{s}^T) & E(\underline{s}\underline{u}^T) \\ E(\underline{u}\underline{r}^T) & E(\underline{u}\underline{s}^T) & E(\underline{u}\underline{u}^T) \end{bmatrix} \cdot \begin{bmatrix} \underline{a} \\ \underline{b} \\ \underline{c} \end{bmatrix} = \begin{bmatrix} E(\underline{r} \bullet \underline{x}) \\ E(\underline{s} \bullet \underline{x}) \\ E(\underline{u} \bullet \underline{x}) \end{bmatrix} \tag{6-12}$$

where,

$$\underline{r} = \begin{bmatrix} r_1 \\ r_2 \\ \vdots \\ r_n \end{bmatrix}, \qquad \underline{s} = \begin{bmatrix} s_1 \\ s_2 \\ \vdots \\ s_n \end{bmatrix}, \qquad \underline{u} = \begin{bmatrix} u_1 \\ u_2 \\ \vdots \\ u_n \end{bmatrix}, \tag{6-13}$$

and the ($\bullet$) on the right-hand side denotes element-by-element multiplication. The left-hand side of equation 6-12 thus contains the autocorrelations of each input along the diagonal blocks and the cross correlations of each input to every other input to fill in the matrix. The right-hand side contains the cross correlations of each input to the output. The weighting constants can then be found by inverting the left-hand side matrix.

For the system studied in this thesis, the inputs are the hot-film sensors sampled at discrete times and the output is the unsteady total pressure probe sampled at the same discrete times.

The size of these matrices obviously depends upon how many hot-film sensors are used and how many prior measurements are included. Once solved for, the filter coefficients are its impulse response; the longer the impulse response, the more accurate the prediction will be. However, the size of these matrices has consequences for the real-time implementation of this method. As the size increases the computational demands increase. The computational time can begin to come into conflict with the desired response time of the control system and may thus play a role in determining the ideal number of input sensors and number of samples.

6.3 Experimental Setup

6.3.1 Overview

In order to generate the input-output data necessary to create the filter, a hot-film sensor array, which provided the signal inputs, was placed in the separated region of the flow and unsteady pressure transducers, which provide the signal output, were placed at the

AIP. High subsonic flow was pulled through the inlet simulating flight cruise conditions, and data from the hot films and pressure probes was sampled. A description of the experimental setup and data collected follows.

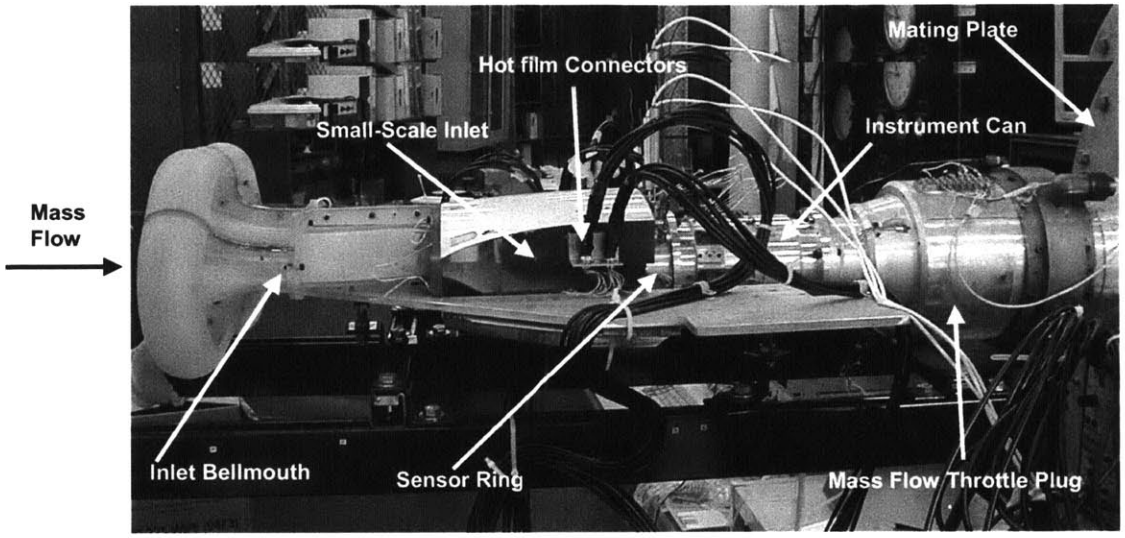

Figure 6-4: Experimental Setup

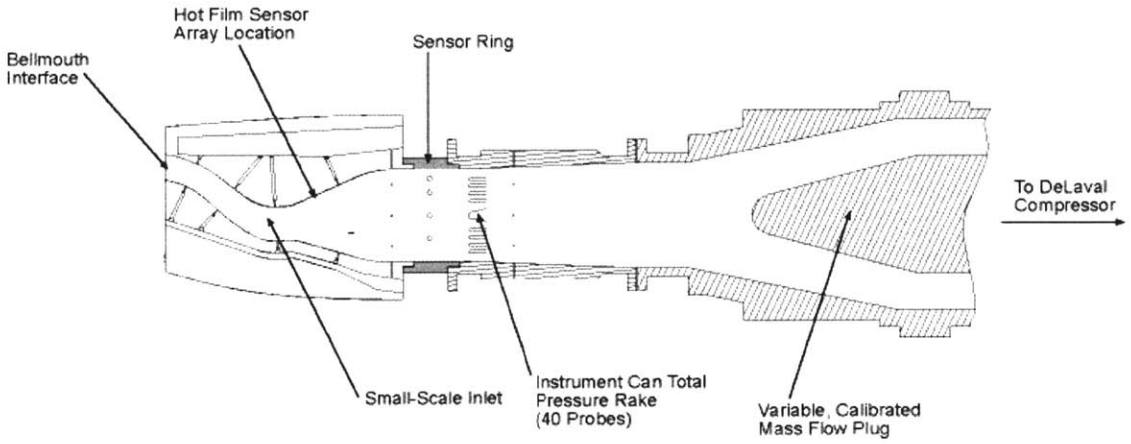

Figure 6-5: Schematic of Experimental Setup

6.3.2 Apparatus

The primary experimental apparatus are shown in figures 6-4 and 6-5. As can be seen from figure 6-4, the UCAV inlet lip has been replaced with a bellmouth to condition the flow and simulate cruise conditions. Mass flow was delivered through the UCAV inlet by way of an open system driven by a ~1 MW De Laval air compressor. The compressor is capable of pulling mass flows of up to ~13 lb/s through an inlet, however for all tests considered in this thesis the maximum mass flow used was 3.6 lb/s. The compressor inlet is fed by a 24-inch diameter pipe to which was mated a mass flow throttle plug. The mass flow throttle plug is used to set the mass flow through the diffuser. It has a cononical inner shape and a movable center bullet that is controlled by a stepper motor. The design of the plug made it possible to change the choking area, and thus the mass flow, by simply moving the plug back and forth in the axial direction. The static pressure just downstream of the throttle plug was measured and the ratio of the atmospheric pressure to this static pressure was maintained at a value of at least 2.0. This was done to ensure that the flow across the system was indeed choked (M=1). The throttle plug area was also kept smaller than the smallest area in the entire flow path to ensure that the flow was choking in the throttle plug, since the flow will choke at the point of smallest area.

6.3.3 Mass Flow Calibration

The mass flow can be determined by the following equation,

$$\dot{m} = \frac{P_T A}{\sqrt{RT_T}} F(M,\gamma), \tag{6-14}$$

where P_T and T_T are the total pressure and temperature respectively, A is the area at the chocking point and F is a flow function that depends only on M and γ. (M=1, γ=1.4, and R=287j/kg/K). Northrop-Grumman developed a calibrated relation between the throttle plug bullet position and the inlet mass flow, which was later updated by Warfield. A voltage was applied across a potentiometer in the throttle plug, which allowed the

position of the plug to be correlated to a voltage. Equation 6-15 is the relation between plug position, in inches, and the measured voltage:

$$x = 0.50398 * V - 0.29231 . \tag{6-15}$$

Similarly, a polynomial calibration curve was developed which relates mass flow through the inlet to the plug position. This curve was developed for a reference mass flow at specific reference conditions, P_{ref}=14.7 psia, and T_{ref}=533°R, and is defined by the following equation:

$$\dot{m}_{ref} = -0.0068x^4 + 0.049x^3 - 0.201x^2 + 1.355x - 0.016 . \tag{6-16}$$

Using these relations, the actual mass flow through the UCAV inlet can be calculated by correcting equation 6-16 for current atmospheric conditions. The units of mass flow, as it is presented here, are pounds per second (lb/s).

$$\dot{m} = \dot{m}_{ref} \frac{P_{atm}}{P_{ref}} \sqrt{\frac{T_{ref} + 460}{T_a + 460}} \tag{6-17}$$

6.3.4 Instrumentation

6.3.4.1 Sensor array

Hot-film sensors were placed in the separated region to capture the coherent structures in the flow for use in developing the filter. A hot film sensor is essentially just a metal strip that acts as a resistor in a bridge circuit. The electrical resistivity of the strip is related to its temperature. As air flows over the sensor heat transfer occurs, altering the resistivity of the metal. If a current is applied across the circuit such that it maintains a constant resistivity and thus temperature, the change in current can then be used to measure the heat transfer of the film. Heat transfer is related to the shear stress exerted by the air on the surface over which it is flowing and the shear stress is related to turbulent structures in the flow.

A Constant Temperature Anemometer (CTA) is used to maintain the hot film sensor at a constant temperature. It does so by way of a feedback loop that adjusts the current through the circuit to maintain a constant resistance. The CTA provides a voltage output indicating the change in current, which thus indicates the change in temperature across the hot-film and ultimately provides a measure of the instantaneous shear stress. The CTA system has a maximum frequency response of about 100 kHz, well above what is needed for the experiments of this research.

A hot-film sensor array containing 30 sensors was designed by Braddom and fabricated by SENFLEX®. For details of the design see [20]. Using the oil flow visualization results, the array was designed to cover the entire separated region. Figure 6-6 shows the placement of the sensors super-imposed upon the oil flow visualization of the separated region of the inlet. The mass flow for the case shown in the figure was 3.6 lb/s, the greatest mass flow tested, which therefore had the largest separation.

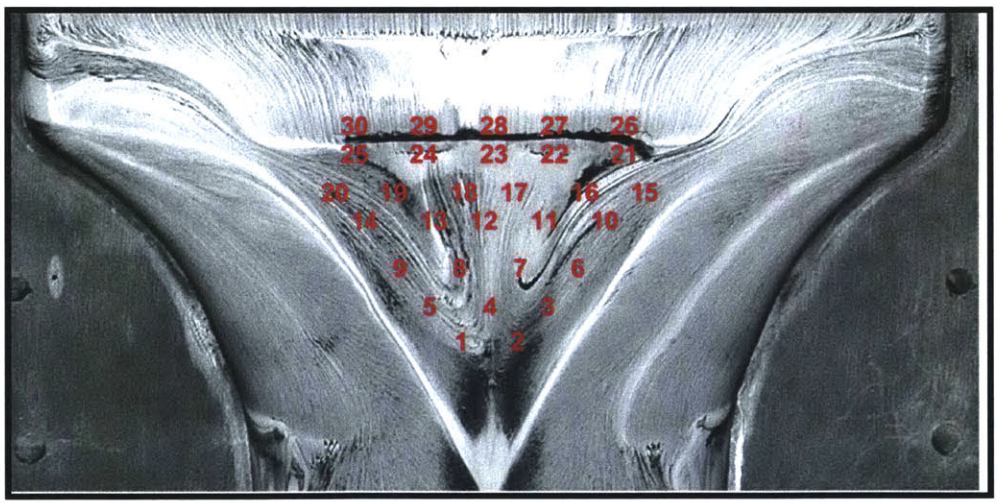

Figure 6-6: Sensor Locations Superimposed on Oil Flow Visualization of the Separated Region of the Inlet

The hot-film array was designed to have span-wise symmetry in order to study the vortex pair discussed earlier. A greater density of sensors was placed near the flow separation

point for greater resolution of the stagnation point. The exact placement of each sensor is given in table 6-1, as measured from the coordinate origin shown in figure 6-7. The coordinate origin corresponds to static pressure tap 225 in the inlet. The number of sensors used in this study was limited by cost, minimum lead wire width, and the available number of CTA bridges.

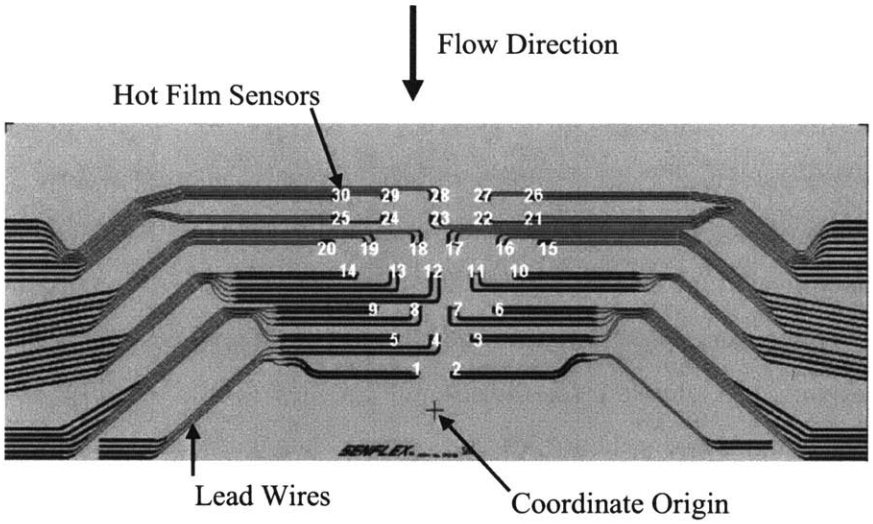

Figure 6-7: Hot-Film Sensor Array

Hot Film Sensor Coordinates

Sensor Number	X-Coordinate (cm)	Y-Coordinate (cm)	Sensor Number	X-Coordinate (cm)	Y-Coordinate (cm)
1	0.59	1.00	16	1.90	4.46
2	-0.59	1.00	17	0.50	4.46
3	1.16	1.96	18	-0.50	4.46
4	0.00	1.96	19	-1.90	4.46
5	-1.16	1.96	20	-3.04	4.46
6	1.79	2.73	21	2.73	5.19
7	0.53	2.73	22	1.41	5.19
8	-0.53	2.73	23	0.00	5.19
9	-1.79	2.73	24	-1.41	5.19
10	2.37	3.64	25	-2.73	5.19
11	1.17	3.64	26	2.73	5.64
12	0.00	3.64	27	1.41	5.64
13	-1.17	3.64	28	0.00	5.64
14	-2.37	3.64	29	-1.41	5.64
15	3.04	4.46	30	-2.73	5.64

Table 6-1: Coordinates of Sensors as Measured From Coordinate Origin

The sensor array was mounted flush with the top wall of the inlet as shown in figure 6-8. The lead wires were bundled and strain relieved. Each lead was connected to a 5 meter BNC cable and connected to a CTA (56C17 DANTEC CTA). The 5-meter cable was necessary in order for the bridge to be correctly balanced, as an internal setting allowed the bridge to compensate for the impedance of a 5-meter cable. Other internal settings included the gain, which was set to 166 AC and 3470 DC, and filter settings, which were set to a bandwidth of 25 kHz with a frequency response shape set to 'Film.'

To ensure that the sensor array did not significantly impact the original flow characteristics of the inlet, its thickness was made to be much less than the thickness of the boundary layer at the leading edge of the sensor array. The thickness of the array was 114μm, a very conservative estimate of the boundary layer thickness at the leading edge of the array was calculated to be on the order of 2mm, for details see [20]. Thus the boundary layer thickness is about 17.5 times greater than the thickness of the array.

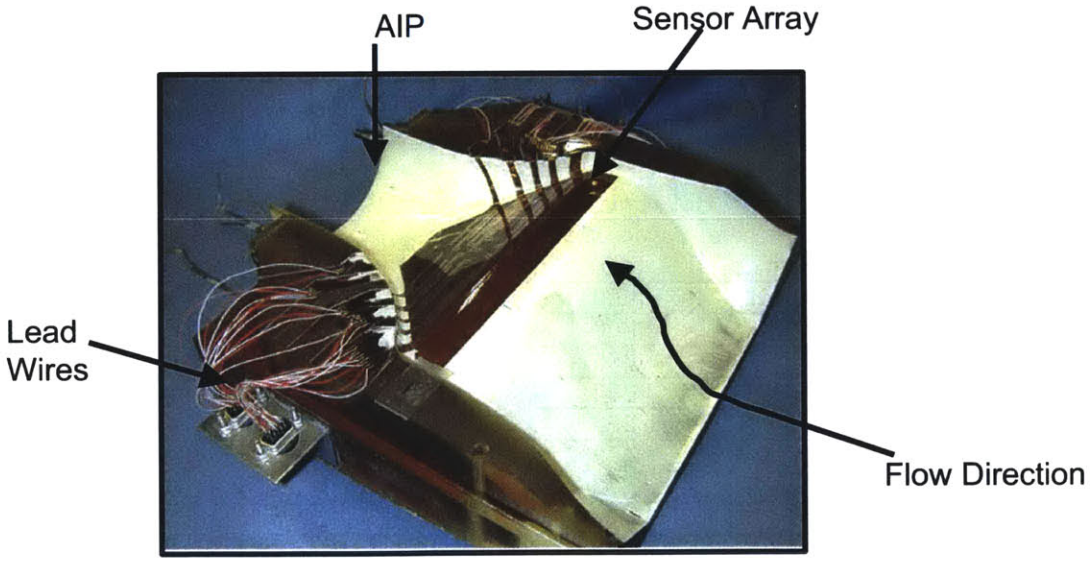

Figure 6-8: Hot-Film Sensor Array in Inlet (top wall shown upside-down)

6.3.4.2 Total pressure probes

The unsteady total pressure was measured at the AIP by way of three 5 psid Kulite pressure transducers. These probes were used to capture the unsteadiness at the AIP and serve as output in the development and verification of the filter. The frequency response of the pressure sensors was limited to a useful range of up to 1500 Hz by the presence of a half wave mode, resulting from the entrance tubing of the probe. However, for the purposes of these experiments this frequency range was sufficient. The pressure probes were mounted in a sensor ring designed by Warfield [18] (see figure 6-9), which allowed for the adjustment of probe location. The probes were placed in the regions of the AIP where Warfield showed the unsteadiness to be strongest in hopes of achieving the best correlation with the unsteadiness measured by the hot films in the separated. The coordinates of the probe locations are listed in table 6-2.

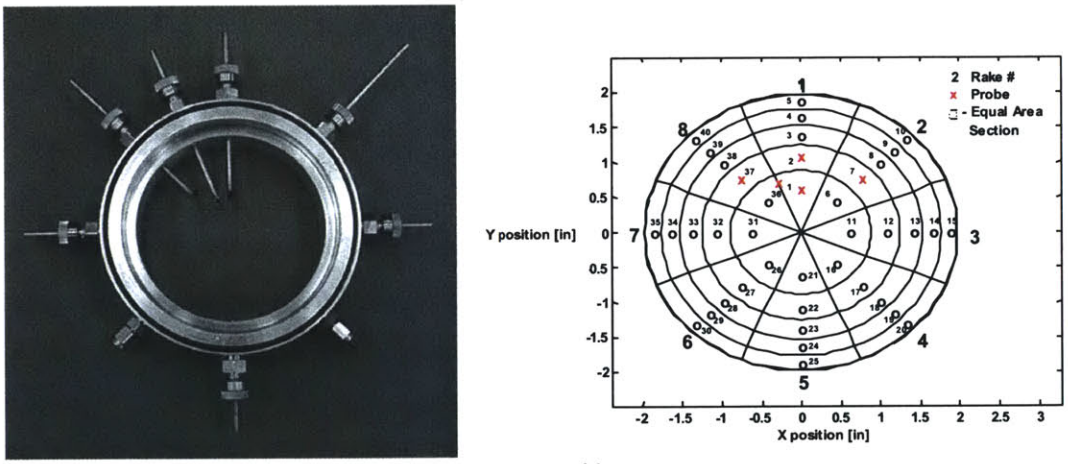

Figure 6-9: a) Sensor Ring, b) Profile of AIP (divided up by ARP 1420 guidelines) and Location of Total Pressure Probes

Total Pressure Probe Coordinates		
Probe Location (Fig 6-8)	Angle	Radius (inches)
1	0°	0.628
2	0°	1.096
7	45°	1.096
37	-45°	1.096
Between 1-37	-22.5°	0.770
Midpoint 2-37	-22.5°	1.013

Table 6-2: Unsteady Total Pressure Probe Coordinates (0° at top)

The CTAs and pressure transducers were connected to Measurements Group Inc. Model 2300 Strain Gauge Conditioning Amplifiers. These signal conditioners serve to AC couple and amplify the input voltages and they allow for adjustments in the bandwidth and gain. For the hot-films, the low pass cutoff was set at 10 kHz, the high pass cutoff was set at 1 Hz, and the gain was set at 10. The pressure transducers were operated with an excitation of 5 volts, the low pass cutoff and high pass cutoff were again 10 kHz and 1 Hz respectively, and the gain was set to 200.

6.3.5 Data Acquisition

Data was acquired simultaneously from the hot-films and total pressure probes through an ADTEX AD-380 12-bit analog to digital high-speed data acquisition system. The data acquisition system consisted of 4 boards with eight channels each and acquired data at a rate of 20 kHz. The buffer size was 32768 bytes with a buffer count of 200 per measurement, corresponding to 102,400 data points or 5.12 seconds per channel. The maximum signal input range was ± 5 Volts. DOS based software, developed and maintained by Dr. Gerald Guenette at the Gas Turbine Laboratory, MIT, was used to operate the system.

6.3.6 Overview of Experiments

Because of a limited number of CTA's, it was only possible to experiment with 18 hot-film sensors at a time. Data was therefore taken on two different days using two different sensor configurations, set 1 and set 2, as illustrated in figure 6-10. For each set, data was

collected at the AIP by way of three total pressure probes. The location of one of the three probes differed from set 1 to set 2 (see figure 6-10).

Before data could be collected, the CTA bridges had to be balanced and the sensor temperature (or overheat ratio) had to be set. A description of how this is done can be found in [20]. The highest possible overheat ratio was used that would not damage the sensor element in order to achieve the maximum sensitivity to the wall shear stress and to reduce the effects of temperature fluctuations in the freestream. Data was collected for a range of mass flows from 2.1 lb/s to 3.6 lb/s. Northrop-Grumman calculated the full-scale UCAV cruise condition to be simulated by a mass flow of 3.1 lb/s in the $1/6^{th}$ scale model, thus the mass flows tested cover a broad range centered around the cruise flight condition.

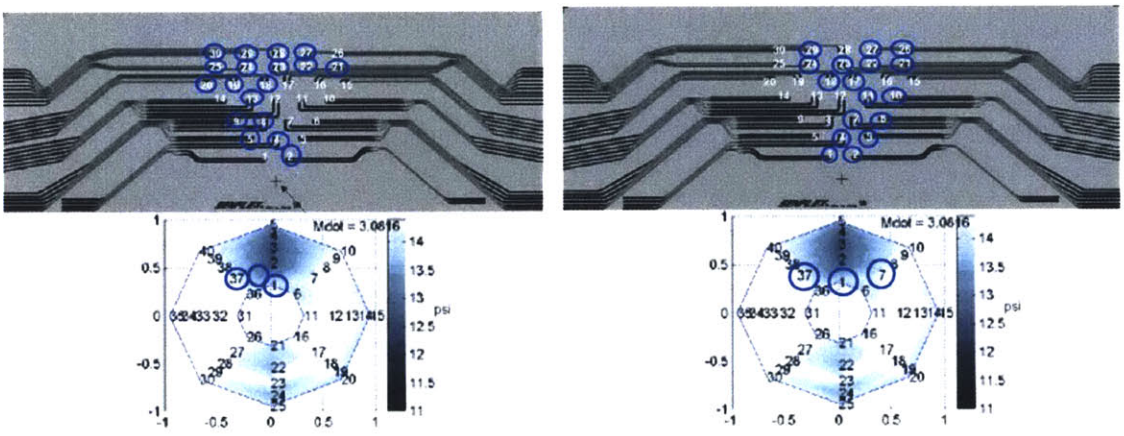

Figure 6-10: a) Hot-Film Sensors and Pressure Probes Used in Data Set 1, b) Hot-Film Sensors and Pressure Probes Used in Data Set 2

6.4 Details of Filter Construction

Using the data collected, the FIR Wiener filter, described at the beginning of this chapter, was constructed using MATLAB. A detailed description of the filter construction follows.

The hot film sensors were used as input signals and the total pressure probes served as the output data used to construct the filter. The filter was then applied to another set of hot film data (or in some cases, the first half of a data set was used in making the filter that was then applied to the second half) and this filtered data was correlated against the actual total pressure data from that same set to verify the ability of the filtered hot film data to predict the down stream conditions. Figure 6-11 shows an illustration of the filter construction and testing method. The commented MATLAB codes used to construct and test the filter can be found in appendix A.

To make the filter, a number of hot-film sensors were chosen (ranging from just one sensor up to using all 18 of the sensors contained in the data set). A single AIP total pressure probe was selected to serve as the output data. Because the signal and noise do not have distinct spectral characteristics, a "conditioned spectral analysis" was used to isolate and emphasize the coherent structures; a band pass filter cut off the high frequency noise and isolated the signal in the range of 600-900 Hz, the frequency shown to be the characteristic frequency of the vortex shedding [20].

The MATLAB command "filtfilt" was used to make this band pass filter. The filter was described by a vector called filter_vector. Filter_vector was created with "FIR2," an arbitrary shape filter design technique that uses the frequency sampling method. The resulting filter is a 251^{st} order FIR digital filter with a user specified frequency response.

A matrix was then constructed which consisted of the autocorrelations of the data from each hot-film sensor along the diagonal, and the cross correlations of each hot-film to the other hot-films to fill in the matrix. The MATLAB command "xcorr" computes the correlation over a specified number of lags. The number of lags chosen directly affects the computing time, as discussed above, and thus will likely need to be truncated at some point. Various numbers of lags were studied to examine the effect of this truncation for the present case and it was seen that truncating the number of lags to a level that would allow for computational times which would meet practical needs, caused little decrease in the filter's ability to predict the downstream signal. A matrix was also constructed by

computing the cross-correlations between each hot-film and the total pressure probe, using the same MATLAB command.

Thus the linear equation XB=Y was made, where X is the hot-film matrix, B is an array of weighting constants and Y is the array containing the cross-correlations of hot-films to the total pressure probe. The weighting constants are then found by inverting the hot-film matrix, $B=YX^{-1}$. These weighting constants are then used to construct the FIR filter.

The weighting constants, however, were passed through a Savitzky-Golay polynomial smoothing filter, or sgolay filter, of order 2, with a frame size of 7. Doing this was found to results in a better prediction of the downstream conditions in the time domain.

The newly made FIR Wiener filter was then applied to a second set of hot film data using the MATLAB command "filter," which implements the following equation,

$$y(n) = b(1)*x(n) + b(2)*x(n-1) + \ldots + b(nb+1)*x(n-nb) - y(n-1) - \ldots - y(0) \quad (6\text{-}18)$$

Lastly, the FIR filtered hot-film data was cross-correlated with the AIP total pressure data in order to verify its ability to predict the flow conditions at the AIP. Ideally they will agree very well, indicating that the hot-films will give an adequately accurate picture of the flow conditions at the AIP and can be used in a control loop to successfully control actuators.

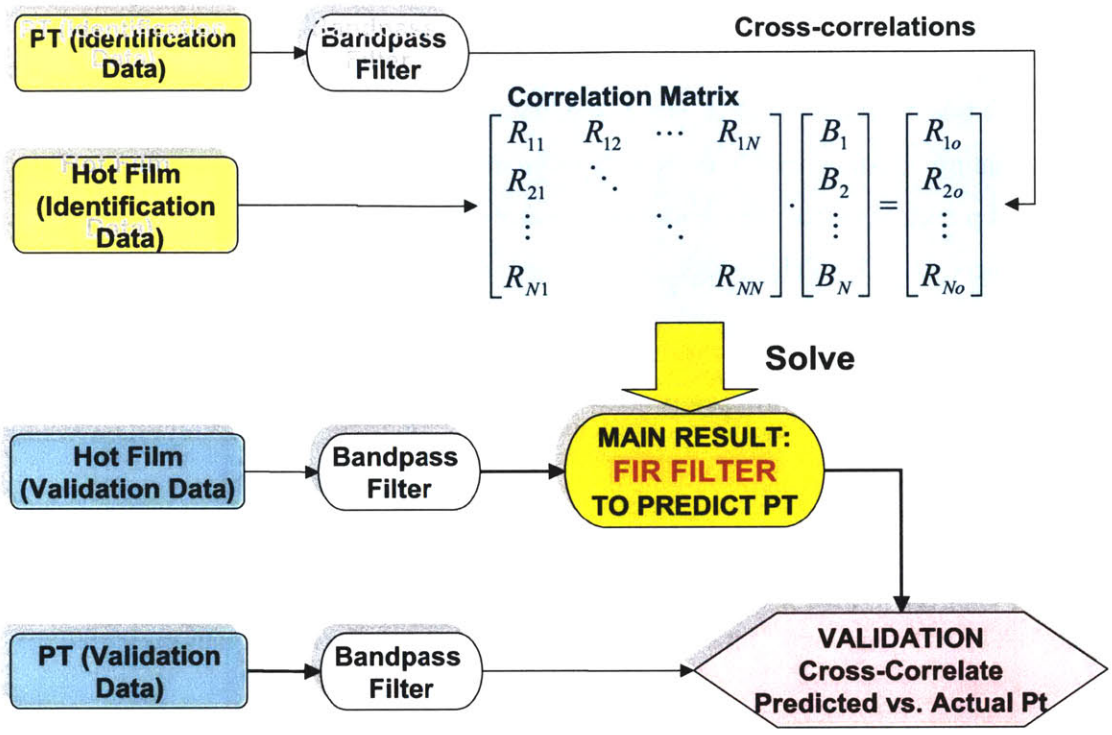

Figure 6-11: Illustration of Filter Construction and Validation

7 RESULTS

7.1 Overview

The filter was applied using various combinations of the 30 hot-film sensors and any one of the three unsteady total pressure probes. The results of this investigation are divided into three sections. The first section demonstrates the ability of the filter to predict downstream conditions at the AIP of the UCAV inlet. The second section shows the results of a study done to determine the best locations in which to place sensors in the full scale UCAV, and the ideal number of sensors to use. The final section shows the filter's ability to predict downstream flow characteristics over changing atmospheric conditions and inlet mass flows.

7.2 Application of Filter

To first determine the filtered hot-film data's effectiveness for predicting conditions at the AIP, the correlation between a single filtered hot film sensor (sensor 21) and a total pressure probe (probe location 7) was calculated. This was compared to the correlation between the same hot-film, without being filtered, and the same total pressure probe, see figure 7-1. In this case, the filter was made using the first half of the data set and was then applied to the second half of the data set. From the figure, it can be seen that filtering the hot-film results in a much greater peak correlation value. The unfiltered sensor had a peak correlation of 0.569, whereas, after filtering, the correlation improved to 0.836. It can also be seen that the phase of the filtered data has shifted. This difference in phase is consistent with the convection time of the flow from the hot-film to the AIP. Thus, the unfiltered data is delayed by the convection time of the flow and this shift represents the removal of the delay by the filter. Figure 7-2 shows the same filtered hot-film – total pressure probe correlation from Figure 7-1, this time plotted on top of the auto correlation of the total pressure probe. The auto-correlation represents the ideal signal that would result if the filter could produce a perfect prediction. As can be seen in figure 7-2, the character of the autocorrelation is predicted well by the filtered data.

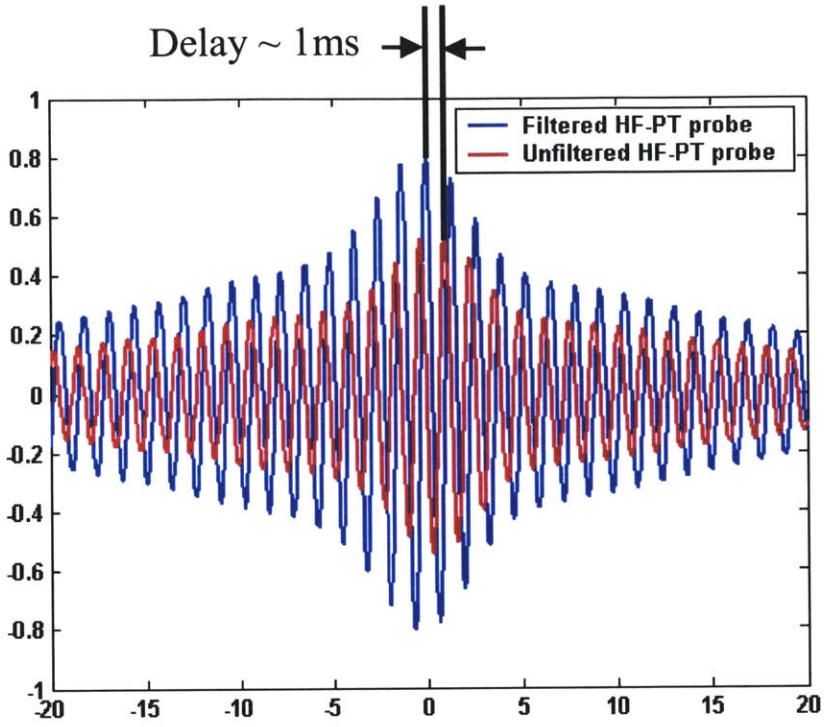

Figure 7-1: Correlation Between AIP Total Pressure Probe and Hot-Film Sensors Both With and Without Filtering. The Filter Has Removed the Time Delay and Improved the Correlation.

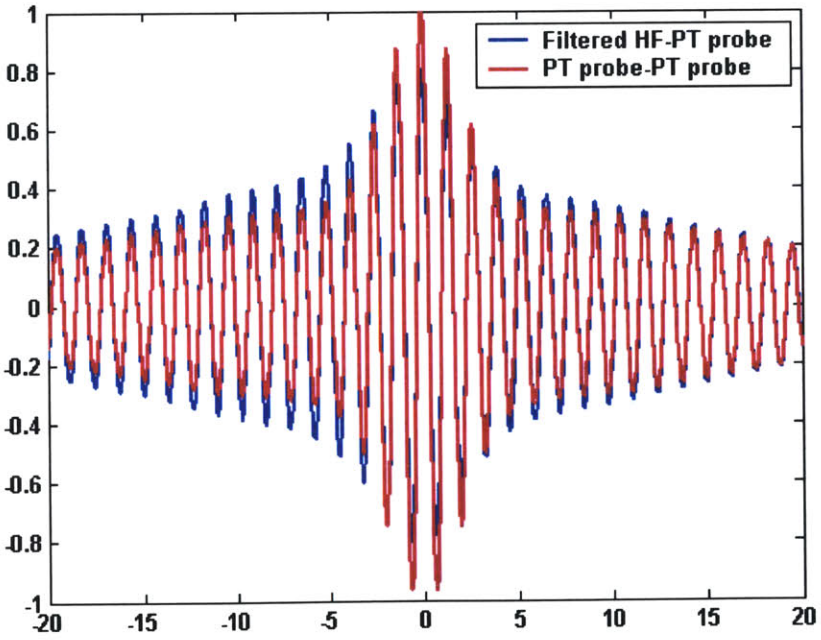

Figure 7-2: Correlation Between the AIP Total Pressure Probe and Filtered Hot-Film Sensors and the Autocorrelation of the AIP probe. The Autocorrelation Represents the Ideal Performance of the Filtered Hot-Film Sensor Data

Figure 7-3 shows a time trace of the filtered data (red) laid atop the actual total pressure data (blue), which it is trying to predict. As can be seen, the filtered data follows the total pressure data quite well. This gives a more deterministic illustration of the ability of the filtered hot film data to predict the downstream conditions, as opposed to a statistical representation, which is what the correlations provide.

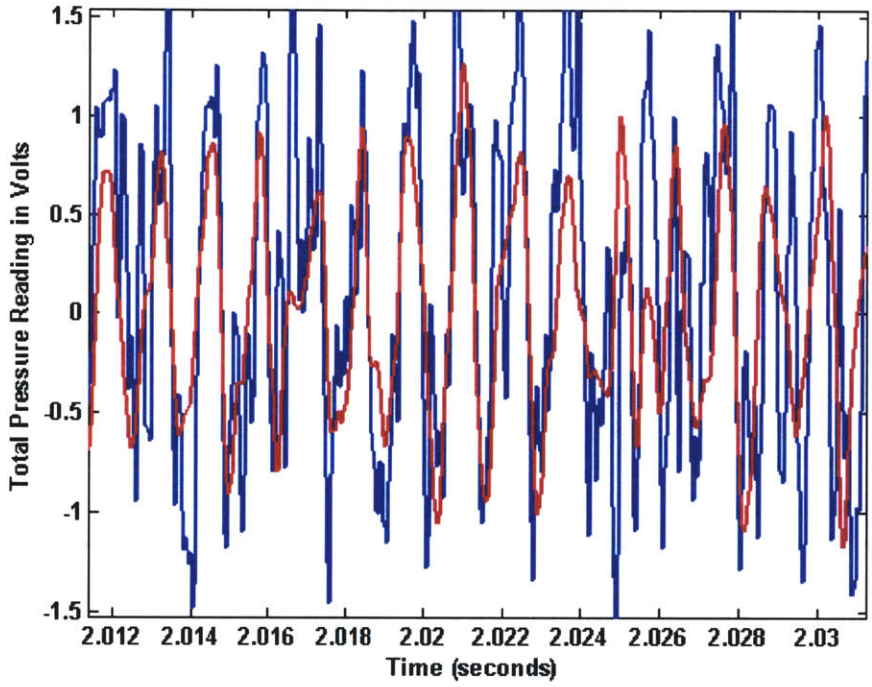

Figure 7-3: Filtered Data (red) Superimposed Upon Output Data Measured at the AIP (blue). In This Case Sgolay Smoothing Was Not Used.

Sgolay smoothing of the weighting constants was used to make Figures 7-1 and 7-2. This was because it was found that smoothing resulted in an increase in the correlation between the hot-film sensors and AIP total pressure probe. However, Figure 7-3 was made without sgolay smoothing. Figure 7-4 shows the same figure made using sgolay filtering. With the smoothing, the filtered data does not follow the actually output data as well. In particular, the amplitude of the data is cut off significantly by the smoothing.

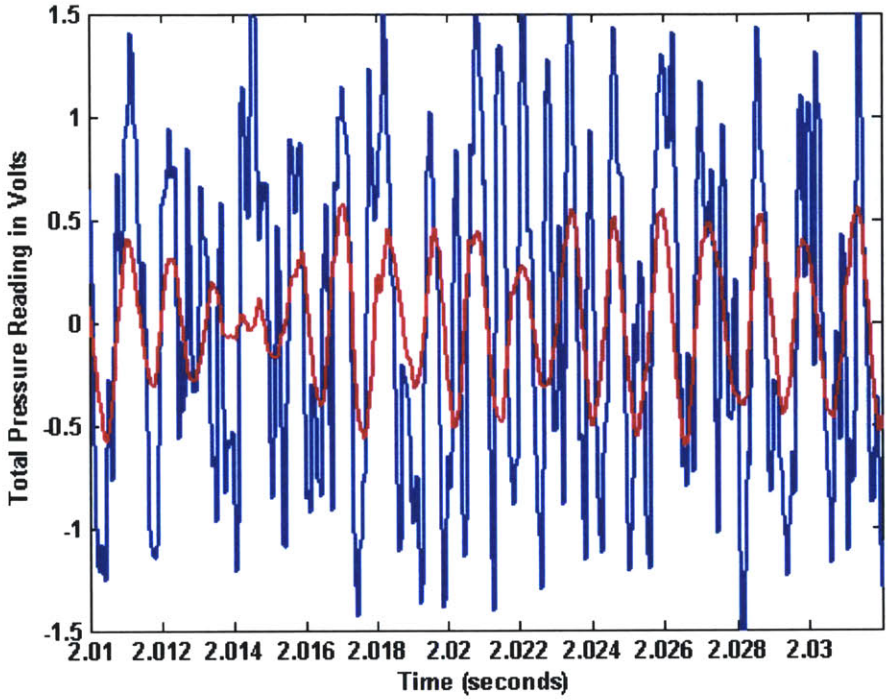

Figure 7-4: Filtered Data (red) Superimposed Upon Output Data Measured at the AIP (blue). In This Case Sgolay Smoothing of the Constants Was Used.

Using the procedure just outlined, each individual hot film sensor was filtered and correlated to an AIP pressure probe. For each hot film sensor, the first half of its data array, along with the first half of an AIP total pressure sensor data array, was used to produce a filter, which was then applied to the second half. Figure 7-5 is an interpolated surface plot, which shows the maximum values of each of these correlations. The +'s on the figure indicate the location of each of the sensors. Figure 7-5a shows the correlation of the hot film sensors against AIP location 7. Because position 7 was only used in data set 2, only half of the array can be shown. Figure 7-5b shows the data for all 30 sensors correlated with AIP position 1.

The individual correlations show a wide disparity in the ability of sensors to predict the down stream conditions. The most highly correlated sensor, when filtered, produced a maximum correlation with the AIP sensor of as high as 0.83, however, in other locations, as low as 0.1. The results of this indicate two striking facts; the first is that very high correlations can be achieved, and the second is that sensor placement is crucial.

a) b)

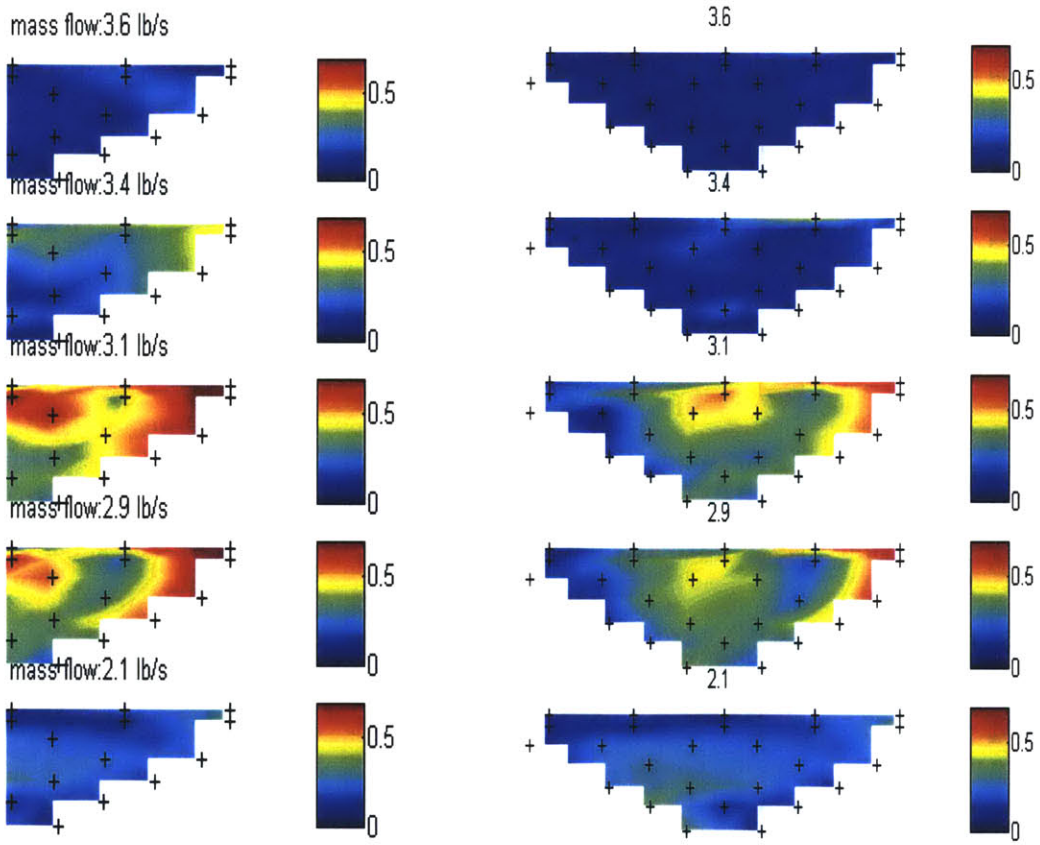

Figure 7-5: a) Interpolated Contour Plot of Maximum Correlation of Each Filtered Hot-Film Sensor from Data Set 2 to AIP Position 7 (see Figure 6-8), b) Maximum Correlation of Each Filtered Hot-Film Sensor from Both Data Sets to AIP Position 1

The type of filtering used here, however, can alleviate the necessity for very accurate sensor placement because it allows for the simultaneous use of multiple sensors as inputs. This ensures a greater likelihood of capturing information from the separated region that is highly correlated to the AIP. Using multiple sensors is also expected to improve the

overall maximum correlation value of the predicted signal to the actual AIP signal over any single input-output pair. The following section applies this concept.

7.3 Optimum Number and Location of hot film sensors

After determining that the filter does improve the correlation of upstream sensors to sensors at the AIP, a study was conducted to determine the ideal number of hot films to use for actual implementation purposes, and the optimal location of these sensors. There were three goals of this study. The first was to determine if adding additional sensors always improves correlation and by how much. The second was to determine if it is critical to have sensors in the very highly correlated region, or if using multiple sensors in locations of lower correlation can provide a sufficient result, thus allowing some forgiveness in sensor location. And the third was to try to map the sensors that provide high correlation to flow features using the flow visualization results of Warfield.

Figures 7-6 and 7-7 show how sensor correlation improves with the addition of input sensors until all 18 in the data set are used. The figures start with the most highly correlated input-output pair for each data set and add in subsequently inferior sensors until the sensor with the lowest individual correlation is added and all 18 are used.

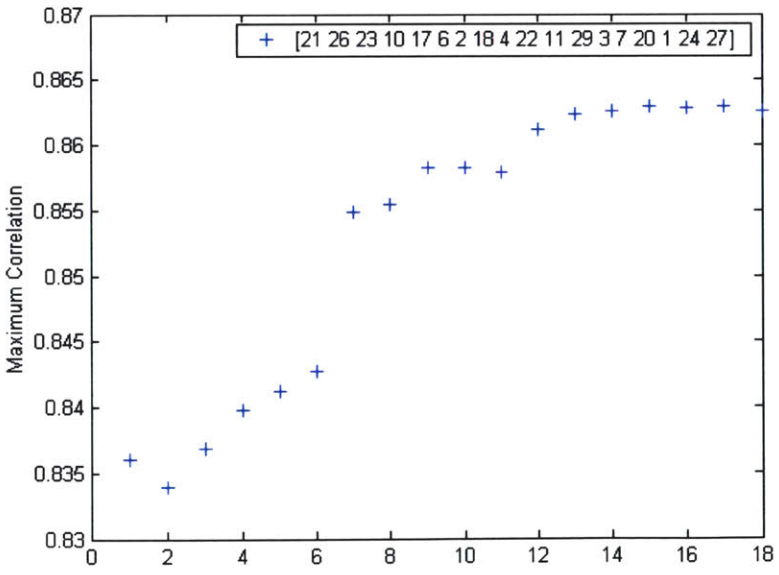

Hot Film Sensor	Max Ind Correlation
21	0.836
26	0.8035
23	0.7177
10	0.7082
17	0.6599
6	0.604
2	0.5682
18	0.5606
4	0.4833
22	0.471
11	0.4578
29	0.4016
3	0.3737
7	0.3487
20	0.2154
1	0.1523
24	0.1407
27	0.1001

Figure 7-6: Correlations to AIP Probe 7, Adding in Successively Inferior Hot-Films

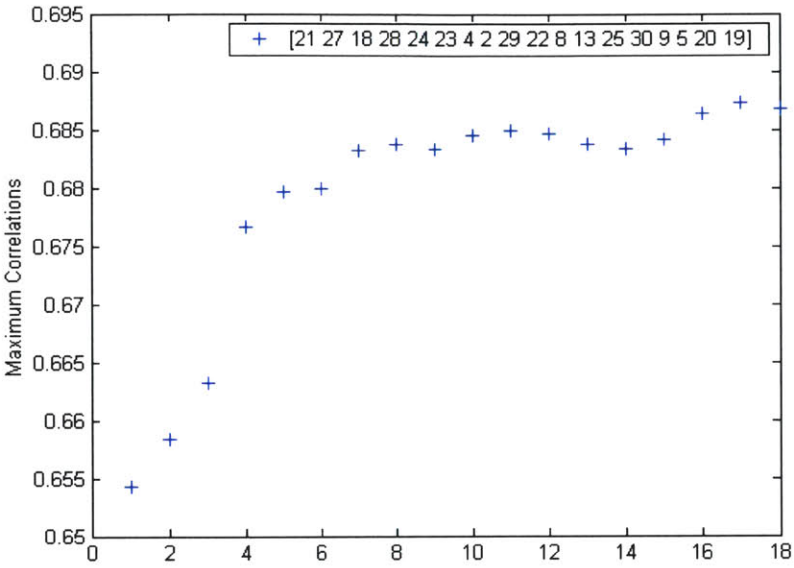

Hot Film Sensor	Max Ind Correlation
21	0.6543
27	0.5985
18	0.5115
28	0.4623
24	0.4328
23	0.4031
4	0.3809
2	0.3797
29	0.3663
22	0.3622
8	0.3237
13	0.2491
25	0.2153
30	0.1941
9	0.1909
5	0.1653
20	0.1387
19	0.1005

Figure 7-7: Correlations to AIP Probe 1, Adding in Successively Inferior Hot-Films

As can be seen from the figures, the correlation improves in an asymptotic way. In both cases, the greatest improvement in correlation is achieved with the first 6 or 7 sensors. For both configurations, the first 7 sensors capture 99% of the maximum correlation that is possible by using all 18 sensors. It can be concluded from these results that a few well-placed sensors are very nearly as effective as the entire array, and much more practical for real applications. Note that in both cases the correlation does not improve greatly over the most highly correlated individual sensor.

The previous figures (Figures 7-6 and 7-7) were made using the most highly correlated sensors first. In order to determine if several sensors with lower individual correlations can provide a sufficiently high correlation, the most highly correlated sensors were removed and the correlation was recomputed. In Figures 7-8 and 7-9 the best seven sensors from each data set were used. The top line in each graph shows the improvement in correlation from the addition of each sensor until all seven are used. In the next line the best sensor has been removed and the others are again added in, and so on.

As can be seen from the figures, the change in improvement in correlation from adding in additional sensors actually increases when the best sensors have been removed. These plots show that using multiple input sensors does indeed provide more flexibility in sensor placement, which is an important finding if this system is to be useful in a real application where perfect sensor placement is unlikely.

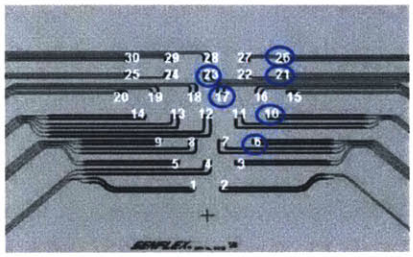

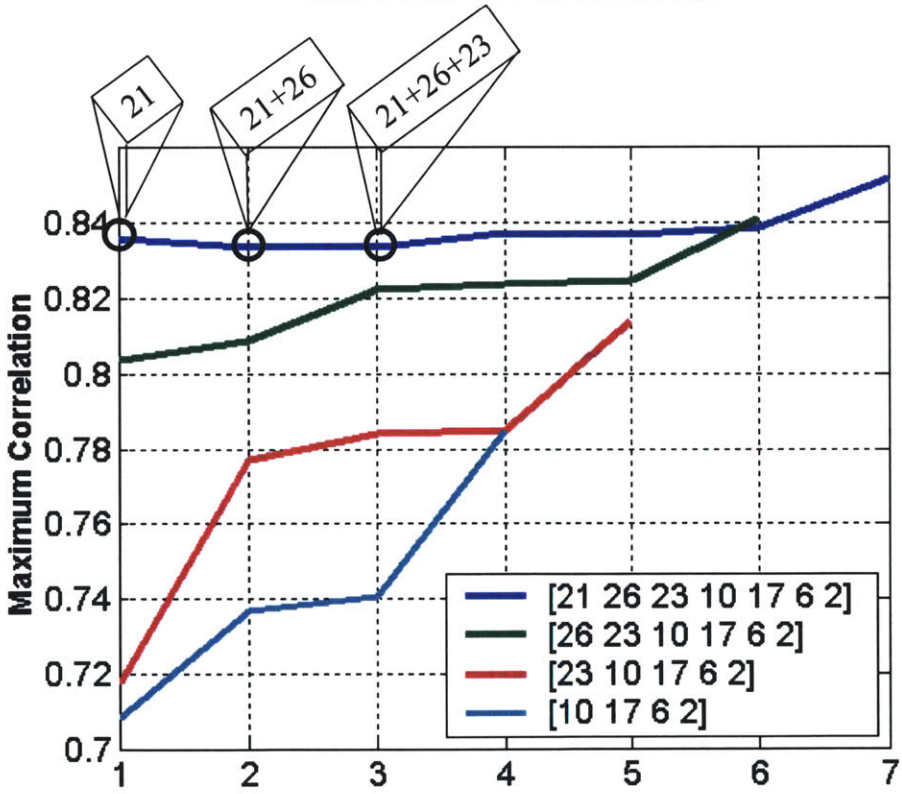

Hot Film Sensor	Max Ind Correlation
21	0.836
26	0.8035
23	0.7177
10	0.7082
17	0.6599
6	0.604
2	0.5682

Figure 7-8: Removing Best Sensor (Data Set 2 Correlated with AIP Probe 7)

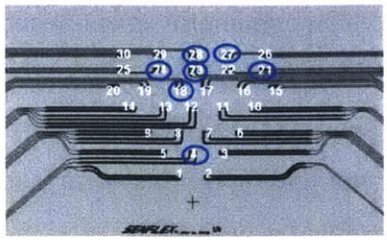

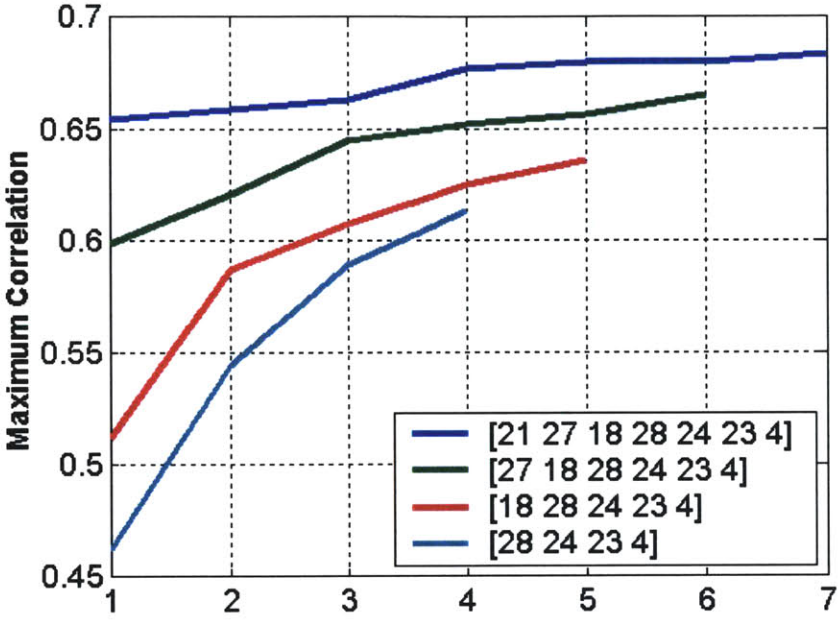

Hot Film Sensor	Max Ind Correlation
21	0.6543
27	0.5985
18	0.5115
28	0.4623
24	0.4328
23	0.4031
4	0.3809

Figure 7-9: Removing Best Sensor (Data Set 1 Correlated with AIP Probe 1)

The hot-film sensors that were found to be highly correlated with the AIP are overlaid on the flow visualization of the inlet, in figure 7-10, in attempt to identify the flow features that are highly correlated to the AIP. The dots on the figure indicate the locations of the sensors that had the highest individual correlations over a range of inlet mass flows. The blue dots represent those sensors that were used in both data sets and were found to be highly correlated in both data sets. The yellow dots were sensors that were found to be highly correlated but were only in one data set or the other. The red dots correspond to sensors that were included in both data sets but were found to be highly correlated in one data set but less so in the other data set.

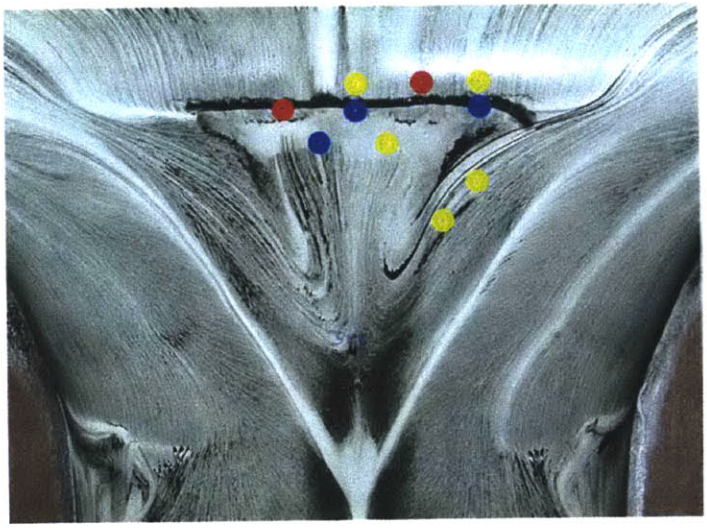

Figure 7-10: Most Highly Correlated Hot-Film Sensors Superimposed on Flow Visualization of Separation

The figure shows that the stagnation line is most likely the location of highest correlation. However, the upper middle of the separated region, just downstream of the separation line, and the outside edges of the separation also show signs of being locations of high correlation. Given the complex flow path of this inlet and the inherent non-linearities, it is unclear how directly these results could be transferred to a different inlet. However because the geometry and flow conditions of this inlet are nearly identical to what they would be in the full-scale UCAV (except for the Reynolds number) it is likely that the full-scale inlet would exhibit similar characteristics.

7.4 Filter Performance Over Varying Conditions

The filter was tested over varying mass flows and atmospheric conditions to determine if it could provide the robustness that would be required in an actual UCAV inlet. Table 7-1 is a matrix in which the filter is made from data from one of the two sets at a particular mass flow. That filter is then used to filter data from a different mass flow or data set and the maximum correlation is recorded in the table. In order to make the matrix the selection of hot-films and the total pressure probe was limited to those that were included in both data sets. Thus in this table, hot-films 21, 23, and 18 and the total pressure probe at AIP location 1 were used.

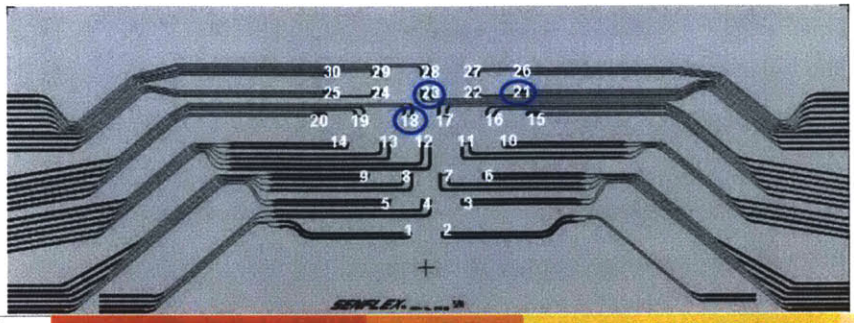

Filter\Data	Set 1: 3.1lb/s(1)	Set 1: 3.1lb/s(2)	Set 1: 2.9lb/s	Set 2: 3.1lb/s(1)	Set 2: 3.1lb/s(2)	Set 2: 2.9lb/s
Set 1: 3.1lb/s(1)	0.6152	0.6831	0.6567	0.4637	0.4661	0.479
Set 1: 3.1lb/s(2)	0.6119	0.6835	0.6564	0.4608	0.468	0.4791
Set 1: 2.9lb/s	0.6183	0.6847	0.6667	0.4636	0.4683	0.4795
Set 2: 3.1lb/s(1)	0.4265	0.4901	0.479	0.6582	0.6568	0.6731
Set 2: 3.1lb/s(2)	0.4331	0.4913	0.4837	0.66	0.6626	0.6686
Set 2:						8

Table 7-1: Maximum Correlations Over Changing Conditions

The table shows that the filter is still capable of achieving a good correlation to the AIP over varying conditions. It would be desirable if these values were higher; however, if more sensors had been included in both data sets the correlations could be improved. The important conclusion is that the trends do not change drastically with changing conditions indicating that it is likely that this method could be optimized and implemented.

The filter was also tested over a very broad range of mass flows (2.1 – 3.7 lb/s), to see if the characteristics of the flow change over different mass flows and thus the potential for this method of control to work over varying mass flows. Figures 7-11 through 7-13 show the change in correlation vs. change in inlet mass flow. All 18 sensors were used to make the filter in figure 7-11, and the filtered data was correlated against AIP probes 1 and 7. The best seven sensors were again used for figures 7-12 and 7-13. In this case, the filter was recomputed for each mass flow.

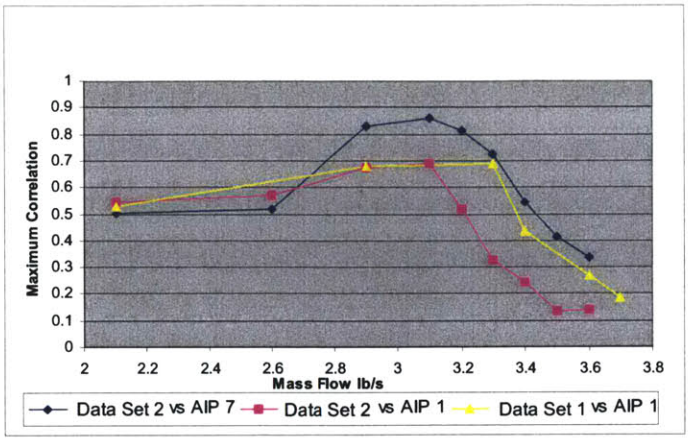

Figure 7-11: Maximum Correlations Over Changing Inlet Mass Flows Using All 18 Sensors From Each Data Set To Make The Filter

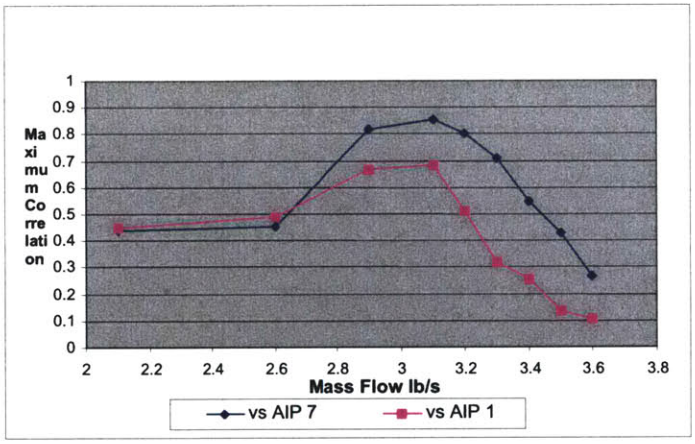

Figure 7-12: Maximum Correlations Over Changing Inlet Mass Flows Using The 7 Best Sensors From Data Set 2 To Make The Filter

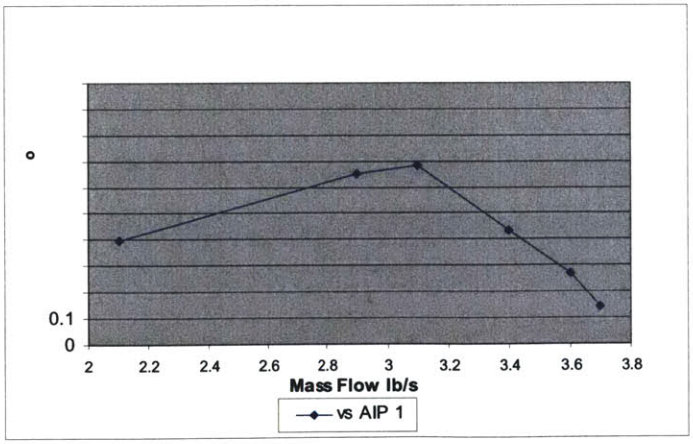

Figure 7-13: Maximum Correlations Over Changing Inlet Mass Flows Using The 7 Best Sensors From Data Set 1 To Make The Filter

The figures show that the hot film sensors are most highly correlated with the AIP in a mass flow range near cruise conditions and that the correlation trails off for high and low mass flows. The reason for this is likely due to the fact that at low mass flows the separation is much less severe and thus the large-scale structures in the flow, that were captured by the hot films at higher mass flows, are either small or no longer present. The reason for the decreased correlation at high mass flow is not as clear but it is likely due to the flow transitioning to a jet flow and thus altering the characteristics of the flow. However it is interesting, and fortunate, that the sensors produce a high correlation for a fairly broad range of mass flows centered at the cruise condition of 3.1 lb/s. It can again be seen from the figures that the best seven sensors perform very nearly as well as all 18.

SECTION 3 – PERIODIC SEPARATION POINT INJECTION

8 EXPERIMENTAL SETUP

8.1 Overview

In this chapter the experimental setup for periodic separation point injection in a high subsonic 3D separating inlet is described. The objectives of these experiments were to study the ability of periodic injection to improve pressure recovery and reduce distortion at the AIP of a real inlet with realistic Mach numbers. The effects of $C_{\mu steady}$, injection position, injection angle and injection frequency were examined in a parametric study.

The experimental test setup was similar to that described in chapter 6. It consisted of the same $1/6^{th}$ scale UCAV inlet, bellmouth, De Laval air compressor, and mass flow throttle plug. Additionally, the setup consisted of an actuation system, which was used to introduce pulsed injection near the flow separation point of the inlet and a data acquisition system that allowed for the measurement of steady total pressure at the AIP and static pressure at various points in the inlet.

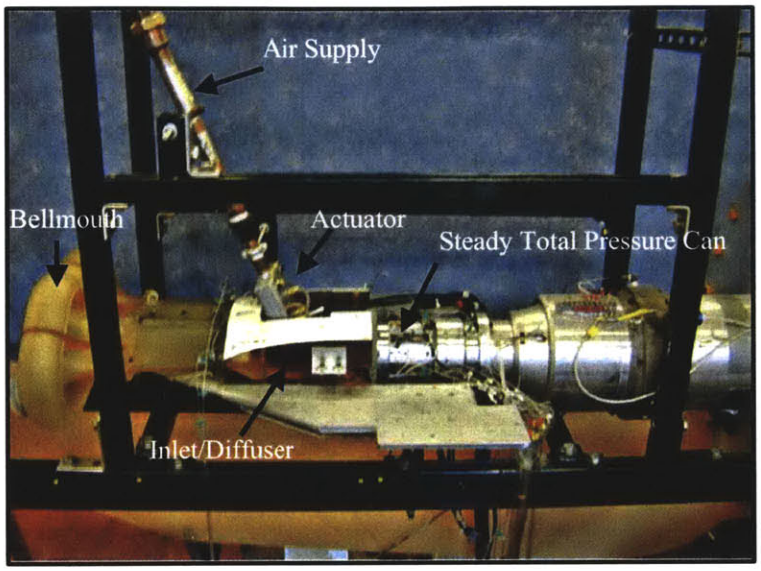

Figure 8-1: Experimental Setup

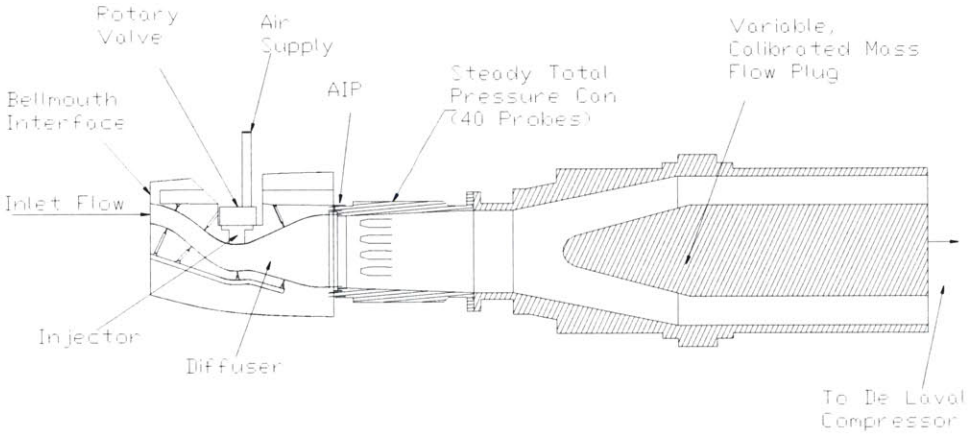

Figure 8-2: Schematic of Experimental Setup

8.2 Actuation

The actuation system used for these experiments consisted of a rotary valve, capable of frequencies of over 2.5 kHz, a 100psi compressor, and various injectors through which the air was ultimately passed into the diffuser. A pressure regulator and flow meter with thermocouple were used to calculate the injection mass flow (see appendix D).

8.2.1 Injector Blocks

Eight different interchangeable Coanda injector blocks were designed and tested. The injectors, which sit flush with the inlet's inner surface, are designed to introduce flow into the inlet near the point of flow separation. The injectors take advantage of the Coanda effect, which says that fluid flow from a nozzle will tend to follow a nearby curved surface if the curvature of that surface is not too sharp. When inserted into the inlet, each injector block is centered at the point of flow separation. High-velocity air is introduced through the injector block, and thus into the inlet, by way of a long narrow slot that runs through the block. This creates a 'wall-jet' at the separation point in the inlet. As described in chapter five, flow separation occurs in this inlet at the point of greatest curvature of the inlet wall. The wall jet introduces flow right at this point of curvature and, due to the coanda effect, the flow 'sticks' to the wall of the inlet in the separated region.

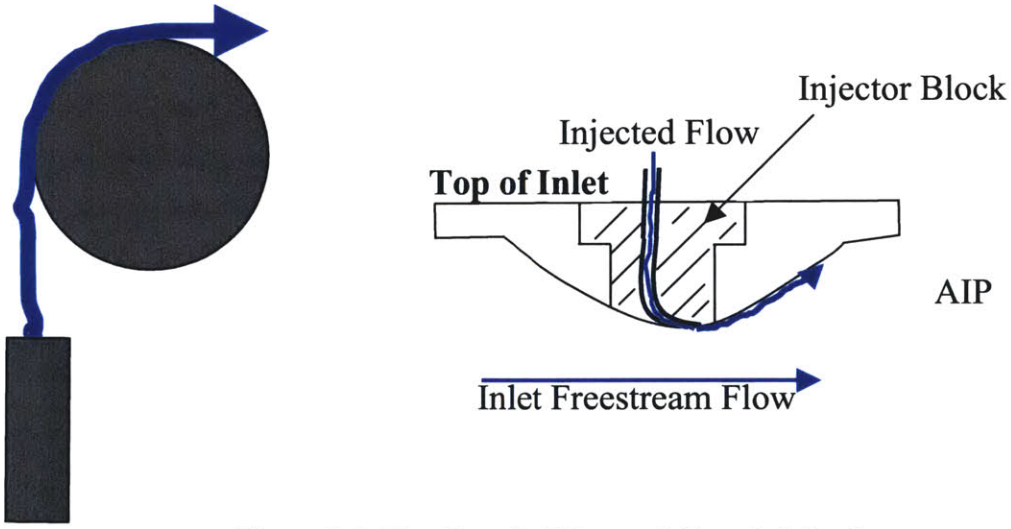

Figure 8-3: The Coanda Effect and Coanda Injection

This jet has three possible effects on the flow. If the injection occurs upstream of the flow separation, it can serve to energize the boundary layer and prevent the separation. In addition, the high velocity flow creates a lower static pressure region that serves to entrain flow from the freestream and thus can possibly 'reattach' the flow. Finally, pulsation of the injection can change the size of the shed vortex structures. Without actuation, these vortices naturally form and grow and, when they have grown to a certain

size, detach and convect downstream. Periodic injection can cause these vortices to detach more frequently, meaning that the shed vortices will be smaller with actuation than they would naturally be. In this case, the shedding frequency becomes phase-locked with the actuation frequency. It has been shown that these smaller vortex structures tend to follow the flow surface rather than convect directly downstream. This dynamic forcing effect is explained by Wygnanski and demonstrated by McCormick [1], [3].

The injector blocks were designed using Pro-Engineer and were fabricated using the same SLA method used to make the inlet. The injectors were designed as two separate pieces, which are bolted together (see figure 8-5). They each consist of a large constant-area duct that converges and curves to become tangential to the inlet flow surface. The large area duct helps to prevent losses through the injector. The flow accelerates as it passes through the converging neck until it reaches the exit which is the plane of smallest area, and thus of maximum flow velocity, in the injector. For details see [21].

Designing the injectors as removable blocks allowed for versatility in injector geometry and injector exit location relative to the separation line. The position and width of the exit slot differed among the eight injector blocks and some were also designed to inject flow at various angles. The angled slots consisted of a symmetric arrangement of two slots canted away from each other in a 'Chevron' configuration (see Figure 9-6). Slot angle is referenced to the spanwise direction, e.g. a slot angle of zero is perpendicular to the free stream. All slots were a total of 4 inches long.

a)

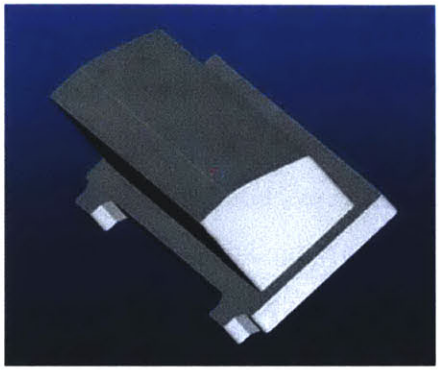

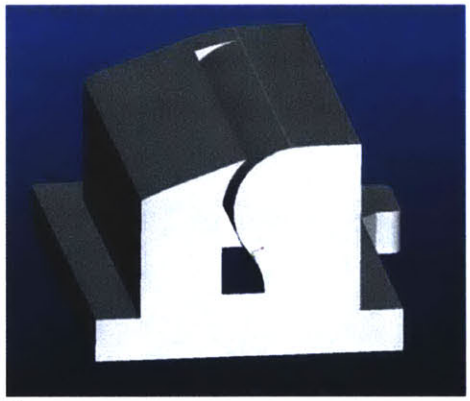

b)

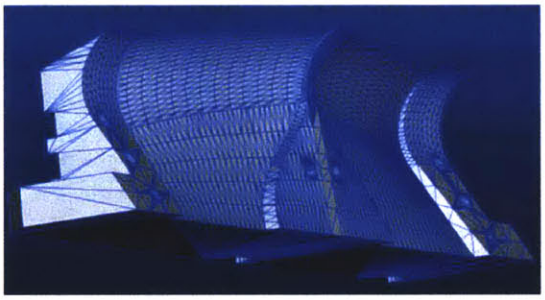

c)

Figure 8-4: a) 3D Rendering of an Injector Block, b) Cutaway Showing Flow Path Through Injector Block, c) One Half of an Injector Block

The following table describes each of the eight injectors. Pictures of each can be found in appendix C.

Injector	Slot Width (h)	Slot Position	Slot Angle
One	0.032"	@ Separation Line	0
Two	0.02"	@ Separation Line	0
Three	0.01"	@ Separation Line	0
Four	0.01"	0.19δ Upstream of Separation	0
Five	0.01"	0.58δ Upstream of Separation	0
Six	0.01"	0.19δ Upstream of Separation	6°
Seven	0.01"	0.19δ Upstream of Separation	12°
Eight	0.015"	0.39δ Upstream of Separation	0

Table 8-1: Description of Injector Blocks

The injector blocks were designed so that each of three parameters, $C_{\mu steady}$, injection position relative to the separation point, and injection angle, could be studied while holding the other two parameters constant. Thus injectors One, Two, and Three were designed to study the effects of changing $C_{\mu steady}$ while holding slot position and angle constant (see section9.3). Injectors Three, Four, and Five were designed to study the effects of injecting at positions at and behind the separation line while holding $C_{\mu steady}$ and angle constant (see section 9.4). Injectors Five, Six and Seven were designed to study the effects of injecting at an angle, relative to the inlet free stream flow, while holding slot position and $C_{\mu steady}$ constant (see section 9.5). Finally injector Eight was designed in attempt to take advantage of the lessons learned from the parametric study (see section 9.6). Note that injection was only introduced on the top side of the inlet where the separation was most severe.

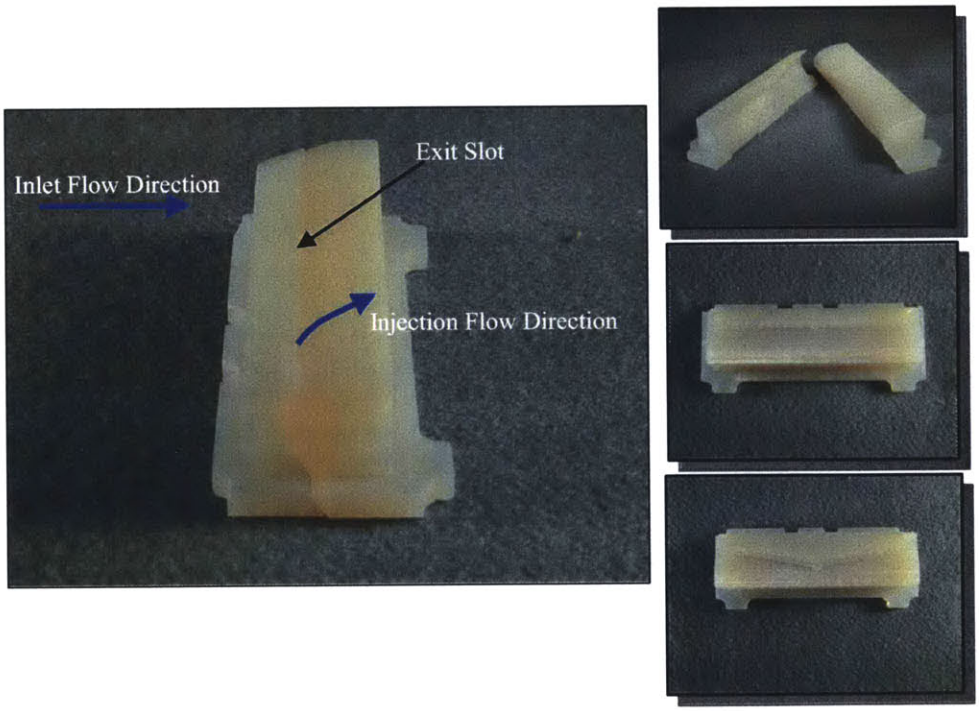

Figure 8-5: Injector Blocks

8.2.2 Rotary Valve

The actuator used in these studies to provide periodic mass flow for separation point injection, was a rotary valve designed by McElwain and built at the Gas Turbine Lab,

MIT [21]. The rotor sits in a body as shown in Figure 8-6. Air is supplied to the body by way of a 100 psi oil-free compressor. Air is transferred up through the middle of the rotor as it spins inside the body. The rotor has 10 holes; as it spins, a hole of the rotary valve is alternately aligned and misaligned with an exit slot in the body. When a hole in the rotor is aligned with the body slot, flow passes through and when no hole is aligned the flow does not pass through. The actuator sits on, and seals to, the injector. When the valve is 'open,' 100% of the flow that is put through the rotary valve passes into the inlet, however, when it is 'off,' though theoretically no flow should pass, because of some leakage due to non-zero clearances, some flow does pass into the inlet.

The rotor was driven by an AstroFlight Model 640 cobalt-40 motor. The rotational speed of the rotor sets the actuation frequency. The rotor was tested up to 15,000 RPM, which produces a actuation frequency of 2,500 Hz. To measure the actuation frequency, an inductor was placed near a 16-tooth gear in the motor and was connected to an oscilloscope. This provided a measure of the motor speed and thus the actuation frequency.

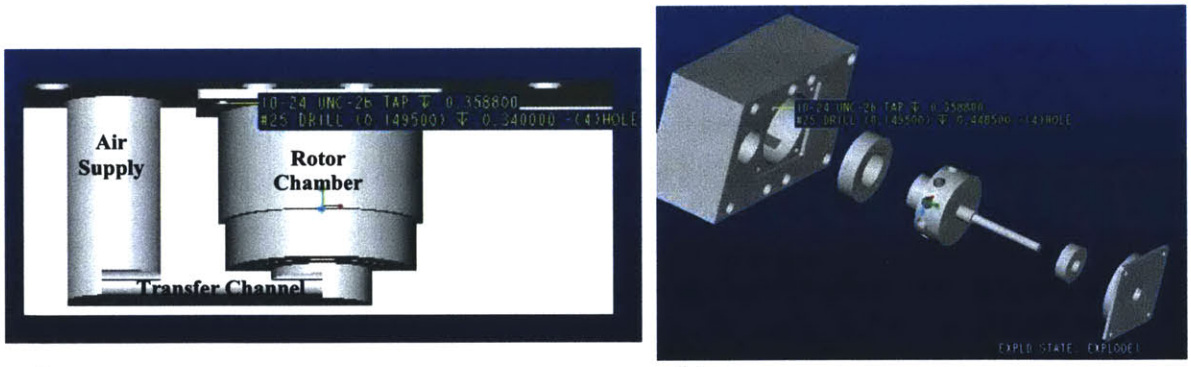

a) b)

Figure 8-6: a) Rotary Valve Body, b) Exploded View Showing Valve Body, Lower Bearing, Rotor, Upper Bearing and Cover Plate

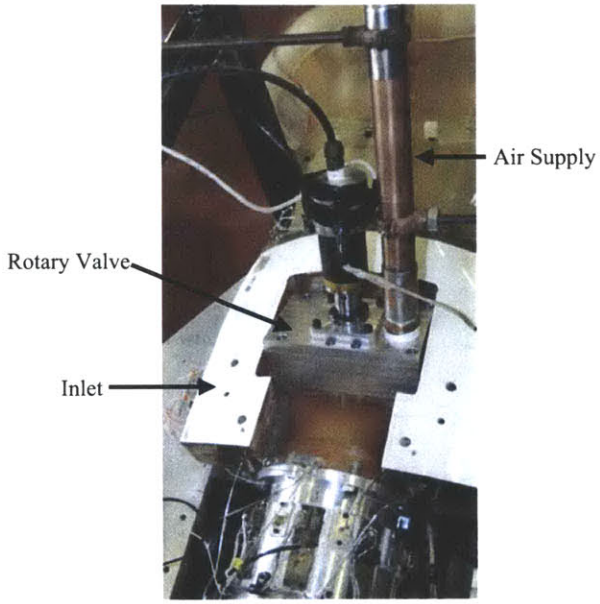

Figure 8-7: Top View of Inlet with Mounted Rotary Valve

8.2.3 Actuation Modifications

The rotary valve was later modified by adding an inner sleeve, reducing the clearance area between the spinning rotor and the body, and by changing the shape of the ten holes from round to square. These changes were made in attempt to reduce leakage and improve the duty cycle. Section 9.7 gives the results of implementing these changes. Another actuator was also designed and tested. This actuator uses a fluidic air diverter to create a pulsed flow. The diverter has no moving parts and relies on pressure differentials in order to create periodicity. Details of the design and testing of this actuator can be found in chapter 10.

8.3 Instrumentation

Steady-state total pressure profiles of the AIP were obtained from a total pressure can with 40 probes, each placed in the centroid of 40 equal area locations covering the AIP. This configuration is in compliance with ARP 1420 guidelines for measuring total pressure in a gas turbine inlet (Figure 8-9) [64]. From these profiles the pressure recovery and distortion could be computed. The can was rotated 22.5 degrees during some of the tests so that 80 points of data were taken, providing a finer resolution of the AIP. The probe locations are plotted in Figure 8-9.

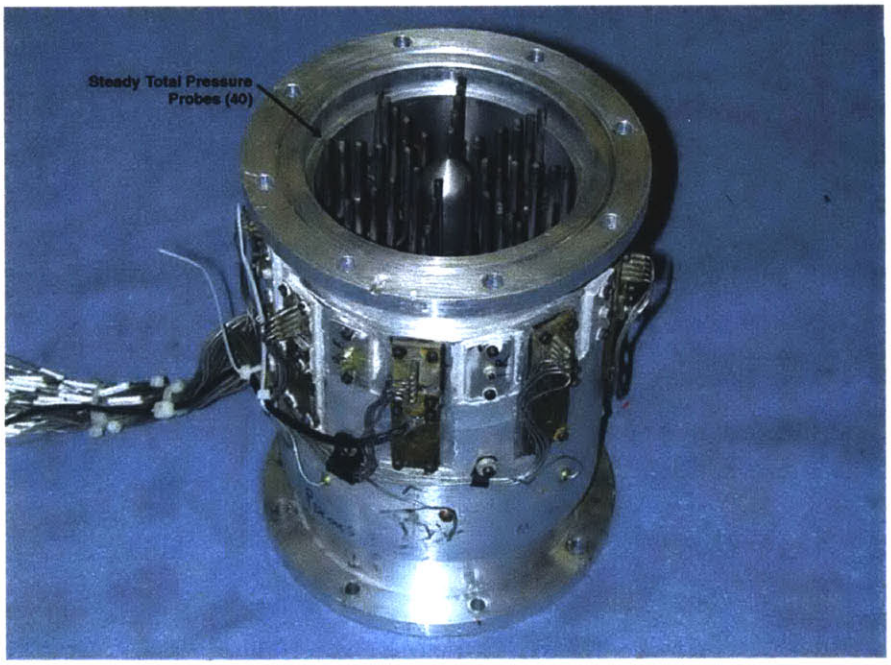

Figure 8-8: Steady Total Pressure Can

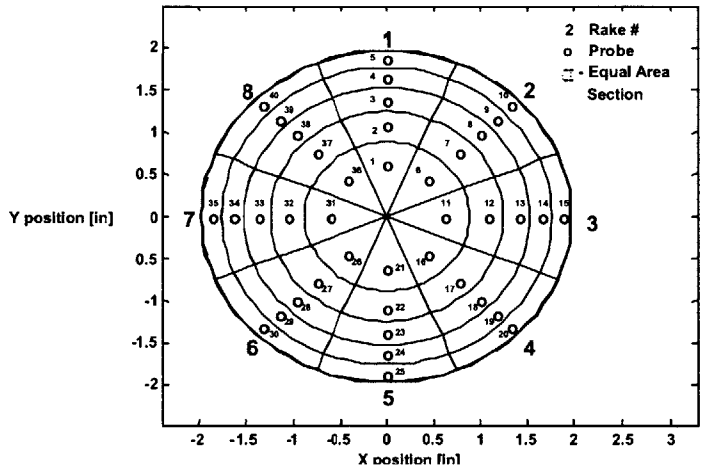

Figure 8-9: Probe Locations in Steady Total Pressure Can

In addition to the total pressure probes at the AIP, 24 wall static pressure taps were placed around the entrance of the inlet, around the AIP, and along the top and bottom surfaces of the inlet.

The static taps and the total pressure probes were connected via flexible tubing to a 48-port Scani-valve (Scanco No.sss 48CMK3) and a 16-port Scani-valve (Model DSA 3217/16Px). The Scani-valves both house a 100 psid pressure transducer, and both incrementally step through each port, measuring the pressure as they go.

8.4 Data Acquisition

8.4.1 Hardware

The 48-port Scani-valve was connected to a Scan-valve Digital Interface Unit (SDIU) (Model No. SDIU MK5), which controlled the Scani-valve and collected the output analog signal from the transducer and converted it to a digital signal. An executable program running on a PC, connected by way of a RS-232 connection, remotely controlled the SDIU. In order for the SDIU to properly interface with the host, several internal switches had to be configured to match settings in the PC. The internal settings used in these studies are shown in Table 8-2. The 16-port Scani-valve was fully autonomous and

was also controlled remotely by a PC connected to the Scani-valve through a 10/100baseT connection.

SDIU/Host Configurations	
Baud	9600
Parity	None
Data Bits	8
Stop Bits	1
Hardware Handshaking	Disabled

Table 8-2: SDIU/Host Configurations

The 48-port Scani-valve was calibrated before testing. The A/D converter was configured to ±5 volts by way of the correct configuration of dipswitches and jumpers. This means that a reading of a positive pressure of 100 psi would be reported as +5 volts and –100 psi would read –5 volts. A built in signal conditioner amplified the signal and was used to calibrate the output to ensure that the proper voltage output corresponded to a given pressure input. The 16-port Scani-valve has its own internal acquisition system and automatically calibrated itself and set the gain upon startup.

8.4.2 Software

The programs used to control the SDIU and the 16-port Scani-valve were Virtual Instruments (VIs) created using National Instrument's LabView software. The SDIU and 16-port Scani-valve came equipped with a set of built in commands; these were incorporated into the VIs in order to create routines for data acquisition. The VIs set the rate at which the transducer would cycle through all of the ports, the number of readings they would take at each port, and wrote the data to a file.

The long length of the tubes connecting the pressure probes and taps to the Scani-valves resulted in lag times between the actual pressure in the inlet and the pressure observed by the pressure transducers. This settling time was accounted for by simply allowing sufficient time in between physical adjustments to the experiment and data collection.

8.5 Bench-Top Experimental Setup

Bench top tests were conducted to characterize the flow through the injectors before they were placed in the diffuser and in order to calculate the momentum of the flow from the injectors, for various mass flows, to be used to calculate Cμ, the ratio of injection momentum to free stream momentum. The same actuation system and injectors that were used for the diffuser tests were used for the bench tests. Additionally, the bench tests consisted of a flow separator bump with geometry similar to the diffuser, and an unsteady total pressure data acquisition system. The actuation system was fastened to the table. An injector block was inserted into the flow separator bump and both were bolted to the actuator (see Figure 8-10).

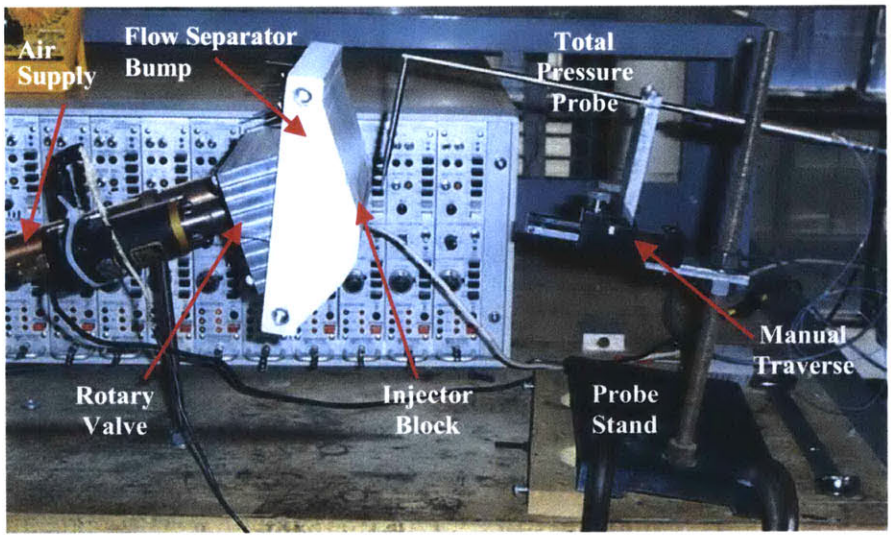

Figure 8-10: Bench-Top Experimental Setup

8.4.1 Unsteady Probe

Unsteady total pressure data was taken with a 15-psig Kulite pressure transducer (Model VCS-062-15G) inside of a probe designed by McElwain [21]. The signal was amplified by a Vishay Measurements Group model 2310 signal-conditioning amplifier. The probe was mounted on a traverse that allowed for data collection along the span of the injector exit, ensuring spatial uniformity. The natural frequency of this probe was found to be 5

kHz, far above the range of frequencies of interest to this research, thus ensuring it would not interfere with the test data.

The nose cone of the probe was later modified in order to make it small enough to be used for Injector Two, which had an exit slot width of 0.02 inches. The natural frequency of the probe after this modification was still found to be sufficiently high and did not interfere with the range of frequencies used in the tests of this research. However, it was not possible to further modify the probe to make it useful for injectors with smaller than 0.02-inch exit slot widths.

8.5.2 Acquisition

Data was collected using a National Instruments PCI-6071E analog-to digital data acquisition board with 32 differential channels, and with a maximum sample rate of 1.25 megasamples per second over all channels. A VI was again created for data acquisition. The VI set the data-sampling rate (in this case it was set to 20 kHz) and commanded the card to acquire a number of samples from specific channels.

8.5.3 Calibration

Before each use, the unsteady pressure transducer had to be calibrated. To do this, the transducer was connected to an amplifier/signal conditioner. The gain on the conditioner was set to 100, the high and low pass values were set to 10 kHz and 1 Hz respectively, and AC coupling was disabled. The amplifier excitation was then turned on. With no pressure applied to the transducer other than atmospheric pressure, the signal conditioner was zeroed using an auto-balance switch on the front panel. The probe was then over-pressured 2 psi above atmospheric. A voltmeter, which was connected to the signal conditioner, reported the voltage output given by the signal conditioner. The amplifier gain was then adjusted until the voltage read 1 volt. Thus for every psi of pressure to the transducer, an output signal of 0.5 volts was given. This was done because the signal conditioner had a ± 10 volt maximum output and a one-to-one volt to pressure ratio would have exceeded this maximum for some test cases.

9 RESULTS

In this chapter a study is described in which periodic separation point injection was used to reduce the steady effects of flow separation in the UCAV inlet. The work of McElwain [21] was furthered by performing a parametric study of the effects of C_μ, injection position, injection angle and forcing frequency. The ultimate goal of this study was to find the optimal value of these parameters within this inlet, where the metrics for improvement are Pressure Recovery and distortion at the AIP.

9.1 First Attempt

The first injector block tested, injector One, had an injection slot that was located right at the point of flow separation [21]. The slot was 0.032 inches wide, 4.0 inches long, and injected flow parallel to the free stream flow direction. Pulsed air was introduced through the injector at a frequency of 2 kHz. This frequency was found to yield the best results for a broad range of geometric conditions, so it was not varied during the parametric study. Injection mass flows ranging from 0.5% to 4% of the inlet mass flow were tested for their effect on pressure recovery at the AIP. The inlet mass flow was also varied from 2.9 lb/s to 3.3 lb/s. The upper-quadrant area averaged total pressure recovery is plotted against injected mass flow in figure 9-1.

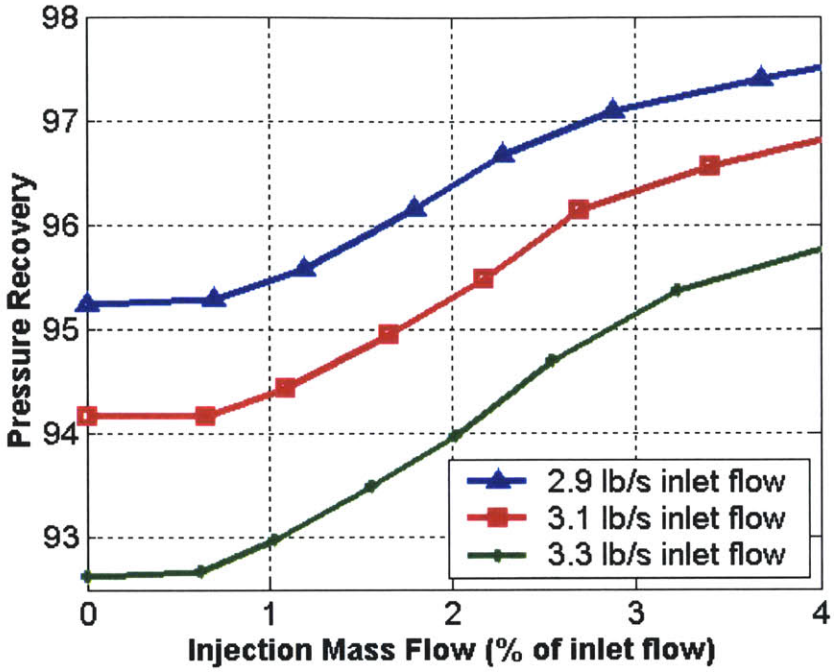

Figure 9-1: Upper Quadrant AIP Pressure Recovery vs Injection Mass Flow

Figure 9-1 shows that periodic separation point injection does improve pressure recovery, verifying the predictions of Amitay et al and the 2-D studies of McElwain. However, the improvements obtained for low mass flows (1 or 2 percent) are relatively poor; improving this performance is the motivation for the parametric study presented next.

9.2 Overview of parametric study

A parametric study of injection designs was performed to explore the effects of $C_{\mu steady}$, stream-wise injection position, and injection angle with respect to the free stream flow direction on the governing parameters of pressure recovery, distortion and unsteadiness. Pressure recovery was the initial metric by which the various injectors were judged, but as the ideal values of these parameters where determined, the improvements in inlet distortion, DC(60) and DPCP were also studied. Plots of upper quadrant area averaged pressure recovery vs. injection mass flow for each injector, along with total pressure profiles of the AIP for each injection mass flow, can be found in appendix D.

9.3 $C_{\mu steady}$

The first parameter studied was $C_{\mu steady}$. $C_{\mu steady}$ is defined here as the ratio of the average injection momentum to the estimated momentum in the separated region,

$$C_{\mu steady} = \frac{\rho_{inj} U_{inj}^2 hl}{\rho_\infty U_\infty^2 A_s}, \tag{9-1}$$

where ρ_{inj} and ρ_∞ are the densities of the injected and free stream air respectively, h and l are the width and spanwise length of the injection slot, A_s is the area of the separated region, U_{inj} is the mean injection velocity, and U_∞ is the freestream velocity.

For injector one, $C_{\mu steady}$ is calculated and plotted against pressure recovery in figure 9-2. From the figure it is clear that pressure recovery increases as the injection momentum increases. It is of course desirable to increase pressure recovery with a minimum amount of mass flow for the practical reason that in a real implementation this mass flow will likely be bled off of the engine and so using a minimum mass flow is desirable. Therefore, in an attempt to increase the injection momentum for lower mass flows, the injection slot width was reduced. Reducing the slot width decreases the injection area and thus, for a given backpressure, increases the injection velocity. The injection momentum is directly related to both the injection velocity and the slot width. Reducing the slot width has a negative impact on momentum, however, because the velocity term is squared it is expected that the overall effect will be an increase in injection momentum that is roughly linearly related to the inverse of the slot height. Because $C_{\mu steady}$ is the ratio of injection momentum to free stream momentum, a concomitant increase in $C_{\mu steady}$ is expected.

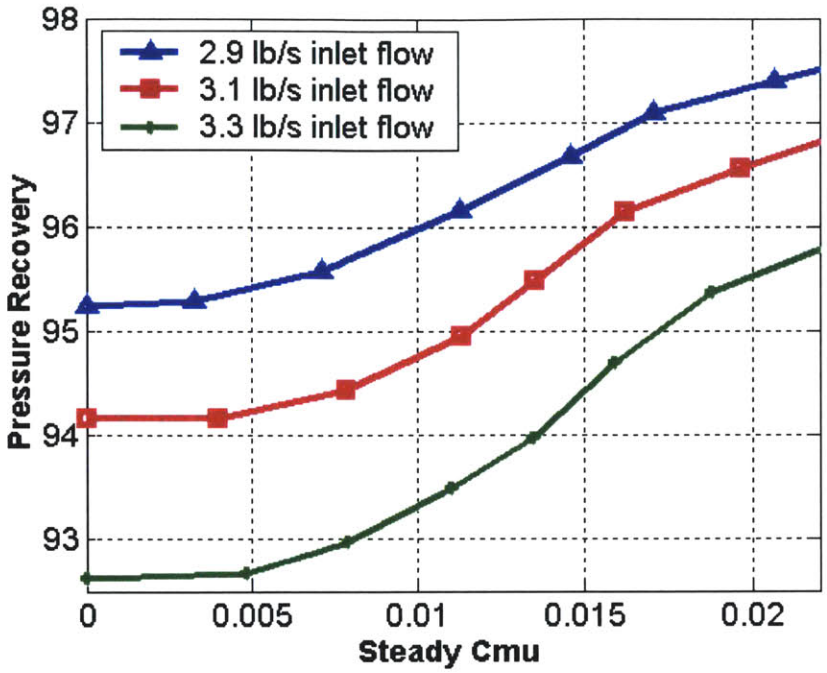

Figure 9-2: Upper Quadrant AIP Pressure Recovery vs $C_{\mu steady}$

Three different slot widths were designed and tested; see injectors One, Two, and Three in Table 8-1. Injector One had a slot width of 0.032 inches, injector Two a slot width of 0.02 inches and injector Three a slot width of 0.01 inches. All other variables were held constant; all injection was introduced at the separation point, and parallel with the inlet flow (zero angle). Data was collected for two different inlet mass flows (2.9 lb/s and 3.1 lb/s) and for a range of injection mass flows (from 1/2 % to 4% of inlet mass flow). Pressure recovery was calculated for each probe in the upper quadrant and then area averaged.

Figure 9-3 is a graph of the change in area-averaged pressure recovery versus slot width for inlet mass flows of 2.9lb/s and 3.1lb/s and injection mass flow of 1% and 2% of the inlet mass flow. From this figure it can be seen that, of the three injectors, the 0.02-inch injector had the greatest effect on pressure recovery. A slot width of 0.01 inches provides some improvement in pressure recovery over the 0.032-inch slot, but the improvement was not as great as the 0.02-inch slot. From these trends, it appears that the optimum slot width is between 0.01 and 0.02 inches.

Because of the small slot widths it was not possible to obtain exit velocity and density data, necessary for calculating C_{μ}, with the unsteady probe. An attempt was made to obtain the needed data using hot wires, however the force of the exit jet caused the hot wires to break. Thus reliable estimates for $C_{\mu steady}$ cannot be provided. It is conjectured, however, that $C_{\mu steady}$ rises as slot width decreases, up to a point at which boundary layer and perhaps shock losses begin to dominate the effect of accelerating the flow. At this point further reduction in the slot width does not increase $C_{\mu steady}$, so the pressure recovery improvement levels off.

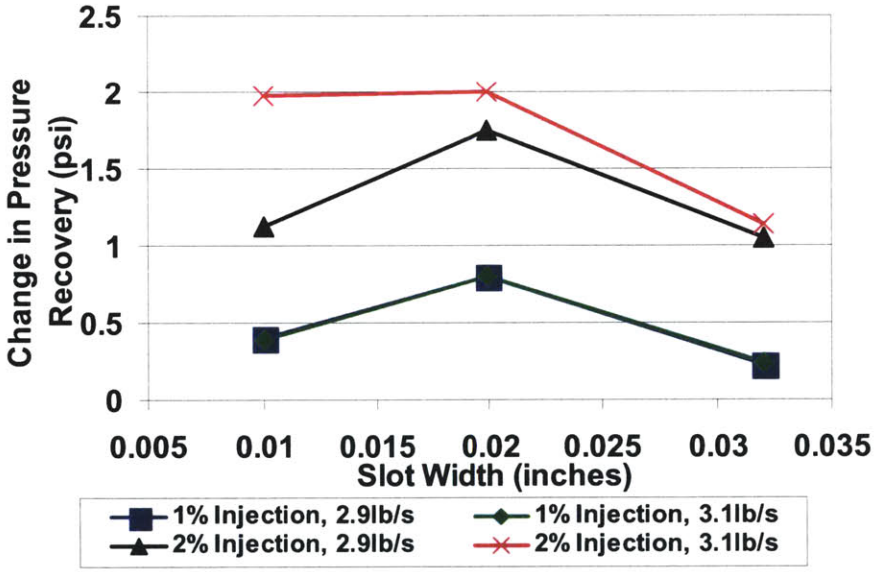

Figure 9-3: Change in Upper Quadrant Pressure Recovery vs Injection Slot Width Figure (slot position = at separation line, slot angle = 0°)

9.4 Stream-Wise Slot Position

The next parameter studied was slot position relative to the separation point. Previous studies have indicated that injecting upstream of the separation line may be superior to injecting at or downstream of the separation point. Thus, injectors Three, Four and Five were designed to determine the optimum position for injection. Again, all other variables were held constant; the width of the injection slot was 0.01 inches for each block and all the injectors ejected flow parallel to the inlet free stream flow.

The appropriate length scale by which to non-dimensionalize the slot position in this inlet is not obvious. Several length scales were proposed including the size of the separation region, and the boundary layer thickness at the point of separation. It was decided to use the boundary layer thickness because it is a well-defined quantity and emphasizes viscous effects on injector placement.

The boundary layer thickness at the separation point in the full-scale UCAV inlet was calculated by Northrop-Grumman using a 3D lifting-surface inflow correction method (see figure 9-4)[65].

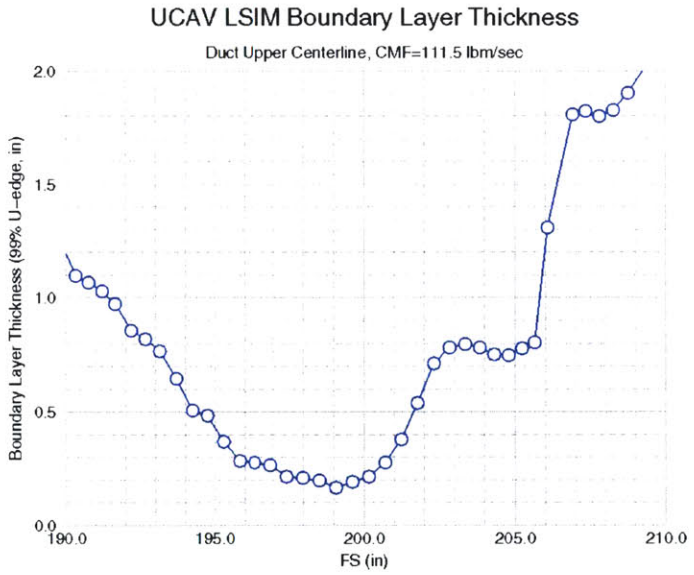

Figure 9-4: Full-Scale Inlet Boundary Layer Thickness

This value was adjusted to account for the differences in size and Reynolds number of the $1/6^{th}$ scale inlet by dividing it by 6 and multiplying by the ratio of the full-scale Reynolds number at the separation point to the $1/6^{th}$ scale Reynolds number at the separation point. This was done by first assuming the velocity profiles of the model and full-scale inlet to be the same. The separation point in the full-scale inlet is at about 209 inches, thus from the figure the boundary layer thickness is $\delta \sim 1.9$ inches. This number was assumed to equate to the Blasius solution for compressible flows over a flat plate, which is,

$$\delta_{full-scale} = \frac{0.37x}{\mathrm{Re}^{1/5}_{full-scale}} \tag{9-2}$$

Thus for the 1/6th scale inlet, the boundary layer was calculated as,

$$\delta_{1/6-scale} = \frac{\delta_{full-scale}}{6} \cdot \frac{\mathrm{Re}^{1/5}_{full-scale}}{\mathrm{Re}^{1/5}_{1/6-scale}} \tag{9-3}$$

The full-scale Reynolds number at the separation point was calculated to be 6.45x10^7, and the Reynolds number in the 1/6th scale inlet was calculated to be 5.55x10^6. Thus the boundary layer in the 1/6th scale inlet was calculated to be δ~0.517 inches, and it was this number that was used to non-dimensionalize the slot position. Note that this boundary layer thickness is different from that reported in chapter 6. That thickness was a conservative estimate, however it is believed that this is a more accurate approximation.

Data was again collected for inlet mass flows of 2.9 lb/s and 3.1 lb/s, upper quadrant pressure recovery was calculated and the change in pressure recovery vs. slot position is plotted in figure 9-5. As can be seen from the figure, injecting behind the separation line shows a substantial improvement in pressure recovery over injecting at the separation line. Injecting 2% inlet flow at the separation line improves pressure recovery by just over 1% for an inlet flow of 3.1 lb/s and by about 2% for an inlet flow of 2.9 lb/s.

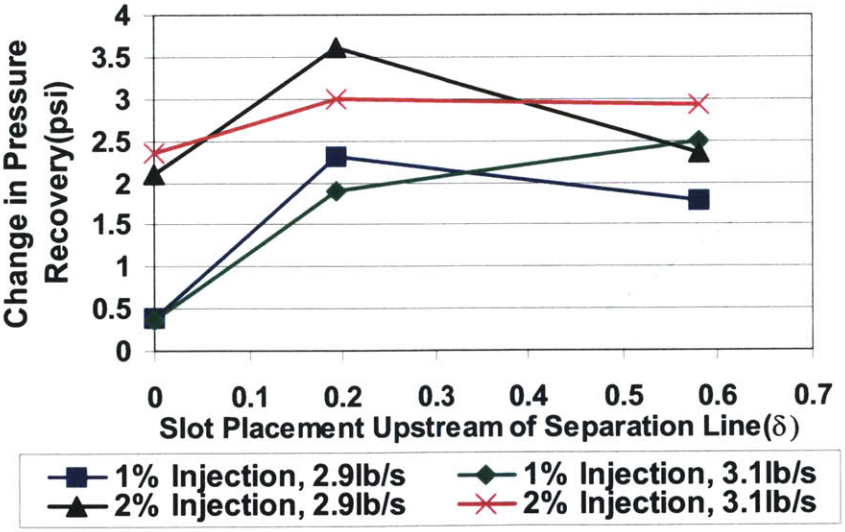

Figure 9-5: Change in Upper Quadrant Pressure Recovery vs Injection Slot Position (slot width = 0.01", slot angle = 0°)

By comparison, injecting 2% inlet flow 0.19δ upstream improves pressure recovery by over 3% for an inlet flow of 3.1 lb/s and by over 3.5% for an inlet flow of 2.9 lb/s, going from 94.49% to 98.09% of total pressure recovered. In addition, the largest gains in pressure recovery from injecting behind the separation line are seen at low injection mass flows, which is of course desirable (see Pressure Recovery vs. injection mass flow plots in appendix D). The figure shows that in many instances, 0.19δ gave the maximum improvement in pressure recovery, however in one case injecting further upstream at 0.58δ continued to improve pressure recovery, indicating that the ideal injection position probably lies somewhere between 0.19δ – 0.58δ upstream of the separation.

9.5 Injection Angle

The final parameter, injection angle (Figure 9-6), was examined to study the effects of this type of injection on secondary flows. If secondary flows are the primary cause of total pressure loss, then injecting at an angle to counter these flows should have a large effect on pressure recovery. Injectors Four, Six, and Seven were designed to study this possibility. Each has a slot width of 0.01 inches and each was placed 0.19δ upstream of the separation line. The angle of injection is measured with respect to the inlet freestream flow direction. Injector Four injects flow parallel to the freestream (zero angle), injector Six injects 6° away from the inlet flow direction, and injector Seven injects 12° away from the inlet flow direction.

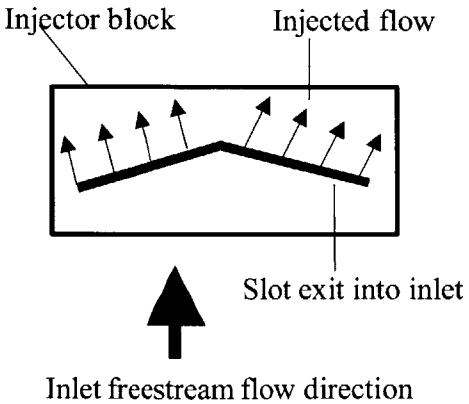

Figure 9-6 – Illustration of Angled Injection (top view)

Figure 9-7 shows the effects on pressure recovery of angled injection. It can be seen that injecting at zero degrees produces a greater gain in pressure recovery than injecting at any positive angle. One would expect that if secondary flows were indeed the primary cause of distortion, injecting at an angle would be superior to injecting directly downstream, and alternatively, if secondary flows are not the primary cause of distortion, injecting at an angle would result in relatively small improvements in pressure recovery. However, the performance of the angled injectors is quite good relative to most of the axial injectors. One simple conclusion that can be drawn from this study is that results are relatively insensitive injector angle; a useful result in highly 3-dimensional inlets whose separation line is either poorly known or changing as a function of operating condition. Injection at an angle to what is eventually deemed to be ideal incurs only a small penalty. Injection position relative to the separation line appears to be more important.

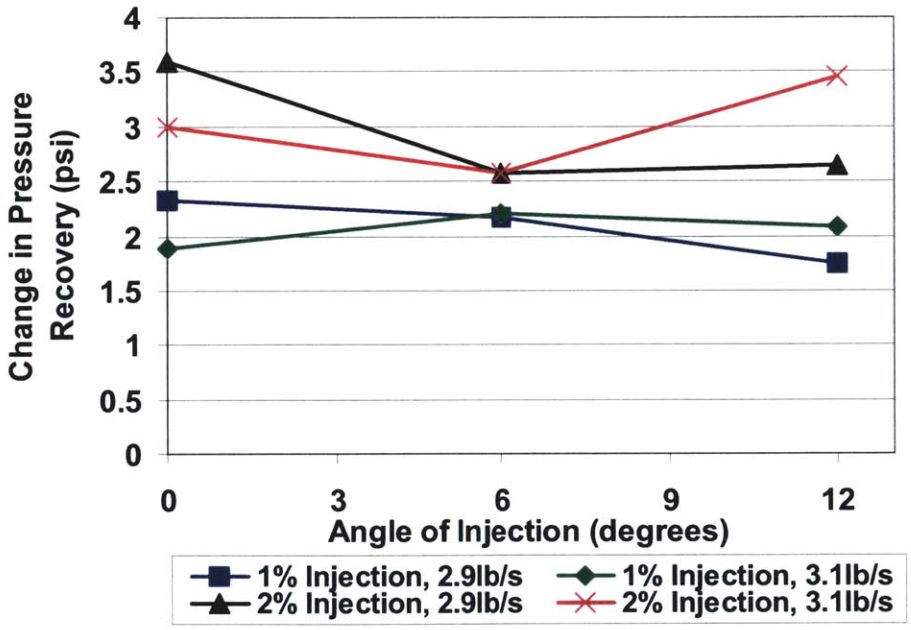

Figure 9-7: Change in Upper Quadrant Pressure Recovery vs Injection Angle (slot position = 0.19δ upstream of separation, width = 0.01")

9.6 Optimized Injector

A final injection configuration was examined in attempt to take advantage of what was learned in the parametric study. Injector block Eight had a slot width of 0.015 inches,

injected flow parallel to the freestream, and was located 0.39δ upstream of the separation line.

As predicted, this configuration returned the greatest improvement in pressure recovery for any given injection mass flow. Figure 9-7 shows area averaged pressure recovery plotted against injection mass flow. This final configuration provided an improvement in pressure recovery of 3.75% for an injection mass flow of 2% of inlet flow at cruise conditions, a recovery of nearly 60% of the original loss. Figure 9-8 provides an illustration of what was achieved through the parametric study by comparing the pressure recoveries from injector One to those of this injector, injector Eight.

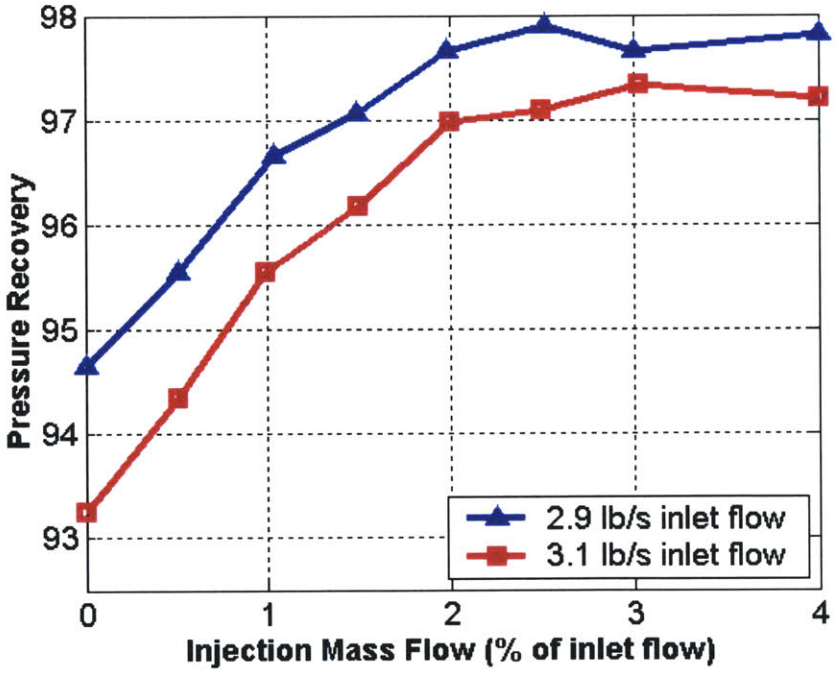

Figure 9-8: Upper Quadrant AIP Pressure Recovery vs Injection Mass Flow

a)

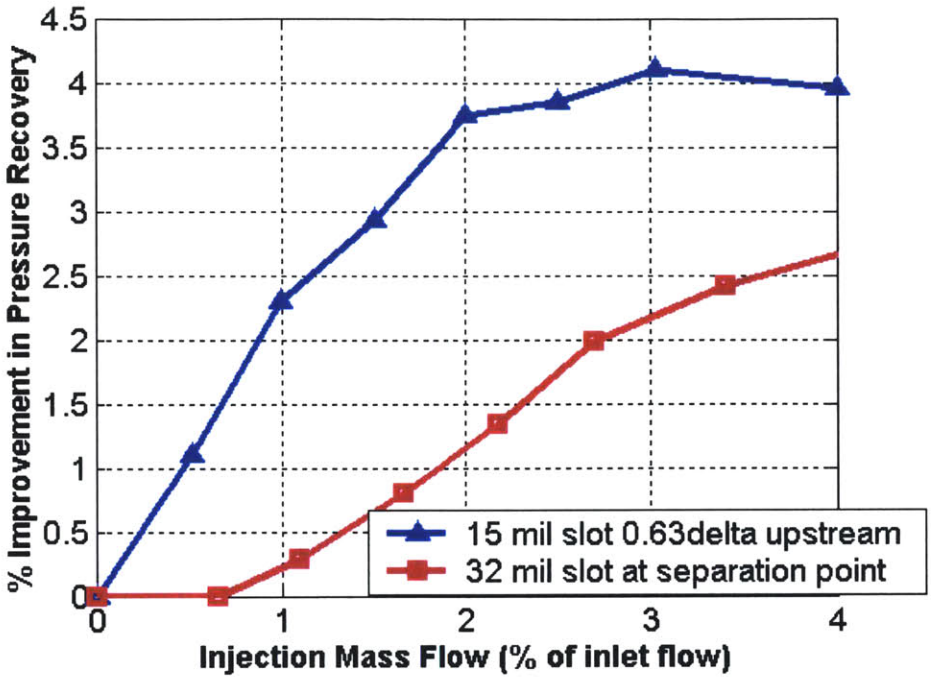

b)

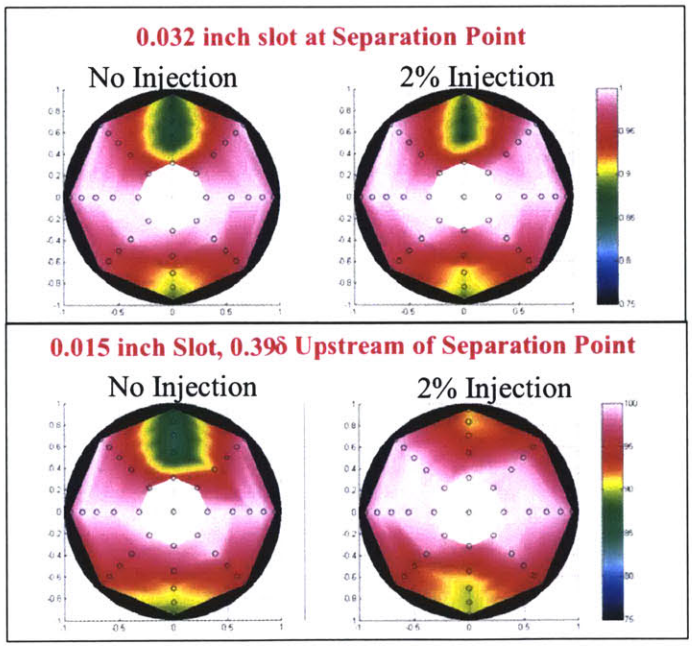

Figure 9-9: a) % Improvement in Upper Quadrant AIP Pressure Recovery vs Injection Mass Flow for Injector Block One and Eight, b) Contour Plots of AIP without Injection and with 2% Injection Through Injector Blocks One and Eight

The improvement in distortion at the AIP resulting from this final injection configuration was examined by way of DC(60) and the circumferential distortion intensity (DPCP).

DC(60) is defined as,

$$DC\,(60) = \frac{\overline{P_t}\Big|_{360} - \overline{P_t}\Big|_{60}}{\frac{1}{2}\rho\overline{c_x}^2} \tag{9-4}$$

where the overbars on the pressures indicate average over the specified range of angles, and c_x is the axial velocity. $\overline{P_t}\Big|_{60}$ is the averaged total pressure over the 60 degrees of the AIP with the greatest distortion. As described in the experimental setup in chapter 8, AIP total pressure probes were placed every 22.5 degrees. Figure 9-9 is a plot of DC(60) for several inlet mass flows. Figure 9-10 shows the same data plotted as a function of inlet Mach number. As can be seen from the figures, injection significantly reduced distortion as measured by DC(60). For an injection mass flow of 2%, for all three inlet mass flows tested, the distortion is reduced by over 60%, and in some cases, by as much as 77% with an injection mass flow of 3% of the inlet flow.

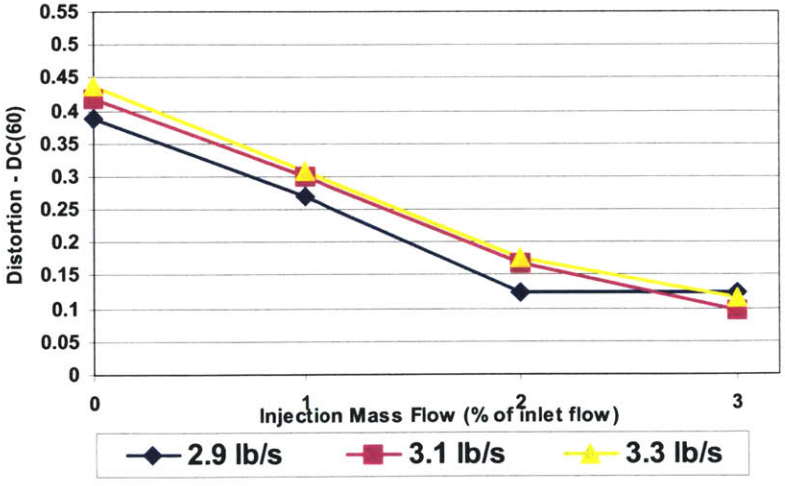

Figure 9-10 – DC(60) at AIP vs Injection Mass Flow

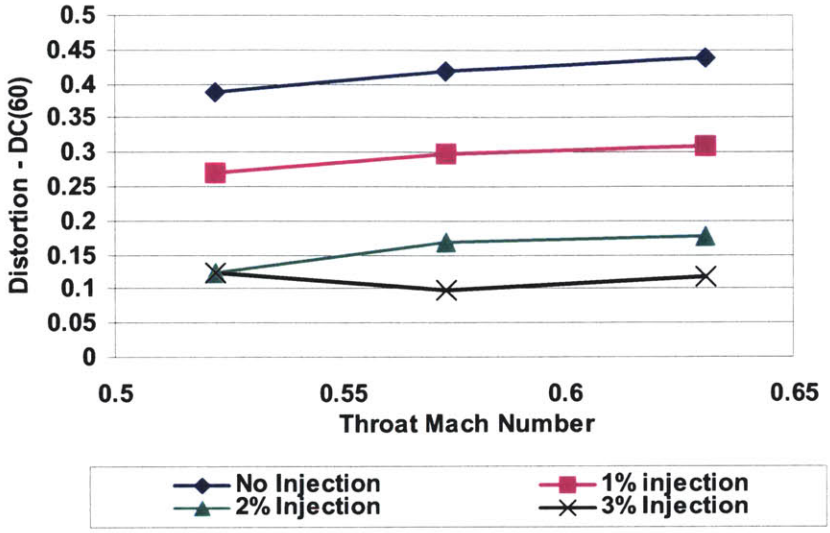

Figure 9-11: DC(60) at AIP vs Inlet Mach Number

DPCP, another way of measuring distortion, is a numerical indication of the magnitude of the pressure distortion. The details of this parameter can be found in the SAE ARP 1420 [64].

DPCP is calculated differently depending on the number and size of distorted regions at the AIP. For the case presented here there are two large distorted regions and thus the distortion intensity is calculated as follows: First the total pressure around the AIP is plotted vs. angle for each ring, i, and a linear interpolation between the points is performed. The average total pressure, $(PAV)_i$ is then calculated and from this the extent of the distorted regions is determined (see figure 9-11). Next the average total pressure of the larger of the two distorted regions, $(PAVLOW)_i$, is calculated. The intensity is then given by:

$$Intensity: \left(\frac{\Delta PC}{P}\right)_i = \left(\frac{PAV - PAVLOW}{PAV}\right)_i \tag{9-5}$$

Figure 9-12 shows an example of how the calculation was done for an inlet mass flow of 3.1 lb/s without injection.

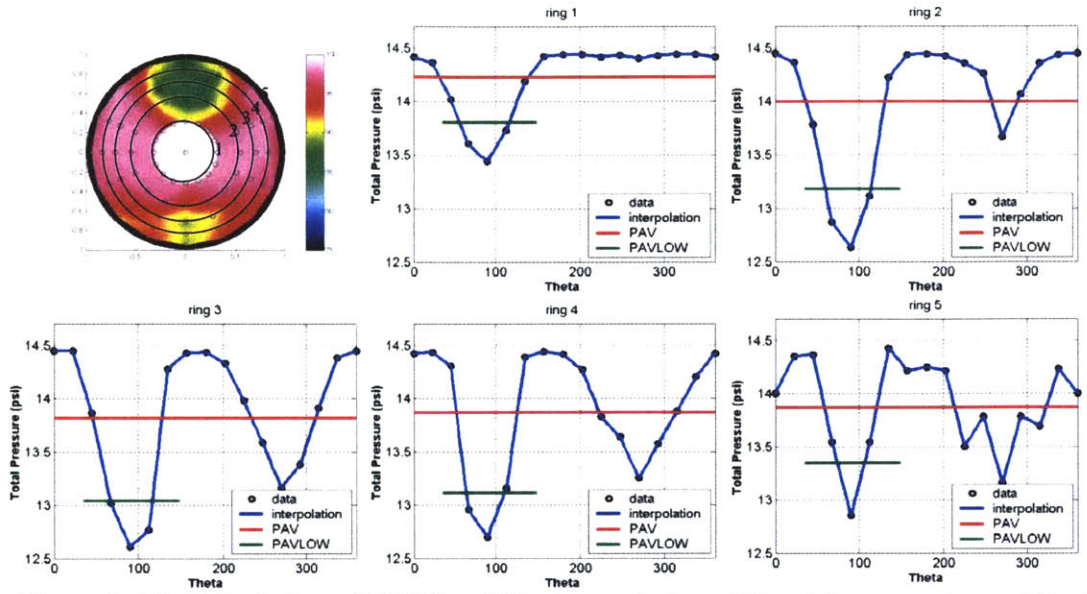

Figure 9-12: Calculation of DPCP at AIP: Interpolation of Total Pressure Around Each Ring at AIP

Figure 9-13 is a plot of DPCP for each ring of the total pressure can, where ring 1 is the innermost ring and ring 5 is the outermost ring, and, again, for inlet mass flows of 2.9lb/s, 3.1lb/s and 3.3lb/s. This figure shows that injection produces significant reductions in distortion intensity. Note that after injection the distortion in the lower half of the AIP is larger than the distortion at the top. According to ARP 1420 guidelines the larger distortion should be used in calculating DPCP, but in this case, because the bottom distortion was ignored for now, DPCP was calculated using only the upper distortion.

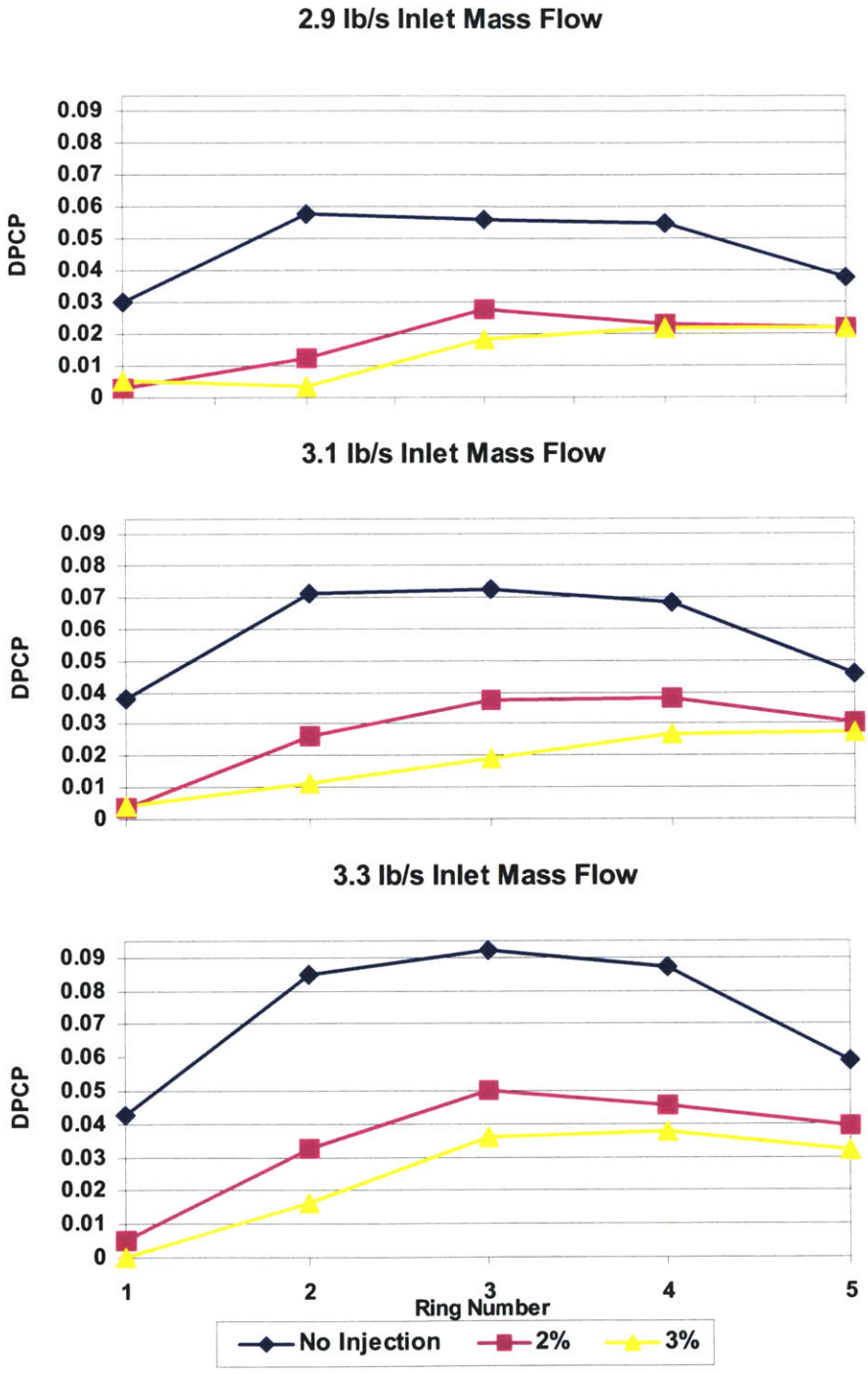

Figure 9-13 – DPCP at AIP vs Ring Number

9.7 Unsteadiness Studies

As mentioned in the introduction, periodic excitation was used in this study because it has been shown to be more effective than steady blowing in many other applications. The effects of periodic excitation on the present case were studied. In particular the effects frequency, mean velocity and amplitude of actuation on the governing parameters were studied. Section 9.7.1 is a discussion of the waveform of the injection flow from the rotary valve, section 9.7.2 shows the effects of frequency on pressure recovery and section 9.7.3 is a discussion of the relation of mean and peak oscillation to pressure recovery. An attempt was made to increase the amplitude of oscillation by reducing leakage through the rotary valve. This is discussed in section 9.7.4.

9.7.1 Waveform

The actuator used in the above studies, the rotary valve described in chapter 8, allowed for the adjustment of the actuation frequency from approximately 50 Hz to over 2500 Hz and essentially produced a sin wave signal. Figure 9-14 shows and example of the exit velocity from an injector block for a given mass flow; injector Two, with mass flow of 0.062lb/s or 2% of the inlet flow at cruise conditions, was used in this case. Total pressure was measured right at the exit of the injector on the bench and velocity was calculated by using the isentropic flow equations,

$$M = \sqrt{\frac{2}{\gamma - 1}\left[\left(\frac{P_T}{P_{atm}}\right) - 1\right]} \tag{9-6}$$

$$V = M\sqrt{\gamma RT} \tag{9-7}$$

$$T = \frac{T_{atm}}{1 + \frac{\gamma - 1}{2}M^2} \tag{9-8}$$

where P_T is the measure total pressure at the exit and T_{atm} and P_{atm} are the ambient total pressure and temperature respectively.

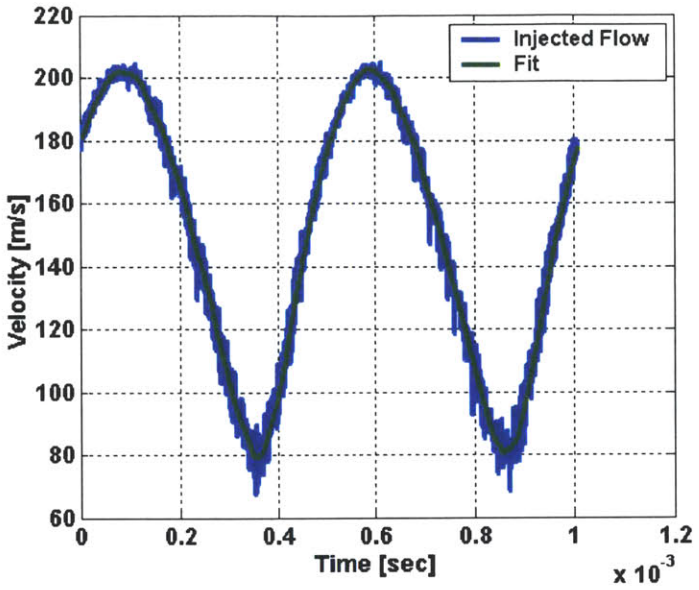

Figure 9-14: Waveform from Injector Two

The minimum, mean and maximum velocity obtained from injector Two for a range of pressure ratios (the ratio of the back pressure to the exit pressure) is plotted in figure 9-15.

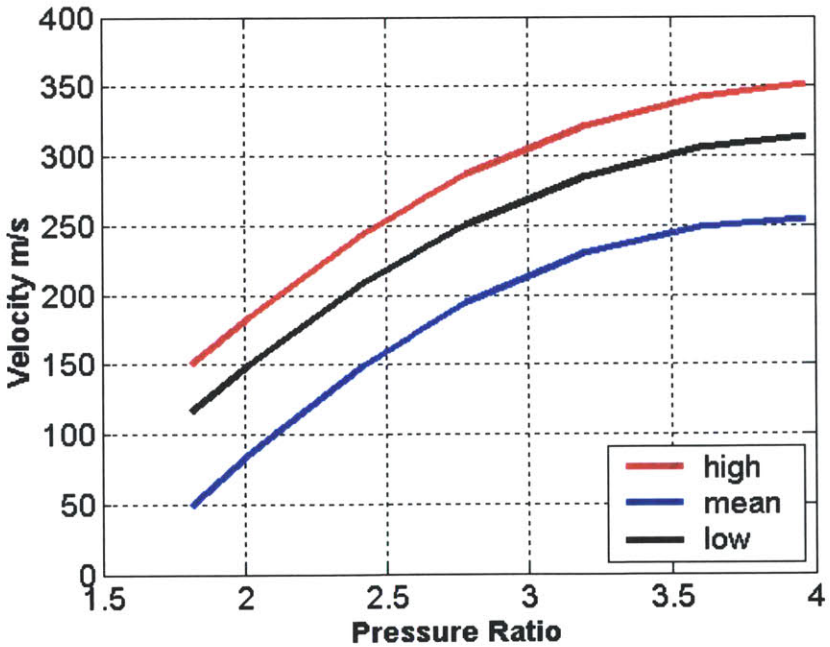

Figure 9-15: Maximum, Minimum and Mean Velocity of Injection Flow (measured at injector exit) vs Pressure Ratio

9.7.3 Frequency

A frequency sweep was performed while inlet mass flow and injection mass flow were held constant. Figure 9-16 shows that pressure recovery improves with actuation frequency up to about 800 Hz, after which there is little additional improvement except for a small peak at about 1600 Hz. Note that 800 Hz is approximately the vortex shedding frequency. This figure shows that the dominant effect on pressure recovery comes from steady blowing.

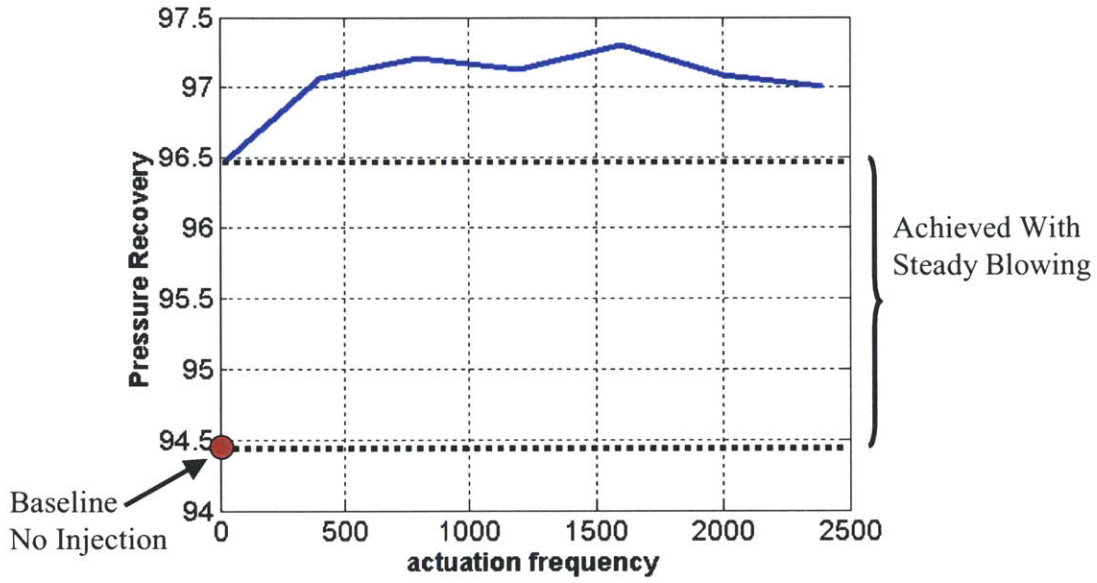

Figure 9-16: Upper Quadrant Pressure Recovery at AIP vs Actuation Frequency (injector Eight, inlet mass flow = 3.1 lb/s, injection mass flow = 2% of inlet flow)

9.7.2 Mean and Peak Oscillation

It was thought that an oscillation about the inlet mean flow velocity would provide the greatest improvement in pressure recovery. Figure 9-17 shows the pressure recovery versus injection mass flow for injector Two, with an inlet mass flow of 3.1 lb/s. Two points in the figure are highlighted and the injection velocities at those two mass flows are plotted along with the inlet freestream velocity. For injector Two, with a 2% flow, it can be seen that for most of the cycle, the injection velocity is below the inlet freestream velocity and, conversely with ~4% flow the injection velocity is greater than the freestream for most of the cycle.

What this figure does not show is the need for a high maximum injection velocity or a zero minimum velocity in order to achieve some improvement in pressure recovery. The first mass flow highlighted in Figure 9-17 shows a mean injection velocity that is well below the mean inlet velocity. The second highlighted mass flow shows a mean and peak injection velocity that is well above the inlet mean velocity. In both cases an improvement in pressure recovery at the AIP is achieved. The improvement is greater for the higher mass flow case, however it is unclear if this is due to the increase in mean injection velocity or peak injection velocity.

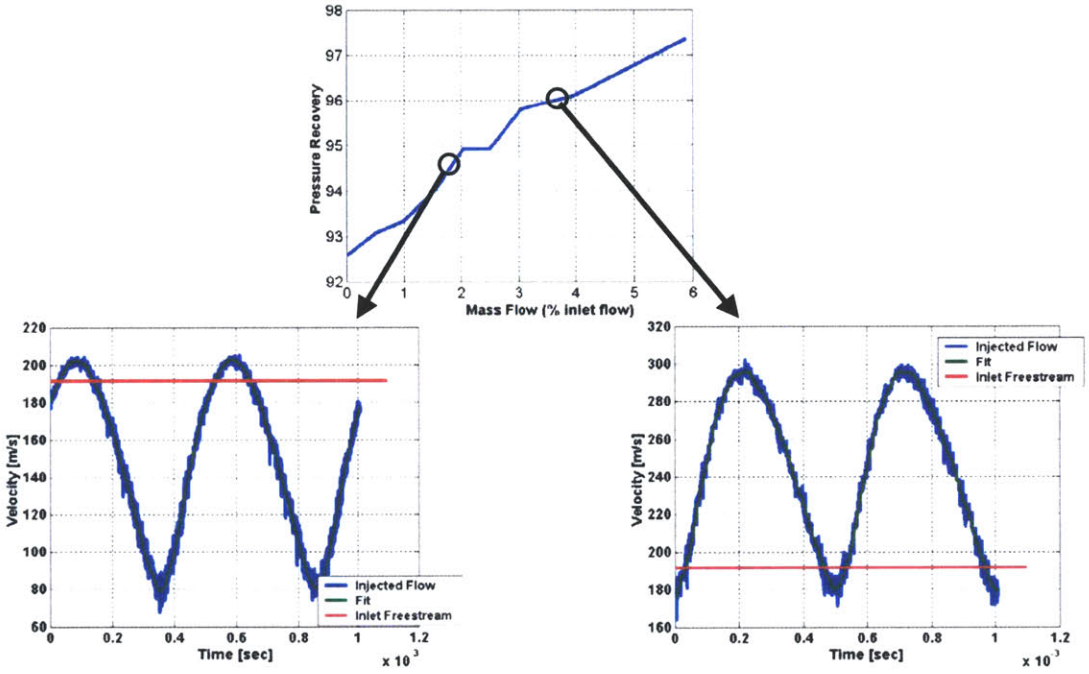

Figure 9-17: Top Figure: Upper Quadrant Pressure Recovery vs. Injection Mass Flow (injector Two, inlet mass flow = 3.1 lb/s), Bottom Figures: Waveform From Injector with Inlet Mean Flow Superimposed

If the velocity of the injection flow is always lower than free stream, the low momentum flow will result in the introduction of another source of loss. On the other hand, if very high velocity injection (high mass flow) is introduced this will be expensive and the improvements in pressure recovery result just from brute force, not necessarily from changing the characteristics of the flow.

9.7.4 Amplitude

As mentioned in chapter 8, the actuator leaked when it was closed. This limited the maximum amplitude of oscillation that could be achieved for a given pressure ratio, by making the minimum greater than zero, and thus limited the value of unsteady C_μ ($<C_\mu>$). McElwain showed that the values of $<C_\mu>$ from this actuation configuration were lower than those shown to be successful in other studies [3], [21]. An attempt was therefore made to improve the duty cycle, and increase $<C_\mu>$, by redesigning the rotor to reduce leakage. The sources of leakage were identified to be the clearance areas, which were necessary to allow the rotor to spin freely within the valve body. This was exacerbated by the many holes in the rotor, which stored mass and served as alternate pathways for the flow to pass. A new rotor was designed which had tighter clearances. This new rotor still had 10 exit chambers (this time rectangular slots rather than circular holes), but an insert was added which prevented flow from passing into any of the chambers that were not aligned with the exit (see figure 9-18).

It was hoped that these changes would result in larger amplitude by reducing the leakage. Figure 9-19 shows a comparison of the minimum and maximum velocities measured at exit of injector Two. The alterations to the rotor clearly resulted in greater amplitude although significant leakage still existed. Figure 9-20 shows a plot of pressure recovery versus injection mass flow for injector Eight, with an inlet mass flow of 3.1 lb/s. The figure shows a direct comparison of the old rotor and new rotor. As can be seen from the figure, the modifications had little effect on the overall change in pressure recovery. Several different conclusions could be drawn from this; the first is that amplitude has little effect in general at high subsonic conditions, but another view would be that the amplitude was not increased significantly enough to see an effect. Thus, unfortunately, the results are inconclusive.

a)

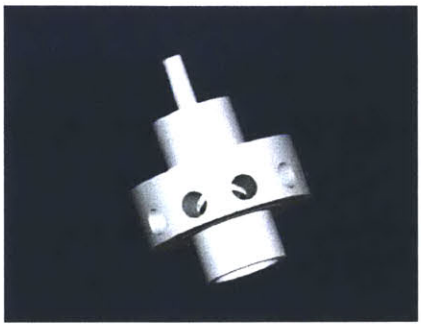

b)

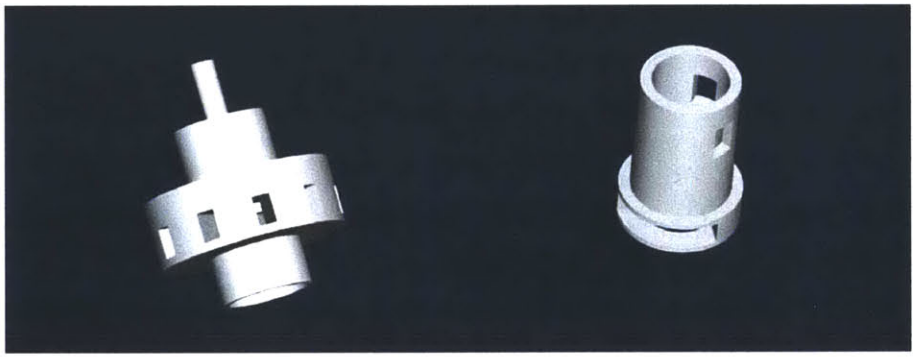

Figure 9-18: a) Old Rotor, b) New Rotor and Insert

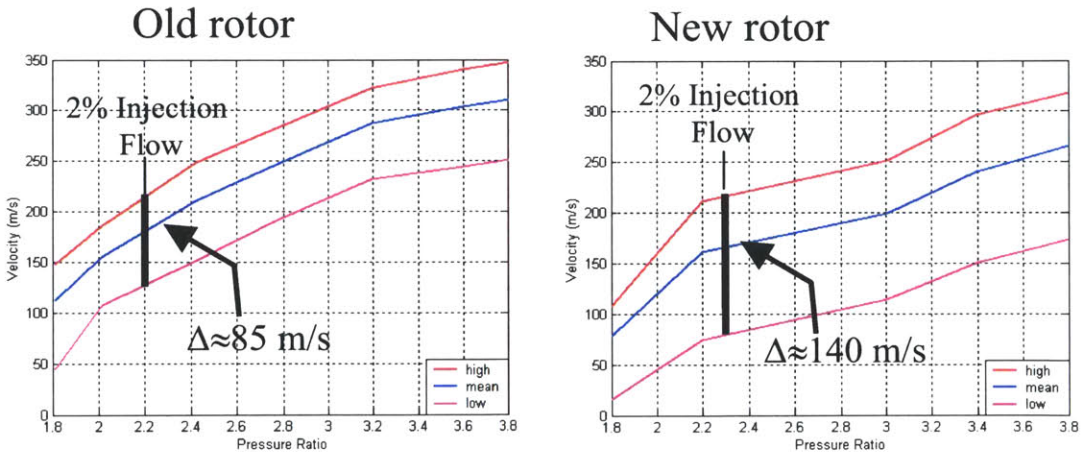

Figure 9-19: Maximum, Mean and Minimum Velocity of Injection Flow (measured at injector exit) vs Pressure Ration for Old Rotor and New Modified Rotor

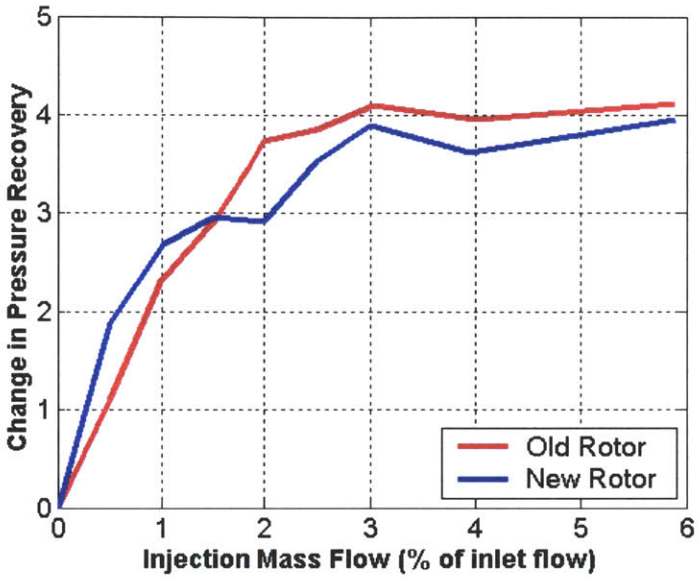

Figure 9-20: Upper Quadrant Pressure Recovery vs Injection Mass Flow Using Old Rotor and New Rotor

9.8 System Analysis

An attempt was made to compare the effort put into the system by injecting to the improvement gained from it. A representation of the system is shown in Figure 9-21. Flow is injected into the inlet and a shock is formed near the injector exit.

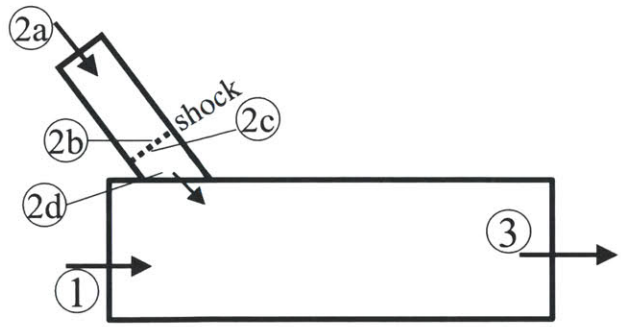

Figure 9-21: Illustration of System

The system is adiabatic and thus, according to the first law,

$$0 = \sum \dot{m}(h + \frac{v^2}{2} + gz) \tag{9-9}$$

Where h is the enthalpy, v is the velocity of the flow, g is the gravitational constant and z is a height. The gravitational term is negligible and can be dropped. At point 2a, the air is slow-moving and thus the enthalpy term dominates and the energy of the flow is approximately,

$$\dot{m}c_p T_0 . \tag{9-10}$$

From experimental data, for a mass flow of 2% of the inlet flow, this number was calculated to be ~8,400 J/s.

The flow then accelerates to point 2b, where a shock occurs. The kinetic energy is now important and the energy at 2b is,

$$\dot{m}c_p T_b + \frac{u_b^2}{2} \tag{9-11}$$

The flow then passes through the shock, which is assumed here to be a M=1.5-2.0 shock, and the energy is now,

$$\dot{m}c_p T_c + \frac{u_c^2}{2} \tag{9-12}$$

The flow then accelerates up to approximately Mach 1 at the exit of the injector, and the energy injected into the flow is,

$$\dot{m}c_p T_d + \frac{u_d^2}{2} \tag{9-13}$$

Compressible flow tables were used to find approximately how much of the enthalpy at 2a was converted into kinetic energy at point 2d. This gives an indication of the kinetic energy introduced into the flow through injection. It is the kinetic energy that will have the desired effect on the flow in the inlet and thus the kinetic energy that is of interest. From the tables, going from point 2a to 2b gives, $T_b=0.5556T_a$ for a Mach 2 shock ($T_b=0.6897T_a$ for a Mach 1.5 shock), across the shock the temperature ratio is, $T_c=1.688T_b$ ($T_c=1.32T_b$ for a Mach 1.5 shock), and after the flow accelerates back to Mach 1 the temperature ratio is, $T_d=0.8333T_c$. After solving it can be seen that about 22%-24% of the enthalpy at 2a is converted to kinetic energy at point 2d. Thus the

kinetic energy put into the system is on the order of 1,850-2,020 J/s (ignoring for now any other losses through the system other than the shock).

The kinetic energy at the AIP was calculated both before and after injection in order to get an indication of the change in kinetic energy induced by injection. Static and total pressure was measured at the AIP from the static taps and the forty equal-area total pressure probes described in chapter 8. From this, velocity and density were calculated and the area averaged kinetic energy obtained. For consistency, the change in kinetic energy was calculated for the upper quadrant of the AIP only, although the energy flux change across the rest of the AIP is small. For an injection mass flow of 2%, at cruise conditions, the change in kinetic energy flux at the AIP was calculated to be approximately ~800 J/s or about 40% of the energy reported above as that which was added to the system. However, that number fails to account for the losses through the rotary valve and injector block, and to account for the fact that the injector creates a pulsed flow and thus the maximum energy is only added periodically.

An attempt was made to measure the kinetic energy at the exit of the injector in order to account for the losses through the system. This was done by measuring the static and total pressure at various points along the exit of the slot on the bench and then interpolating to obtain a velocity profile at the exit. A profile was obtained for both the maximum injection velocity (i.e. when the rotor is fully open) and the minimum injection velocity (i.e. leakage flow). From these profiles, estimates of the average minimum and maximum kinetic energy of injection were made. For a 2% injection flow, the maximum kinetic energy added to the system by way of injection was found to be ~250 J/s and the minimum to be ~50 J/s. However because this data was taken on the bench it is difficult to match the conditions of the inlet. Table 9-1 shows an accounting of the energies reported above.

Calculated Kinetic Energy Flux at Injector Exit	Measured Kinetic Energy Flux at Injector Exit		Measured Change in Kinetic Energy Flux at AIP (top quadrant)
	Maximum	Minimum	
1850 - 2020 J/s	250 J/s	50 J/s	800 J/s

Table 9-1: Kinetic Energy Flux in Joules per Second at the Injector Exit and Change in Kinetic Energy Flux at the AIP

It would be desirable if the change in kinetic energy at the AIP were greater than that which is added to the system. This would mean that injection in the boundary layer near the separation is serving to alter the dynamics of the inlet flow and that the improvements seen at the AIP do not result simply from the addition of mass flow. The analysis of the energy described above indicates that this very well may be the case, however, a more thorough and detailed study needs to be performed in order to be sure.

10 NEW ACTUATOR – FLUIDIC DIVERTER

10.1 Objectives

The design and use of a new actuator were investigated with several goals in mind. The first was to improve the duty cycle by making an actuator that would leak less during the "off" part of the cycle. A second goal was to create an actuator that would be virtually maintenance free and capable of surviving the harsh conditions it could be subjected to in a UCAV inlet. There are currently no off-the-shelf actuators that would serve the purposes of this research.

10.2 Design

The concept of a fluidic diverter was used. A fluidic diverter is a device that creates an oscillation using feedback channels. Flow is passed through a nozzle in the diverter. It can then travel down either of two output legs. The jet stream tends to stick to the walls of one or the other output channels due to the Coanda Effect (see section 8.2). As the flow travels down one of the output channels, it pressurizes a chamber in the diverter which is connected to a feedback channel. The feedback tube channel creates a small jet near and perpendicular to the exit of the nozzle. This jet serves to force the flow from the jet to the other output channel. A similar feed back mechanism forces the flow back down the other first output channel and a pulsed flow is created. For a more detailed account of how a fluidic diverter works, see [66]. The length and area of the chambers serve to alter the frequency at which the flow oscillates back and forth. The fluidic diverter designed and tested in this research (see figures 10.1 and 10.2) was based on a design by Dr. Guenette [56]. The diverter sat on a base, which adapted it for use in the inlet. One channel of the diverter was fed into the inlet, through the base, and the other channel was vented to the atmosphere, outside of the inlet. The diverter and base were constructed entirely from aluminum in the Gas Turbine Laboratory at MIT.

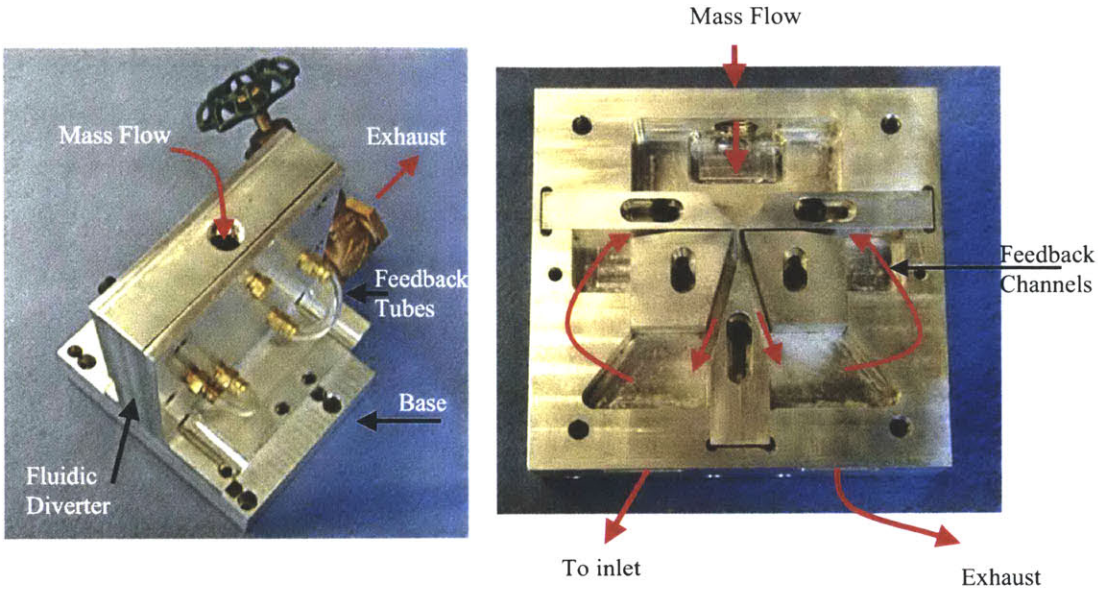

Figure 10-1: Fluidic Diverter

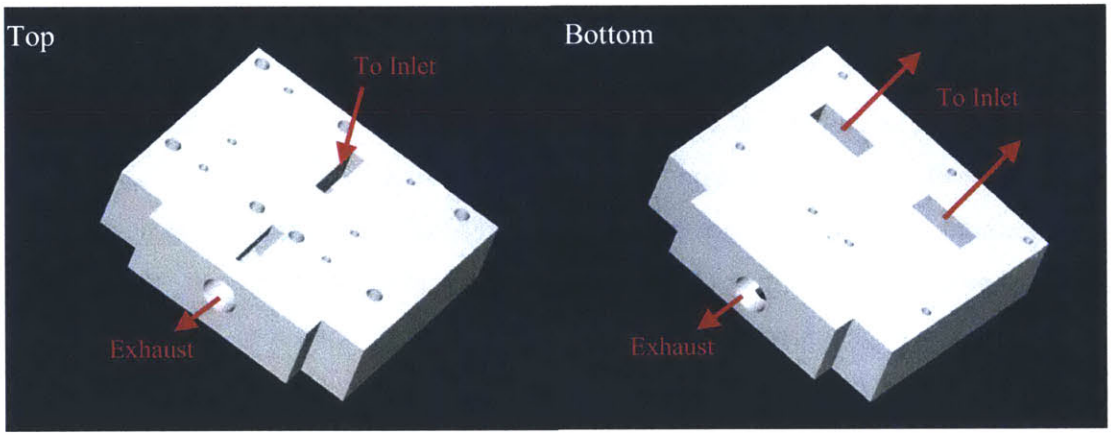

Figure 10-2: Fluidic Diverter Base Used to Adapt Diverter to Inlet

10.3 Experimental setup

10.3.1 Bench

The diverter was first bench tested to verify that it would provide a periodic signal. The oil free compressor was again used to provide the mass flow for actuation. The diverter is sensitive to the many adjustable parameters such as the internal areas of the flow passages and the tube lengths between the channels. These were adjusted to

provide that maximum frequency possible. An unsteady pressure probe was used to measure the frequency and amplitude of the signal.

10.3.2 Inlet

The inlet setup was nearly identical to the setup used for the rotary valve with one notable difference. The static pressure in the inlet at cruise conditions is about 11 psi. In order for the diverter to work, it was necessary that the static pressure of the exhaust be pulled down to a lower pressure, rather than just venting to the room (~14.7 psi) otherwise the flow would only pass through the passage with the lower exit static pressure and would not oscillate. A steam ejector, which pulls vacuum by forcing high pressure steam through adjacent duct work was used to pull a vacuum on the exhaust exit and enabled the diverter to work in the inlet.

10.4 Results

The maximum frequency from this diverter was found to be 350 Hz. For low mass flows this actuator was found to have a larger amplitude than the rotary valve, however as the mass flow increased, it too leaked and thus the amplitude was not as large as it could be. Because only half of the mass flow was passed into the inlet (the other half being vented) a higher mass flow was needed to achieve the same fractions of inlet mass flow used for injection as were used with the rotary valve. This meant that the leakage flow from the diverter unfortunately ended up being very similar to that of the rotary valve.

Injector block Eight was used for all of these tests. At an inlet mass flow of 3.1 lb/s, an injection mass flow of 2% of the inlet flow (after discounting the flow that was exhausted and not passed into the inlet) was found to improve pressure recovery by 1.4%.

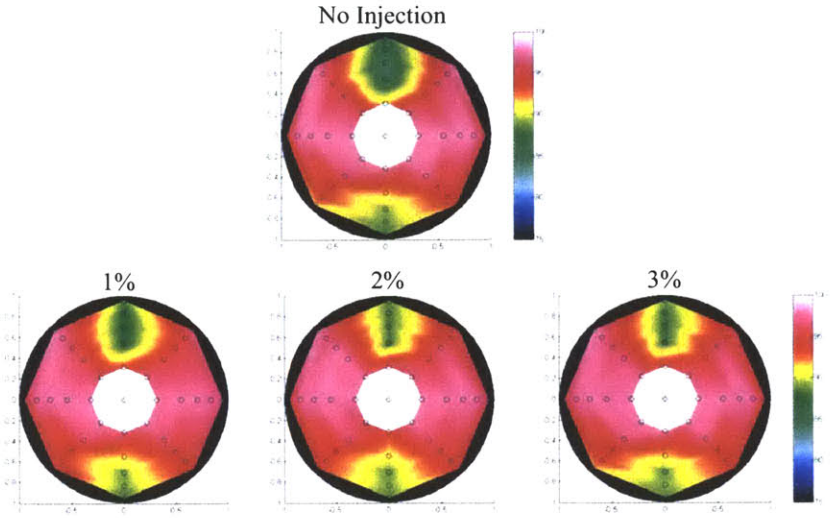

Figure10-3: Total Pressure Contour Plots of AIP Without Injection and With Injection Mass Flows of 1%, 2% and 3% of the Inlet Flow

The actuator served as a rough cut at constructing an actuator with no movable parts, making it robust and relatively maintenance free. Additionally it was an attempt to improve the duty cycle. Unfortunately the frequency was not as high as desired and it provided only marginal improvements in duty cycle. However, these studies do show that this type of actuator could work for this type of application. The actuator could quite easily be improved upon by designing it to produce higher frequencies, and making adjustments to reduce leakage (i.e. wider pathways, greater vacuum for the exhaust exit, etc.).

After using the diverter in much the same way as the rotary valve, i.e. injecting pulsed air with an off-on cycle, the base was removed and the diverter was put to a new use. The base was removed so that all air was injected into the inlet, but injected in a side-to-side way. This was done in order to examine the effect on the two vorticies that form on either side of the inlet. If the frequency could be matched to the shedding frequency, it could produce some interesting effects of either more efficiently countering the vortices, or alternatively, exacerbating the vortices and resulting in a bigger problem.

In fact, a substantial improvement was found. Figures 10-4 and 10-5 show the effect of this type of injection on pressure recovery. Figure 10-6 shows a direct comparison of the performance of rotary valve and fluidic diverter. Though the improvements are not as good as those seen with the rotary valve, they are substantial improvement and warrant further investigation.

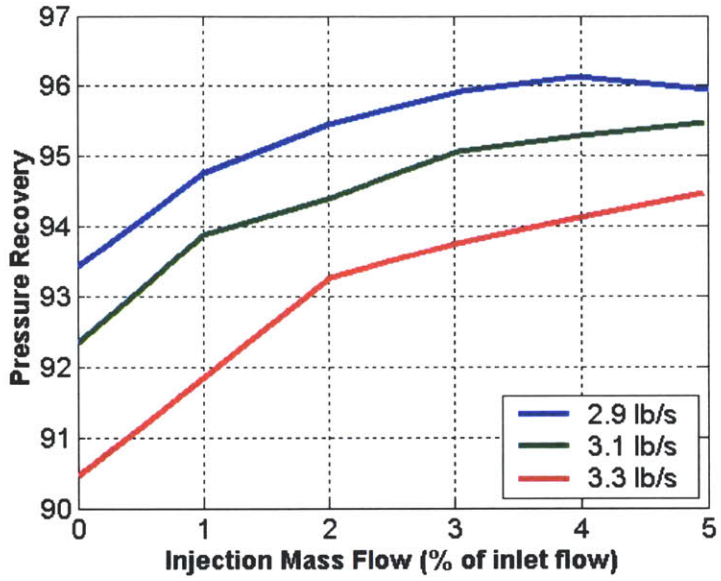

10-4: Upper Quadrant Pressure Recovery at AIP vs Injection Mass Flow with Diverter Base Removed

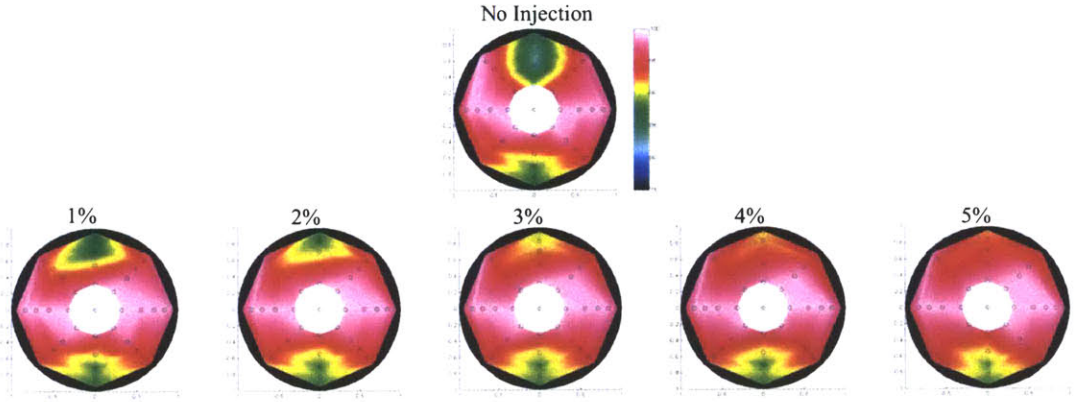

Figure10-5: Total Pressure Contour Plots of AIP Without Injection and With Injection Mass Flows of 1% - 5% of the Inlet Flow with Diverter Base Removed

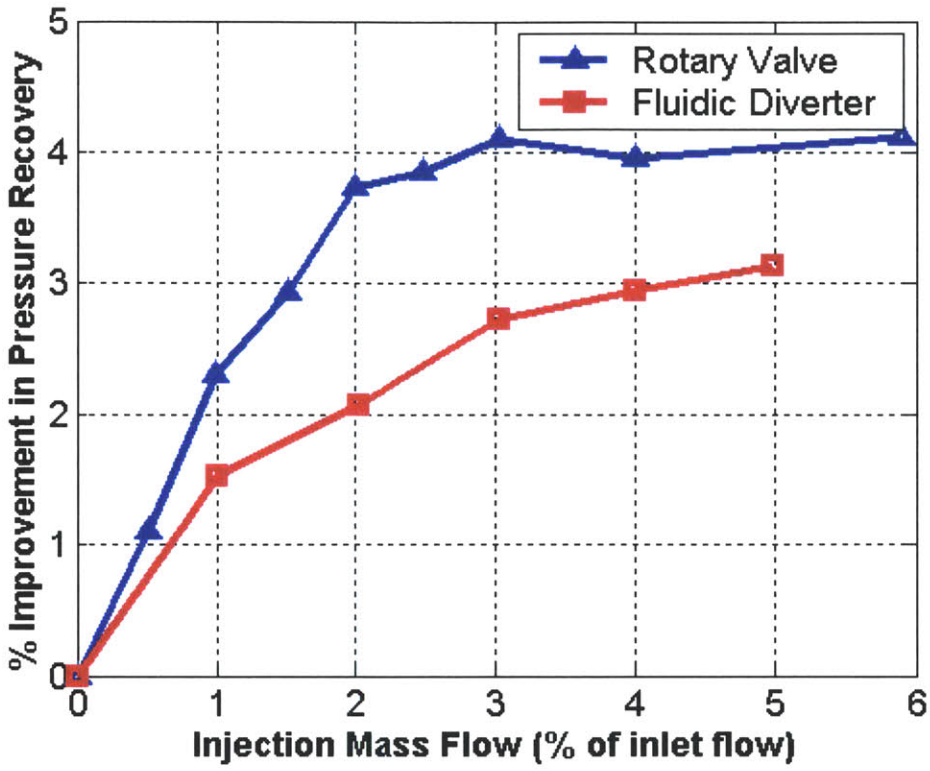

Figure 10-6: % Improvement in Upper Quadrant Pressure Recovery vs Injection Mass Flow (inlet mass flow = 3.1 lb/s, injector Eight)

SECTION 4 - CONCLUSION

11 CONCLUSIONS AND RECOMMENDATIONS

11.1 The UCAV

The Predator and Global Hawk UAVs showed that the most successful UAV programs were those that could effectively performs an important mission, but with the right combination of cost, capability and survivability, exploiting the most unique attribute of any UAV, the fact that they are attritable. DarkStar showed that survivability is only desirable in unmanned air vehicles so far as it does not significantly drive up costs or limit other capabilities. Furthermore, the Predator and Global Hawk found their niche in the force mix; developers exploited the fact that they are attritable and made a vehicle that could cost effectively complete a valuable mission.

Likewise, a niche exists for the UCAV within the force mix. However, the degree to which the UCAV takes advantage of that niche will depend upon the ability of developers to optimally balance cost, capability and survivability. The speed with which the UCAV will be introduced into the force mix and in what quantity and capacity it will be used will depend upon how well developers exploit the UCAV's niche. The strongest attributes of the UCAV are that it is more capable than a cruise missile and more attritable than a piloted vehicle. The UCAV can best take advantage of these attributes by focusing less on survivability and much more on keeping costs low. The cruise missile and JSF should serve as rough guides as developers try to find the correct balance to the cost-capability-survivability equation.

Current development programs include the X-45C and the X-47B. Both of these UCAV designs focus on making a very capable vehicle that is highly stealthy and as a consequence of both of these, will also likely be very expensive. In doing so, these developers risk repeating the mistake of DarkStar. This could result in delaying the time till the UCAV is introduced into the force mix and used to its greatest potential, as it could be lose out in the near term to the JSF and cruise missile for procurement funds. Likewise, the door may be open for another UCAV program, one that focuses less on survivability and can cost effectively perform a SEAD mission and other strike missions.

11.2 Flow Control

Flow control is an emerging technology that could help UCAV programs to design a vehicle for survivability while reducing cost and improving performance. As such, designers should look to incorporate flow control technology into the UCAV.

11.2.1 Sensors

The method of Rathnasingham and Breuer was confirmed for its relevance for use in a real inlet at high subsonic conditions as it provided a filter that greatly improved the ability to characterize the flow at the AIP through the use of hot-film sensors in the upstream separated flow region.

Using multiple sensors further improved this ability and provided the further advantage of greater flexibility in sensor placement, ensuring that sufficient information can be obtained from upstream wall based sensors over varying conditions, thus making it a more likely possibility for actual implementation in a UCAV.

It was found that the more sensors used the better (up to the 18 we had), however, very little is gained from using more than 6 or 7 well placed sensors. The number of sensors used should be limited by the computing time. The more sensors used, the longer it will take to compute the filter and if this system is to be implemented in a feed-forward control scheme, the time will be limited by the flow convection time (about 6 milliseconds in the full-scale inlet). The locations of greatest correlation were along the stagnation line, along the stream-wise sides of the separation, and in the upstream center of the stagnation region.

Future work should develop the necessary control laws and test this scheme in an integrated inlet-compressor system.

11.2.2 Periodic Injection

After adjusting several parameters, $C_{\mu steady}$, injection slot position, injection angle, and injection frequency, periodic separation point injection was found to significantly improve pressure recovery and reduce distortion in a UCAV inlet with 3D geometry at high subsonic conditions. With an injection mass flow of 2% of the inlet mass flow, pressure recovery was improved by 3.75% (a nearly 60% reduction in the losses). With the same mass flow, distortion as measured by DC(60), was reduced by over 60% and distortion intensity, as measured by DPCP, was also significantly reduced.

$C_{\mu steady}$ was found to be an important parameter and optimizing this value is important for optimizing performance. For this system, it was found that a value of $C_{\mu steady}$ that is too low will result in sub optimal performance. Performance improves with increasing $C_{\mu steady}$ in this system until shock and viscous loses through the injection slot begin to dominate. The precise value of $C_{\mu steady}$ was not measured because of the extremely small exit slot, however, the ideal exit slot of those studied here was found to be 0.015 inches wide. It would be worthwhile in future work to devise a method to measure the unsteady total pressure at the exit of these very small injector slots so that $C_{\mu steady}$ could be calculated and reported. Ideally, a method would be devised which would allow for the measurement of the unsteady total pressure at the injection slot exit while the injector is in the inlet, such as one or more flush mounted hot-film sensors at the slot exit.

The slot placement relative to the separation point was found, in these studies, to be the most important parameter. It was found that injecting behind the separation line was greatly superior to injecting right at the separation. In addition, evidence suggests that injecting too far behind the separation decreases performance. The best position studied here was 0.39δ.

Injecting at an angle relative to the inlet freestream flow direction provided mixed results but indicated that the system is relatively insensitive to injector angle, a useful result in highly 3-dimensional inlets whose separation line is either poorly known or changing as a

function of operating conditions. Future work could focus on further exploring the secondary flows in this inlet through further flow visualization and through testing with injection at various angles not studied here, including negative angles.

Periodic blowing was found to be superior to steady blowing, however the improvement is much lower than reported elsewhere. It was thought that improving the duty cycle by reducing actuator leakage would emphasize the value of periodic blowing. An attempt was made to improve the duty cycle by modifying the existing rotary valve to limit leakage. The modification did improve the duty cycle, but provided little if any improvement in pressure recovery at the AIP. The improvement in duty cycle was perhaps not significant enough to see a difference. However, the improvement in pressure recovery seems to be more dependent upon the mean or maximum velocity of injection rather than the amplitude.

A new actuator was developed and tested. The actuator was a fluidic diverter and as such it had no moving parts but relied on pressure differentials to provide periodicity. The actuator's performance was inferior to the rotary valve in terms of improving pressure recovery and reducing distortion at the AIP. This is due in part to the fact that it was only capable of providing an actuation frequency of about 350 Hz, and the duty cycle was about the same as that of the rotary valve. However, this actuator shows promise as a method that could be optimized and used for actual implementation purposes due to its ease of use and the fact that it is virtually maintenance free.

The fluidic diverter was put to use in another way in which it continually injected mass into the inlet but did so in a side-to-side manner, injecting first into one vortex and then into the other. This showed significant improvements and should be investigated further to understand its implications.

Future work should also focus on improving the duty cycle of the fluidic diverter and increasing the actuation frequencies. The fluidic diverter could be improved upon by shortening the air passageways by boring internal channels. This would serve to increase

the frequency. Reducing the volume of the chambers in the fluidic diverter should also serve to increase the frequency. Additionally, increasing the volume of the divergent output channels may help to reduce the leakage flow. This is because the larger volume path would mean that the static pressure at the point of divergence would be lower and thus there would be less force influencing the flow down the wrong path. Additionally, drawing a greater vacuum on the exhaust channel of the diverter should also help to reduce leakage.

Appendix A: Filter Codes

Filt_gen

```
function[fir,firgf,Ryx]=filt_gen(filename,sample_rate,sensors,output_channel,N,low_limi
t_set,high_limit_set,ord,lng)

%DATA FROM HOT-FILMS AND UNSTEADY PROBES
Filt_File=['data_matrix6.mat'];
load(Filt_File)
ad_channels=B;
clear B;
name = {'hf26', 'hf29', 'hf17', 'hf24', 'hf23', 'hf22', 'hf21', 'hf20', 'hf11', 'hf18', 'hf10', 'hf7',
'hf27', 'hf6', 'hf3', 'hf1', 'hf4', 'hf2', 'AIP37', 'AIP1', 'AIP7'};

%NUMBER OF INPUT SENSORS
no_sens = length(sensors);
%NUMBER OF OUTPUT SENSORS
no_outs = length(output_channel);

k=N+1;
dummy = zeros(k,k);
Acorr = zeros(no_sens*k,no_sens*k);
dummy2 = zeros(k,1);
Ccorr = zeros(no_sens*k,1);

%BAND PASS FILTER CONSTRUCTION
low_limit=low_limit_set/(.5*sample_rate); %nyquist frequency
high_limit=high_limit_set/(.5*sample_rate);
filter_vector=fir2(251,[0 .9*low_limit low_limit  high_limit 1.1*high_limit 1.0],[0 .001 1
1 .001 0]);

for sens=1:no_sens
   xf(:,sens)=ad_channels(:,(sensors(sens)));
end

%BAND PASS FILTER OF TOTAL PRESSURE DATA
yf=filtfilt(filter_vector,1,ad_channels(:,output_channel));

%BUILDING AUTOCORRELATION MATRIX
for row=1:no_sens
   for col=1:no_sens
      disp(['Computing correlation of hot films ',num2str(sensors(row)),'-
',num2str(sensors(col)),'...'])
      [CORR,LAGS] = xcorr(xf(:,col),xf(:,row),N,'unbiased');
      for i=1:k
```

```
        dummy(:,i)=CORR(k-i+1:k+N-i+1);
      end
      Acorr((row*k)-N:row*k,(col*k)-N:col*k)=dummy;
    end
end

%BUILDING CROSSCORRELATION ARRAY
for row=1:no_sens
   disp(['Computing crosscorrelation of hot film ',num2str(sensors(row)),' to AIP
',num2str(output_channel),'...'])
   [CORR,LAGS] = xcorr(yf,xf(:,row),N,'unbiased');
   dummy2(:,1)=CORR(k:2*N+1);
   Ccorr((row*k)-N:row*k,1)=dummy2;
end


%SOLVING FOR FILTER WEIGHTING CONSTANTS
Bf(:,1)=(inv(Acorr))*(Ccorr);


%BUILDING FILTER
fir=zeros(102400,1);
for i=1:no_sens
  fir=fir+filter(Bf((i-1)*N+i:i*N+i),1,xf(:,i));
end

%SGOLAY SMOOTHING OF FILTER WEIGHTING CONSTANTS
Bs=sgolayfilt(Bf,ord,lng);

%BUILDING FILTER WITH SGOLAY SMOOTHED WEIGHTING CONSTANTS
firg=zeros(102400,1);
for i=1:no_sens
   firg=firg+filter(Bs((i-1)*N+i:i*N+i),1,xf2(:,i));
end

%SECOND SET OF DATA AGAINST WHICH TO TEST FILTER
load(filename);
ad_channels2=B;
for sens=1:no_sens
   xf2(:,sens)=ad_channels2(:,(sensors(sens)));
end
yf2=filtfilt(filter_vector,1,ad_channels2(:,output_channel));

%BAND PASS FILTER OF SECOND SET OF DATA
low_limit_set2=[600];
high_limit_set2=[900];
```

```
low_limit2=low_limit_set2/(.5*sample_rate);
high_limit2=high_limit_set2/(.5*sample_rate);
filter_vector2=fir2(251,[0 .9*low_limit2 low_limit2  high_limit2 1.1*high_limit2 1.0],[0
.001 1 1 .001 0]);
firgf=filtfilt(filter_vector2,1,firg);

%CROSS CORRELATION OF FILTER AND OUTPUT FOR VERIFICATION
Ryx=xcorr(yf2,firgf,400,'coef');
```

Filt_cmd

```
sample_rate=20000;
delt=1/sample_rate*1000;
N=30;  %number of lags

sensors = [7 1 5 11 3 14 18 10 17 6 9 2 15 12 8 16 4 13]; %hot film sensors
output_channels=[19 20 21];  %AIP total pressure probes

%FILTER MADE AND TESTED FOR ONE PARTICILAR INPUT-OUTPUT
[fir,firg,Ryx]=filt_gen2('data_matrix10',sample_rate,[18],21,N,600,900,2,7);
figure
plot([-400:400]*delt,Ryx);
max=max(Ryx)

%EVERY SENSOR INDIVIDUALLY
N=1000
for pt=1:length(output_channels)
   for sens=1:length(sensors)

[fir,firg,Ryx]=filt_gen('data_matrix6',sample_rate,[sensors(sens)],output_channels(pt),N,
100,1000,2,7);
       a(sens,pt)=max(Ryx);
    end
 end


%EVERY COMBINATION OF THE HOT FILM SENSORS FOR EACH PT PROBE
usemat=zeros(2^6-1,6);
for i=1:2^length(sensors)-1
   a=dec2bin(i);
   use=[]; for j=1:length(a) if (a(j)=='1'),  use=[use length(a)+1-j]; end, end
   use=sensors(use);
   for pt=1:length(output_channels)
```

```
[fir,firg,Ryx]=filt_gen2('data_matrix10',sample_rate,use,output_channels(pt),N,600,900,2
,7);
        Maximums(i,pt)=max(Ryx);
    end
    usemat(i,1:length(use))=use;
end

%ALL COMBINATIONS OF TWO SENSORS
N=500
for pt=1:length(output_channels)
    for sens1=1:length(sensors)
        for sens2=sens1+1:length(sensors)
            [fir,firg,Ryx]=filt_gen('data_matrix6',sample_rate,[sensors(sens1)
sensors(sens2)],output_channels(pt),N,100,1000,2,7);
            b(sens1,sens2,pt)=max(Ryx);
        end
    end
end

%ALL COMBINATIONS OF THREE SENSORS
for pt=1:length(output_channels)
    for sens1=1:length(sensors)
        for sens2=sens+1:length(sensors)
            for sens3=sens2+1:length(sensors)
                [fir,firg,Ryx]=filt_gen('data_matrix6',sample_rate,[sensors(sens1)
sensors(sens2) sensors(sens3)],output_channels(pt),N,100,1000,2,7);
                c(sens1,sens2,pt)=max(Ryx);
            end
        end
    end
end
```

Appendix B: Procedures and Calibrations

Starting DeLaval Compressor

Revised:07/3/2002

Check Off *Date*

Section 1:

_ Call Wright Brothers Wind Tunnel (Richard Perdichizzi / 3-4924) to coordinate run times.

_ Call Power Plant 3-4753 (or try 3-0963). Tell them you are going to run the 2300 Volt MG Set in Bld. 31. (Tell them also you are going to run the 6" Steam Ejector if needed.)

_ Start Oil Free Compressor if needed.

Ground Floor:

_ Check in and around the MG Set and DeLaval Compressor to ensure they are clear of all junk (especially the shafts).

_ Check oil level in MG oil tank. Sight gage should read ½ to ¾.

_ Check oil level in DeLaval Compressor oil tank. Gauge should align with mark.

_ Unlock 25 KV Excitation MG set and MG oil pump electrical boxes

_ Check that the breaker is on for the 2 KVA control voltage, on column near men's room.

Motor Generator:

_ Turn Oil Filter Scraper lever, located on top of the filter, seven full Rotations (clockwise).

_ Turn on MG Oil Pump power switch on electrical box.

_ Press start button below electrical box, and next to the oil filter listen for the oil pressure switch to click.

_ Check press 10-15 PSI at gage.

_ Check sight gauges for oil flow. Must see good flow before start of MG (Takes 15-20 minutes for good flow).

0011 Basement:

At the DeLaval auxiliary oil pump.

_ Open H_2O Inlet Ball valve on oil pump heat exchanger.

Check second valve is open outside of room.

_ Check H_2O Drain Ball valve on oil pump heat exchanger is open.

_ Switch on pump: Red switch on wall

_ Turn on Air Cooler Heat Exchanger inlet water valve.

_ Check that Air Cooler Heat Exchanger outlet valve is open.

_ Set DeLaval tunnel butterflies valves as required for the particular experimental program involved. To open or closed positions as necessary.
Inlet Experiment: 3 Closed, 1 Open
Supersonic Tunnel: 2 Closed, 2 Open

Ground Floor:

_ At DeLaval gage panel check oil pressure (9-10 PSI).

_ Check all sight gauges for oil flow on the DeLaval Compressor.

Section 2:

Motor Generator:

_ Turn on valve for H_2O cooling for M.G. and DeLaval. Gate valve is on piping near the ceiling, ball valve is on the backflow preventor to the right of the electrical boxes.

_ Feel outlet pipes on both heat exchangers for water flow. Should be cold to the touch.

_ Check water pressure at switch on ceiling should be 10 psi.

_ Turn the 25 KV Excitation MG Set coupling over by hand, check that it is free of all obstacles and rotates freely. It is in front of the large MG Set.

_ Turn on exciter gen power switch on electrical box.

_ Press start button and check that the 25 KV Excitation MG set comes up to speed.

At 25 KV Excitation MG Control panel:

_ Set selector switch to #2 position. (2^{nd} floor Console).

_ Adjust 25 KV Excitation rheostats to 250 Volts (Red Mark).

_ Turn the 25 KV excitation breaker. Bottom lever to close. (Red Flag indicates the breaker is closed).

_ In 2^{nd} cabinet in the back open door and switch the electrical box lever to on.

_ Check for white light at the 2300-volt switchgear panel.

_ On Sloan Auto Lab Wall to the left of the door switch both

voltage supply boxes to 2300v.

2300 Switch gear panel:

_ At 2300 switch gear panel. Check all phases of the 2300 volts AC via. The switch is on the upper right of the panel.

_ Call Power Plant 3-4753 (or 3-0963) Tell them that building 31 will be switching the 2300-volt service to start the MG set.

_ Lock all doors.

_ Check MG set sight gauges for oil flow. If good flow is seen, continue with procedure to start MG, if not wait for good flow indication.

_ Tip Hg switch inside switchgear panel (1st door on left bottom left of panel). With non-conducting rod flip switch to left should lock and stay in left position.

_ Turn the motor field rheostat to back to start position.

_ Press start button to start MG Set. (Lots of noise). MG Set starts on the Starting Breaker, and then, don't be surprised by the Running Breaker slamming closed, Listen for it to switch over from the Starting Breaker if not check the Hg switch and try again.

_ Adjust Amps to 19.3A using the motor field rheostat. White light goes out.

_ Check all voltage and current phases.

_ Adjust 25 KV Excitation rheostats to 250 Volts (Red Mark)

Time: :

_ Allow MG to warm up 5-10 minutes before starting Compressor.

_ Observe operation of the unit including oil flow thru sight gages.

Section 3:

1st Floor:

In the 3-stage compressor area.

_ Check black DeLaval tunnel valve (blue handle) to the GE rig is closed or open as may be the case for the test run.
Inlet Experiment: Open
Supersonic Tunnel: Closed

_ Check black DeLaval discharge tunnel valve is open or closed as may be the case for the test run.

Inlet Experiment: Open
Supersonic Tunnel: Closed

1st Floor control console:

_ Set control to station #1
_ Turn LC switch, on top left of panel, to on position.
_ Switch on 115 VAC supply (on right of panel).
_ Turn the generator vernier field rheostat all the way in a clockwise direction to its min position.
_ Set generator field rheostat to the minimum field position
This is done by turning the knob clockwise (or lower) direction. When minimum field position is reach the Min. (green light) will turn on.
_ Set the compressor motor field rheostat to the max field position.
This is done by turning the switch counter-clockwise (or raise) direction until the blue equipment ready light comes on.
_ Need equipment ready light to run. If no light get help.
_ Turn Generator breaker to close. Should have red flag and lights should change from green to red.
_ Turn motor breaker to close. Should have red flag and lights should change from green to red.
_ The DeLaval compressor should now rotate and the Rpm's should read up to a minimum of 400-600.
The motor voltage should be about 80-100 volts
The motor voltage should be about 150-200 amps

Time: :

_ Allow Compressor unit to warm up at min speed for five minutes.

_ Fill out DeLaval Run Sheet during test.

To run DeLaval:

_ The compressor speed may be increased by turning the Generator main field rheostat control switch in a counter -clockwise direction, or toward its max position which raises the voltage.
Do this a little at time, keeping and eye on the compressor amperage (max 200 amps). It is slow to respond so give it a little time to react.
Fine adjustment of speed is done by turning the generator venier field rheostat counter-clock wise, remember to turn it back when you go to the next speed setting or you will

run out of its adjustment.
You can increase speed higher when you max out generator main field voltage to 250 volts by turning the compressor motor field rheostat clockwise or toward its min position. There is no fine adjustment so be careful.

Section 4:

Shut Down:

_ Turn motor breaker to trip position. Should have green flags
and lights should change from red to green.

_ Turn generator breaker to closed position. Should have green flag
and lights should change from red to green.

_ Turn LC Switch on top left of panel, to off position.

_ Switch off 115V AC supply (on right of panel).

_ Shut down MG Set at white light panel.

_ Trip 25 kV Exciter breaker. Flag should go red to green.

_ Turn breaker inside 2nd cabinet to off position.

_ Press stop button and check that the 25 KV Excitation MG set shuts down.

_ Turn off exciter generator power switch on electrical box and lock.

_ Turn water ball valve to off position.

_ Let oil systems cool approximately 1.5 Hours after cool down:

_ Shut down Oil Lube Pump to MG Set, (and lock electrical box). Shut down Oil Lube Pump to DeLaval boost pump, and shut the Inlet and Outlet water valves to the heat exchanger.

_ Turn off the Air Cooler Heat Exchanger inlet water valve.

Injection Mass Flow Calculation

A flowmeter, pressure regulator and thermocouple were used to calculate the injection mass flow. The flowmeter was from Fischer and Porter Co. It consists of an FP-1-27-6-10/55 tube and a 1-GNSVGT 69-T60 float and has a maximum flow rate of 31.4 standard cubic feet per minute (SCFM). The SCFM is defined at a reference pressure of 14.7 psia and temperature of 70° f. The SCFM is converted to cubic feet per minute (CFM) by adjusting for the current ambient temperature and pressure.

$$CFM = (\%Flow)(31.4SCFM)\sqrt{\frac{P_{op} * 530^{\circ}R}{14.7psia * T_{op}}} \tag{B-1}$$

Where P_{op} and T_{op} are the supply pressure and temperature. The density through the flow meter can be calculated as,

$$\rho = \frac{P_{op}}{RT_{op}} \tag{B-2}$$

The mass flow can then be calculated as,

$$\dot{m} = \rho \cdot CFM = (\%Flow)(31.4SCFM)\sqrt{\frac{530^{\circ}R}{14.7psia * R}\left(\frac{P_{op}}{T_{op}}\right)^{1.5}} \tag{B-3}$$

P_{op} can be written as the sum of the ambient conditions and supply gauge pressure.

$$P_{op} = P_a + P_g \approx 14.7psia + P_g \tag{B-4}$$

Finally, the injection mass flow (in lb/s) can be written as,

$$\dot{m} = 0.0847(\%Flow)\left(\frac{14.7 + P_g}{T_a + 460}\right)^{1.5} \tag{B-5}$$

Where T_a is the ambient temperature in °f.

Appendix C: Injector Blocks

Injector Block One

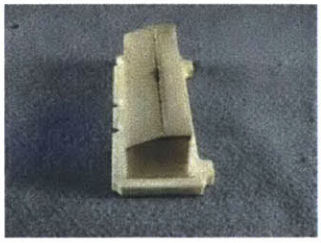


Injector Blocks Two and Three

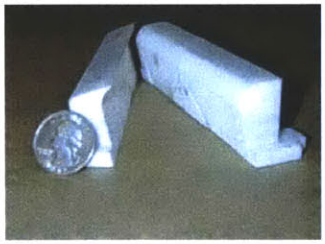


Injector Block Four

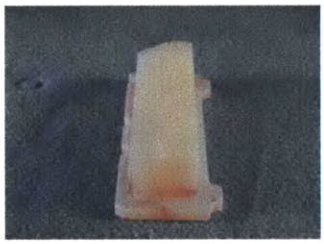
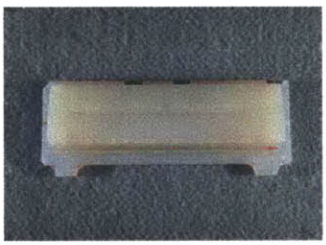

Injector Block Five

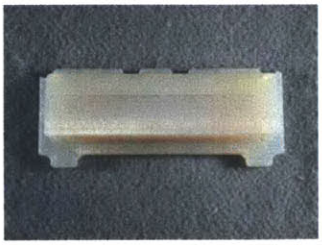


Injector Block Six

Injector Block Seven

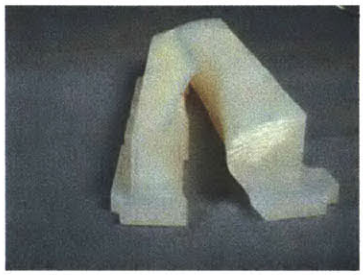

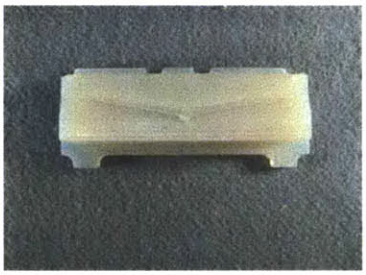

Injector Block Eight

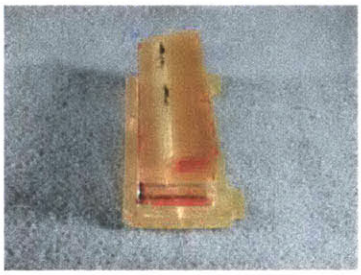

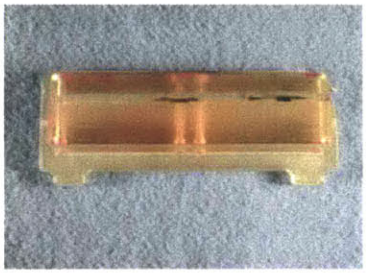

Appendix D: Pressure Recovery vs Injection Mass Flow Plots and Contours

Injector One

Slot Width: 0.032 inches
Slot Position: At Separation
Angle: 0 Degrees
Frequency: 2 kHz

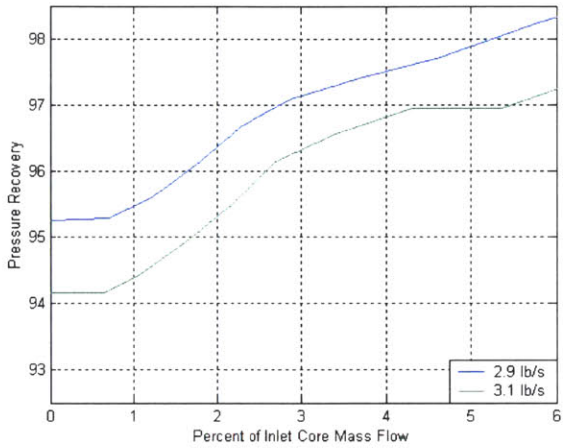

Injector Two

Slot Width: 0.02 inches
Slot Position: At Separation
Angle: 0 Degrees
Frequency: 2 kHz

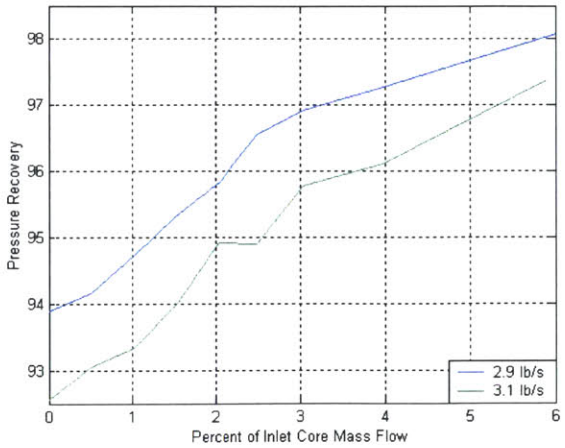

Injector Three

Slot Width: 0.01 inches
Slot Position: At Separation
Angle: 0 Degrees
Frequency: 2 kHz

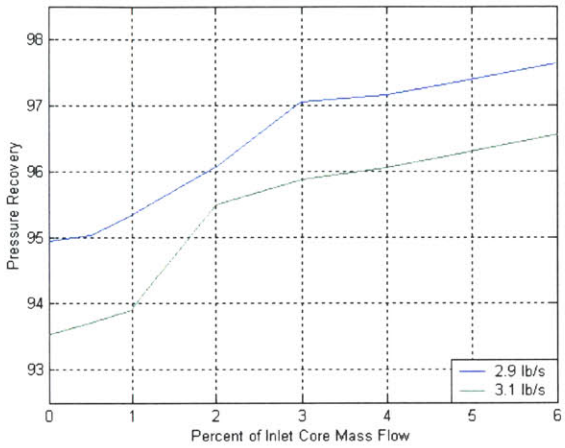

Injector Four

Slot Width: 0.01 inches
Slot Position: 0.19δ Upstream of Separation
Angle: 0 Degrees
Frequency: 2 kHz

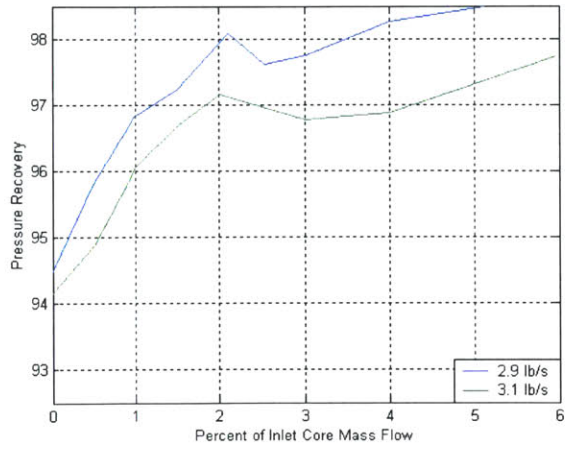

Injector Five

Slot Width: 0.01 inches
Slot Position: 0.58δ Upstream of Separation
Angle: 0 Degrees
Frequency: 2 kHz

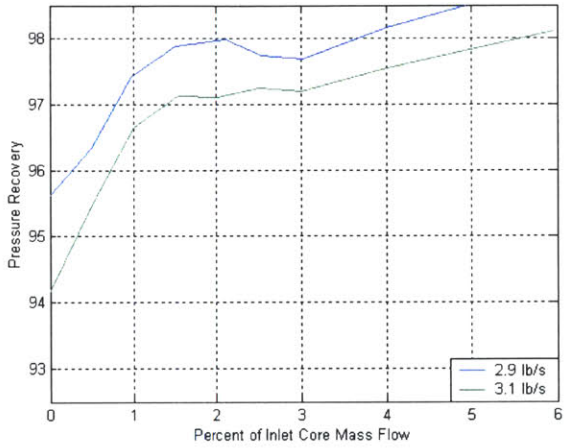

Injector Six

Slot Width: 0.01 inches
Slot Position: 0.19δ Upstream of Separation
Angle: 6 Degrees
Frequency: 2 kHz

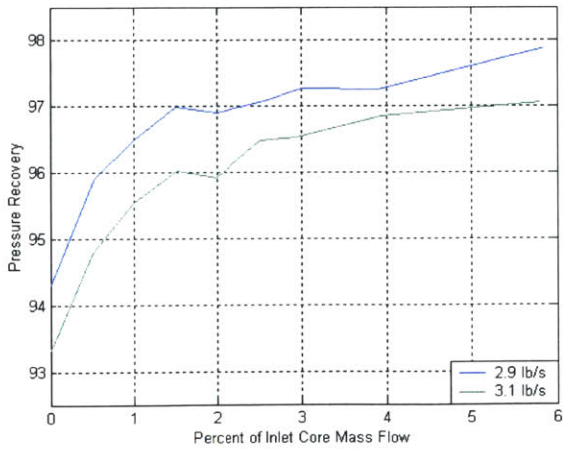

Injector Seven

Slot Width: 0.01 inches
Slot Position: 0.19δ Upstream of Separation
Angle: 12 Degrees
Frequency: 2 kHz

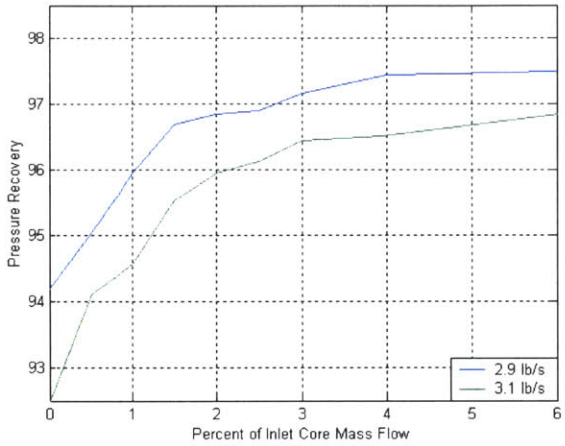

Injector Eight

Slot Width: 0.015 inches
Slot Position: 0.39δ Upstream of Separation
Angle: 0 Degrees
Frequency: 2 kHz

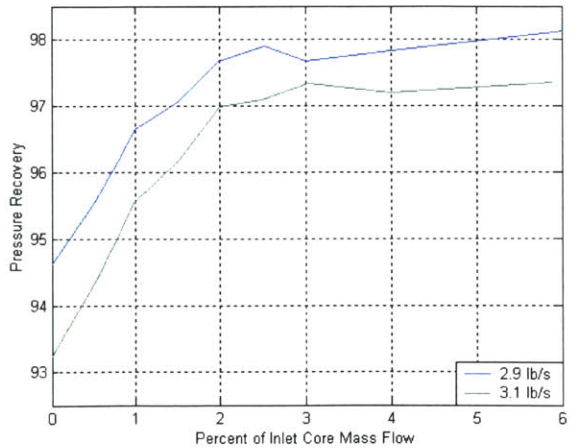

AIP Total Pressure Profiles With Increasing Injection Mass Flow

Inlet Mass Flow = 3.1 lb/s

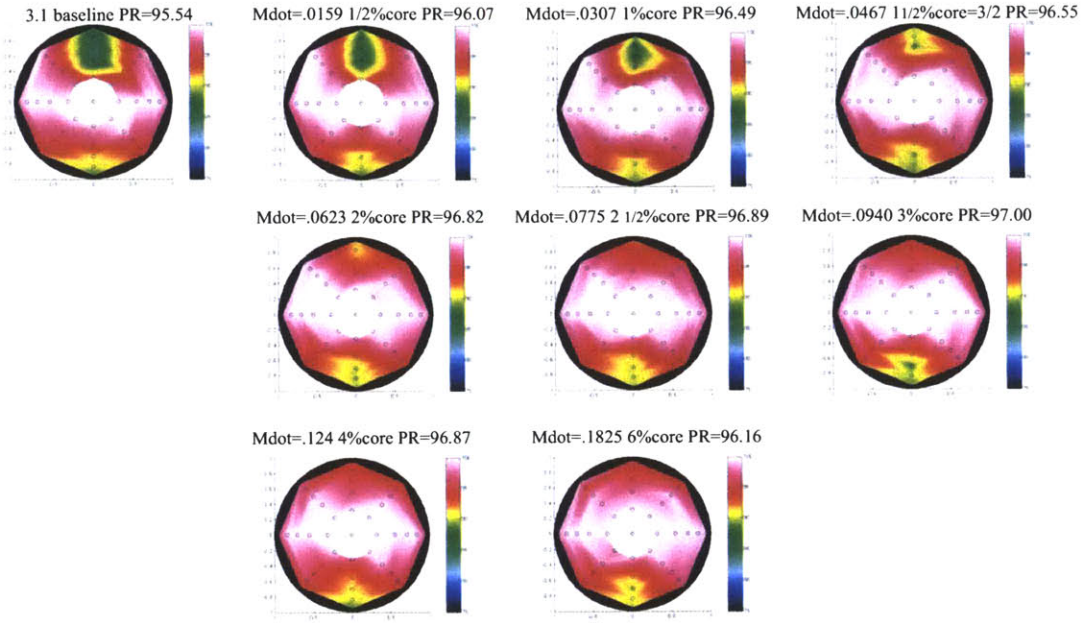

Inlet Mass Flow = 2.9 lb/s

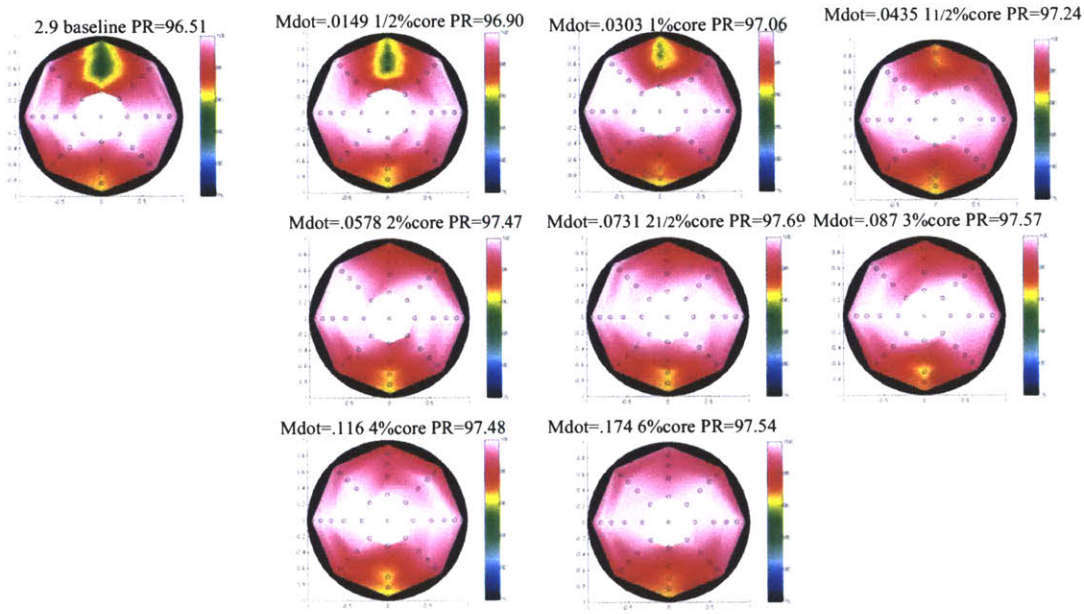

Corrected Mass Flow

As can be seen from the above Pressure Recovery vs. Injection Mass Flow figures, the starting pressure recovery varies from run to run. This can be mostly accounted for by adjusting for the atmospheric pressure and temperature associated with each run. The corrected mass flow plot shows how these values converge fairly well when ambient conditions are taken into account. A small part of the difference is also likely due to calibration drift [18].

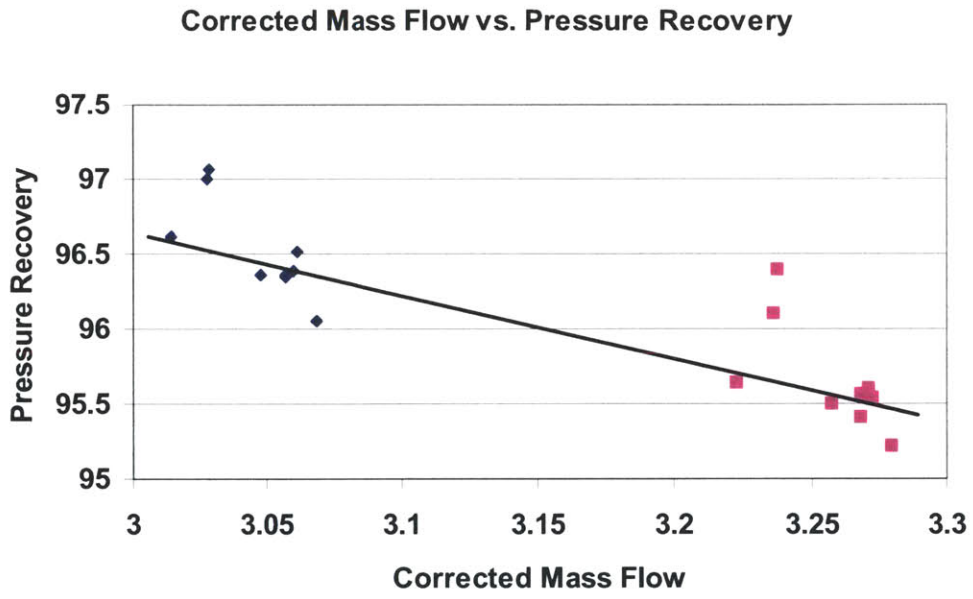

References

[1] Greenblatt, David, Wygnanski, Isreal J. "The control of flow separation by periodic excitation." *Progress in Aerospace Sciences*, vol. 36, pp. 487-545, 2000.

[2] Amitay, M., Pitt, D., Kibens, V., Perekh, D., Glezer, A. "Control of Internal Flow Separation using Synthetic Jet Actuators." AIAA 2000-0903.

[3] McCormick, D. C. "Boundary Layer Separation Control with Directed Synthetic Jets." AIAA 2000-0519.

[4] Seifert, A., Pack, L. G. "Separation Control at Flight Reynolds Numbers: Lessons Learned and Future Directions." AIAA 2000-2542.

[5] Hamstra, J.W., Miller, D.N., Truax, P.P.,Anderson, B.E., Wendt, B.J. "Active Inlet Flow Control Technology Demonstration." The Aeronautical Journal, Vol. 104, No. 1040, October 2000.

[6] Rabe, Angie, Olcmen, Semih, Anderson, Jason, Budisso, Ricardo, Ng, Wing. "A facility for Active Flow Control Research in Serpentine Inlets." 40th AIAA. Aerospace Sciences Meeting and Exhibit, AIAA-2002-0510, Reno, NV, 2002.

[7] Paduano, J., 2001-2003. Personal Communications

[8] Kwong, A.H.M., Dowling, A.P. "Active Boundary-Layer Control in Diffusers." AIAA Journal, Vol. 32, No. 12, Dec. 1994.

[9] Paduano, J.D. *Active Control of Rotating Stall Axial Compressors.* Ph.D. Thesis, Massachusetts Institute of Technology, 1991.

[10] Spakovsky, Z.S. *Active Control of Rotating Stall in a Transonic Compressor Stage with Inlet Distortion.* S.M. Thesis, Massachusetts Institute of Technology, 1999.

[11] Weigl, H.J. *Active Stabilization of Rotating Stall and Surge in a Transonic Single Stage Axial Compressor.* Ph.D. Thesis, Massachusetts Institute of Technology, 1997.

[12] Ng, Wing F., Burdisso, Ricardo A. "Active Acoustic and Flow Control for Aeropropulsion." AIAA 2001-0220.

[13] A.N. Menendez and B.R. Ramaprian. "The Use of Flush-Mounted Hot-Film Gauges to Measure Skin Friction in Unsteady Boundary Layers," Journal of Fluid Mechanics, Volume 161, 139-159, 1985.

[14] S. Kuppa and S.M. Mangalam. "In Flight Detection of Flow Separation, Stagnation and Transition." ICAS-92-3.7.2.

[13] Israel, Daniel M., Fasse, Ernest D., Fasel, Hermann F. "Numerical Investigation of Closed Loop Active Flow Control of Separation." AIAA 2002-3282.

[14] Rathnasingham, Ruben. *System Identification and Active Control of a Turbulent Boundary Layer*. Ph.D. Thesis, Massachusetts Institute of Technology, 1997.

[15] Rathnasingham, Ruben, Breuer, Kenneth S. "System Identification and Control of a Turbulent Boundary Layer." Phys. Fluids **9** (7), 1867 (1997).

[16] Amonlirdviman, Keith, Breuer, Kenneth. "Linear Predictive Filtering in a Numerically Simulated Turbulent Flow." Phys. Fluids **12** (12), 3221-3229, (2000).

[17] Rathnasingham, Ruben, Breuer, Kenneth S. "Closed-Loop Control of Turbulent Boundary Layers."....

[18] Warfield, Zachary. *Active Control of Separation Induced Distortion in a Scaled Tactical Aircraft Inlet*. S.M. Thesis, Massachusetts Institute of Technology, 2001.

[19] Brear, Michael J., Warfield, Zachary, Mangus, John F., Braddom, Cpt. Steve, Paduano, James D., Philhower, Jeffry S. "Flow Separation within the Engine Inlet of an Uninhabited Combat Air Vehicle (UCAV)." 4th ASME_JSME Joint Fluids Engineering Conference, Honolulu, Hawaii, 2003.

[20] Braddom, Steven R. *Design and Characterization of Robust Hot Film Sensors for Tactical Aircraft Inlets*. S.M. Thesis, Massachusetts Institute of Technology, 2002.

[21] McElwain, Brian D. *Unsteady Separation Point Injection for Pressure Recovery Improvement in High Subsonic Diffusers*. S.M. Thesis, Massachusetts Institute of Technology, 2002.

[22] Suzuki, T. and Colonius, T. "Large-scale unsteadiness in a two-dimensional diffuser: Numerical study toward active separation control." 41st AIAA Aerospace Sciences Meeting and Exhibit, AIAA-2003-1138, Reno, NV, 2003.

[23] MacMartin, D., Verma, A., Murray, R., Paduano, J. "Active Control of Integrated Inlet/Compression Systems: Initial Results." ASME Fluids Engineering Division Summer Meeting, FEDSM2001-18275, New Orleans, LA, 2001.

[24] DOD Dictionary of Military Terms, Joint Publication 1-02, Joint Doctrine Division, J-7, Joint Staff.

[25] Boyle, E., 2003. Personal Communications

[26] Miller, D., 2003. Personal Communications

[27] Office of the Secretary of Defense. "Unmanned Aerial Vehicles Roadmap 2002-2027." March 11, 2003.

[28] U.S. Air Force Fact Sheet. "RQ-1 Predator Unmanned Aerial Vehicle." http://www.af.mil/news/factsheets/RQ_1_Predator_Unmanned_Aerial.html

[29] "RQ-1 Predator MAE UAV MQ-9A Predator B." Global Security.org http://www.globalsecurity.org/intell/systems/predator.htm

[30] Wegerbauer, Cyndi. "Predator B UAV Contract Signed." Aeronautical Systems. December 20, 2002.

[31] "FY 2003 Request for Selected Weapon Systems. " Table 6, Center for Strategic and Budgetary Assesment. February, 2002. http://www.csbaonline.org/

[32] Kilian, Michael. "Unmanned Planes Show Mixed Results." Chicago Tribune Online Edition. March 2, 2003.

[33] Hicks, Anthony J., Avalon 2003 Air show

[34] Photo courtesy of the US Air Force Museum

[35] Major Carlson, Barak J. USAF, "Past UAV Program Failures and Implications for Current UAV Programs," ...

[36] Leonard, Robert S., Drezner, Jeffrey A., "Innovative Development: Global Hawk and DarkStar – HAE UAV ACTD Program Description and Comparative Analysis," MR-1474-AF, RAND Corp, Santa Monica, 2002.

[37] "U.S. Air Force Fact Sheet, Global Hawk." Aeronautical Systems Center, http://www.af.mil/news/factsheets/global .html

[38] "Northrop Grumman Delivers Seventh Global Hawk Vehicle to U.S. Air Force." Northrop Grumman, Feb. 25, 2003.

[39] UAV Forum. http://www.UAVforum.com/vehicles/developmental/darkstar.htm

[40] Pae, Peter. "Military Is Sold on Unmanned Spy Plane." Los Angeles Times, January 8, 2001.

[41] Richter, Paul. "Global Hawk Crashes in Afghanistan in a Setback for High-Tech Drones." Los Angeles Times, January 1, 2002.

[42] Tirpak, John A. Senior Editor: UCAVs Move Toward Feasibility. *Journal of the Air Force Association,* Vol. 82, No. 3, March 1999.

[43] Lt Col Clark, Richard M. USAF: *Uninhabited Combat Aerial Vehicles-Airpower by the People, for the people, But Not with the People*, Air University Press, Maxwell Air Force Base, Alabama, August 2000, p. 8.

[44] Chapman II, Col. Robert E. "Unmanned Combat Aerial Vehicles: Dawn of a New Age?" Aerospace Power Journal, Summer 2002.

[45] "Look, no pilot." The Economist, Science and Technology, November 11th, 2000.

[46] "United States Quadrennial Defense Review Report." United States Department of Defense, September 30, 2001.

[47] "The National Security Strategy of the United States of America." The White House.

[48] Mahnken, Thomas G. "Transforming the U.S. Armed Forces: Rhetoric or Reality?" NWC Review, Summer 2001.

[49] Haire, John, "Unmanned Combat Air Vehicle Completes First Flight," Air Force Flight Test Center, Air Force New Archive, May 23, 2002. http://www.af.mil/news/May2002/n20020523_0841.shtml

[50] "Unmanned Combat Air Vehicle (UCAV) Summary Fact Sheet." Boeing, http://www.boeing.com/news/releases/2002/q2/nr_020523m_facts.html

[51] Tirpak, John A., "Heavyweight Contender," Air Force Magazine, Vol. 85, No. 07, July 2002.

[52] "DARPA kicks of joint UCAV demonstration program." Defense Advanced Research Projects Agency, News Release, April 28, 2003.

[53] "Northrop Grumman Given Approbal to Design, Build X-47B Navy UCAV Demonstrators." Northrop Grumman, May 1, 2003.

[54] "Boeing to Develop New X-45C UCAV for Air Force and Navy Demonstrations." Boeing, April 29, 2003.

[55] Barry, Charles L., Zimet, Elihu, "UCAVs – Technological, Policy, and Operational Cahllenges," Defense Horizons, Center for Technology and National Security Policy, National Defense University, October, 2001.

[56] Guenette Jr., G., 2001-2003. Personal Communications

[57] Philhower, J., 2003. Personal Communications

[58] Kometer, M., 2002-2003. Personal Communications

[59] Dawgwillo, R., 2002-2003. Personal Communications

[60] Labs, Eric, 2002-2003. Personal communications.

[61] Seddon, J., Goldsmith, E.L. Intake Aerodynamics. 2nd ed. AIAA education series, AIAA, 1999

[62] Brown, Hwang. Introduction to Random Signals and Applied Kalman Filtering. John Wiley & Sons, New York, 1997.

[63] Proakis, Manolakis. Digital Signal Processing, Priceples, Algorithms, and Applications. Prentice-Hall, New Jersey, 1996.

[64] SAE Committee S-16, "ARP-1420 – Gas turbine engine inlet flow distortion guidelines."

[65] Mangus, John F., 2003. Personal Communications

[66] Brogan, Tory. "Air Flow Control by Fluidic Diverter for Low Nox Jet Engine Combustion." AIAA 2002-2945.